UNIVERSITY OF OKLAHOMA

GRADUATE COLLEGE

SEISMIC DATA CONDITIONING FOR QUANTITATIVE INTERPRETATION OF UNCONVENTIONAL RESERVOIRS

A DISSERTATION

SUBMITTED TO THE GRADUATE FACULTY

in partial fulfillment of the requirements for the

Degree of

DOCTOR OF PHILOSOPHY

By

SUMIT VERMA
Norman, Oklahoma
2015

SEISMIC DATA CONDITIONING FOR QUANTITATIVE INTERPRETATION OF UNCONVENTIONAL RESERVOIRS

A DISSERTATION APPROVED FOR THE
CONOCOPHILLIPS SCHOOL OF GEOLOGY AND GEOPHYSICS

BY

_____
Dr. Kurt J. Marfurt, Chair

_____
Dr. Deepak Devegowda

_____
Dr. Matthew J. Pranter

_____
Dr. Xiaowei Chen

_____
Dr. Steve Roche

To my family and friends like family

ACKNOWLEDGEMENTS

In the last four years of my PhD, I have received an endless amount of support from people, which made my PhD journey cheerful.

I received an enormous amount of guidance, knowledge, encouragement and care from my supervisor, Dr. Kurt Marfurt. In the beginning of my PhD, I was not sure what I wanted to do. Dr. Marfurt (Kurt Ji) has been patient with me and provided me with scope to think and figure out what I wished to do. I wanted to learn something new during my PhD. Coming into the program I had almost no knowledge of seismic data processing. Dr. Marfurt wanted me to be exposed to processing as if it were a viral flu. I was meant to be developing an immunity to said flu. I am glad that I learned processing, which I now understand as well as like. He also provided me with an opportunity to be *Lab guru* for his classes, which not only helped me in my PhD, but also inspired me to choose academia as my career. I feel proud to be a student of Dr. Marfurt. To me he is one of the most wonderful people I have ever met in my life.

I would also like to express my sincere thanks to Dr. Matthew J. Pranter. He provided me geological inputs for my Mississippi lime project. He also encouraged me to present at the Mississippi lime consortium, which provided me a platform to share my research with the industry experts.

I would like to thank Dr. Deepak Devegowda, who is one of my committee members, for being very easy going and friendly as well as for his help with geo-statistics in Barnett Shale TOC and Brittleness estimation project. I also want to express my gratitude to Dr. Vikram Jayram who motivated and excited me to work on the Support Vector Machine.

I would like to thank Dr. Steve Roche for being one of my PhD committee members. He provided me with feedback on my ground roll suppression work as well as help with data for my project. I would also like to thank Dr. Jamie Rich for all his help.

I would like to thank Dr. Xiaowei Chen for agreeing to become my committee member. Without his help, my PhD would have been significantly more challenging.

I would also like to express my sincere thanks to Late Dr. J. Tim Kwiatkowski. He was a source of inspiration to me. He also helped whenever there were any technical issues in the lab, preventing many setbacks along the way. I think I speak for all the students who ever worked in the 10th floor lab when I say that we did not notice how invaluable he was until after he was gone.

I would also like to thank Dr. Roger Slatt for his important comments and feedbacks on my research. I learned a lot of reservoir characterization from his courses.

I would like to thank the entire staff of ConocoPhillips School of Geology and Geophysics. I cannot forget the care of Nancy Leonard and Adrianne Fox, as they looked the finances and reimbursements and made my life simple. I also want to thank Donna Mullins who looked after issues concerning both the graduate college and courses. She has vast amounts of knowledge of the inner workings of the graduate college. She saved me from time to time by providing me correct information about graduate college rules. I would like to thank Teresa Hackney, who made me feel at home whenever I visited the geology office. I would like to thank Rebecca Fay for taking care of all the dissertation defense and graduate college issues. I would also like to thank Jocelyn Cook and Devon Harr. I would like to thank Brandy Gunter, my graduate college advisor, who has made it simpler for me to transfers credit hours and apply for removing and adding courses.

I would like to thank Dr. Brad Wallet for his help in various ways. I would like to say thanks to Sean O'Bleness and Grant Butler for helping me with any IT related problems.

I would like to thank my friends and co-authors on my different papers Shiguang Guo, Marcus Cahoj, Tao Zhao, Yoryenys DelMoro, Fangyu Li, Onur Mutlu, Thang Ha, Roderick Perez, and Manuel Aguilar. I would like to also thank Alfredo Fernandez, Ben Dowdell, and Mark Aisenberg for their help with my dissertation. I would like to mention the names of my other friends who helped me during my journey of four years: Bo, Tengfei, Jie, Gabriel, Bryce, Jyot, Sayantan, Mohsen, Oswaldo, Luis, Richard, Dania, Tobi, Joe, Trey Stearns, Dustin, Mike, Caleb, Araceli, Alyssa, Yuji, Xuan, Murphy, Aliya and Bunmi.

I would like to give special *dhannobad* to Atish Roy for all his help and support. I would like to show my gratitude to Supratik Da and Nabanita Di, who acted as my local guardians in the USA. I would like to also thank my friends Avinash, Bijit, Sara, Dhanya (*Madam*), Mahesh and Siddhesh for their support. I would like to also thank India Student Association for their support.

I also want to thank the AASPI Consortium sponsors, and my fellow graduate students at the ConocoPhillips School of Geology and Geophysics for their help and support.

Last but not the least, I would like to thank my family and my friends in India for supporting me to continue with my PhD, especially my mother who has made great sacrifices for my studies.

TABLE OF CONTENTS

Chapter 1 : Introduction 1

Chapter 2 : Interpretation Pitfalls 5

Pitfalls in Prestack Inversion of merged seismic surveys 5

Abstract 5

Introduction 6

Data Description 8

Pitfalls Analysis 10

Input data 10

Assumptions for Prestack Inversion 10

Modeled to measured data misfit 12

Offsets, fold, and prestack migration 13

Validation of our hypothesis 15

The Solution – inversion using shorter offsets 16

Conclusions 17

Acknowledgements 19

Figures 20

References 29

Chapter 3 : Seismic modeling 31

Calibration of attribute anomalies through prestack seismic modeling 31

Abstract 31

Introduction 32

Methods 35
CASE STUDIES 36
Case study 1: Seismic Modeling of Chicontepec Basin's Tectonic Structure 36
Seismic modeling of a pop-up structure 37
Seismic modeling of a graben structure 38
Discussion of results for case study 1 39
Case study 2: Seismic modeling of impedance anomalies associated with faults in the Woodford Shale 40
The Fault Model : 41
The Fracture Model : 41
Discussion on results for case study 2 42
Case studty 3 : Modeling Sags - are they Karst Collapse or Gas Chimneys Pushdown? 42
Karst Collapse Model: 43
Gas Chimney model: 43
Discussion on results for case study 3 44
Case 4 : Identifying processing challenges with seismic modeling 45
Conclusions 47
Acknowledgements 49
Figures and Tables 50
References 70
Chapter 4 : Pitfalls in seismic processing 74
Pitfalls in seismic processing: part 1 groundroll sourced acquisition footprint 74

Summary 74
Introduction 75
Motivation 76
Methodology 77
Seismic modeling 77
Seismic processing 77
Attribute interpretation 78
Results 78
Conclusions 79
Acknowledgments 80
Figures 81
References 87
Chapter 5 : Seismic Data Conditioning 88
Highly aliased groundroll suppression using a 3D multiwindow KL filter: Application to a legacy Mississippi Lime survey 88
Abstract 88
Introduction 89
Exploration Objectives and Data Description 92
Method 94
Validation with a Synthetic patch 96
Application 96
Conclusions 97
Acknowledgements 98

Figures and Tables 99
References 120
Chapter 6 : Estimation of TOC and Brittleness 123
Abstract 124
Introduction 125
Geology of the study area 127
Methodology 128
Correlating Core to Wireline Measurements 129
TOC estimation using Passey's equation 129
Multilinear regression 130
Brittleness estimation using Wang and Gale equation 132
Correlation to wireline logs 132
Volumetric estimation of TOC and brittleness 133
Volumetric TOC estimation 134
Volumetric Brittleness estimation 135
Correlation of TOC and BI to Relative EUR: AASPI proto type Cigar Probe 135
Limitations of TOC and BI correlation with Production using cigar probe 137
Results 137
Disscussion and Conclusions 139
Figures and Tables 140
References 163
Chapter 7 : Conclusions 166

LIST OF TABLES

Table 3.1 Survey geometry created for models. 51

Table 5.1. Computation cost for the processes. 109

Table 6.1 TOC estimated with window of ±1ft has least validation error and highest correlation with 4 well logs. 147

Table 6.2. BI estimated with window of ±2ft has least validation error and highest correlation with 4 well logs. 151

Table 6.3. Validation and Training error using a window of ±8ms for volumetric TOC estimation. 155

Table 6.4 Validation and Training error using a window of ±12 ms for volumetric BI estimation. 157

LIST OF FIGURES

Figure 2.1. Location map of Anadarko basin area on map of Oklahoma, and location of study area in Anadarko basin marked by green boundary (modified from Northcutt and Campbell, 1988). 20

Figure 2.2. Stratigraphy of Anadarko basin in Pennsylvanian and Mississippian age, here Red Fork Formation and two of the geologic formations that appear as strong reflectors on seismic are highlighted in pink. Hunton (highlighted in blue) and Woodford (highlighted with green) are also formation of interest for current operators in the area (Modified from Clement, 1991). 21

Figure 2.3. "Fold Map" of the reprocessed megamerged 3D seismic data volume. Superficially, this gives the impression that the data are greater than 25 fold throughout the survey..... 21

Figure 2.4. Phantom horizon slices 80 ms below Oswego cutting the Red Fork incised channels through (a) the P-impedance volume, Z_P, (b) the S-impedance volume, Z_S, computed from 2°-42° input migrated gathers. For both of the figures, white arrows indicate artifacts in the resulting image. Black dotted arrow indicates a circular artifact. 22

Figure 2.5. (a) Synthetic gather generated at a well, with angles ranging between 0°-42°. (b) Synthetic gather generated at a well, with offset range 0°-22°, and padded with zero

traces from 24° -42°. (c) Extracted amplitudes corresponding to the red and cyan picks in (a) and (b). 23

Figure 2.6. Representative gathers and base map indicating their locations. Note that location A and D have moderate amplitudes while B and C have low amplitudes at the farther offsets. The small residual amplitudes beyond these ranges are due to migration swings from the longer offset surveys. 24

Figure 2.7. Mean-squared error map showing the difference between the measured and modeled seismic gathers for the 2°–42° inversion. 25

Figure 2.8. Horizon slices along the Oswego surface through offset-limited stacked amplitude volumes: (a) 0-1520 m (~0-5000 ft) (b) 1520-2450 m (~5000-8000 ft) (c) 2450-3350 m (~8000-11,000 ft) (d) 3350-4250 m (~11000-14000 ft) and (e) 4250-5200 m (~14000-17100 ft). The Oswego Lime was interpreted as a strong peak in the stacked seismic volume. Amplitude changes in c may be valid AVO effects. Often, inaccurate velocities (including anisotropic effects) result in misaligned gathers giving rise to zero crossings and troughs at far offsets. However, note how the amplitude approaches zero in the top right corner of the megamerged survey in (d) and (e) indicating that these large offsets were never recorded in these areas. White polygons in (c) indicate amplitude anomalies that will be used in subsequent quality control. White arrows indicate the major highways. 26

Figure 2.9. Phantom horizon slices 80 ms below the Oswego through (a) the P-impedance volume, Z_P, (b) the S-impedance volume, Z_S, computed from 2°-22° input migrated gathers. Pink polygons correspond to an area of high error shown in Figure 2.10. 27

Figure 2.10. Mean squared error map showing the difference between the measured and modeled seismic gathers for the 2°-22° inversion. To compare with Figure 6 the squared error was normalized with respect to the number of traces in each gather. White arrow corresponds to those drawn about amplitude anomalies shown in Figure 8c. Pink polygons encircle an area of high error that is posted on Figure 2.9..... 28

Figure 3.1 Flowchart for generation of synthetics..... 50

Figure 3.2 Horizon slice along the top Jurassic through co-rendered coherence, most-positive curvature, and most-negative curvature. The same three attributes are co-rendered with amplitude on the vertical slice, which shows a pop-up feature (yellow arrow) and a graben (cyan arrow). Although the edges of these features are well delineated by curvature, the coherence anomaly (in green) appears to be broken. In subsequent images, we will generate 2D models over these features to better understand the lack of a coherence anomaly. (Data courtesy of PEMEX)..... 51

Figure 3.3 Vertical slices through the seismic amplitude volume through (a) a pop-up block and, (b) a graben previously shown in Figure 3.2. Fault traces are shown in by red lines. (c) and (d) The same images are co-rendered with most-positive and most-negative curvature. Figures displayed at 1:1 scale..... 52

Figure 3.4 (a) A representative well in the study area showing gamma ray, density, and P-wave sonic logs. (b) The model of the pop-up feature seen in Figure 3.3a. (c) Graben model based on image shown in Figure 3.3b. The units below the top Paleocene are faulted. P-wave velocity V_P is in ft/s while density ρ is in g/cm3. (d) Snapshot at 0.7sec, green star represents source location and the red inverted tringles represent receiver position, blue arrow represents primaries and yellow arrow represents multiples..... 54

Figure 3.5 (a) Modeled prestack depth migrated (time converted) data from 120 common shot gathers based on model displayed in Figure 3.3a. The same section co-rendered with (b) dip, (c) 2D curvature, and (d) coherence. Primaries are indicated by cyan arrow and multiples are indicated yellow arrow. Note that the multiples from the shallower horizon disrupt the anomalies on dip and curvature. The fault plane reflection appears only above the stronger reflection. These fault plane reflections give rise to a continuous response such that the coherence anomalies are minimal. All the attributes including seismic are displayed with 50% opacity..... 55

Figure 3.6 (a) Modeled prestack depth migrated (time converted) data from 120 common shot gathers on model displayed in Figure 3.3b (primaries are indicated by cyan arrow and multiples are indicated yellow arrow). The same section co-rendered with (b) dip, (c) 2D curvature, and (d) coherence. Note that the multiples from the shallower horizon disrupt the anomalies on dip and curvature. The fault plane reflection appears only about the stronger reflection. These fault plane reflections give rise to a continuous response such that the coherence anomalies are minimal. All the attributes including seismic are displayed with 50% opacity..... 56

Figure 3.7 Horizon slices along the top Woodford Shale through (a) most negative principal structural curvature, (b) acoustic impedance, and (c) most-negative curvature (a 2nd derivative) of the acoustic impedance volumes. Note the correlation of structural curvature lineaments with subtle faults on the vertical slice through seismic amplitudes. These faults give rise to subtle changes in amplitude and hence to impedance, which are delineated through 2nd derivative (curvature) computations seen in (c). The correlation of the low impedance anomalies and structural lows implies that they are either fault- or

fracture-related, though this correlation may be due to limitations in seismic imaging rather than to geology. (Data courtesy of CGG-Veritas. After Guo et al., 2010). 57
Figure 3.8 (a) A representative well log section of the study area, and (b) model of a suite of faults with variable throw constructed to evaluate the hypothesis that amplitude anomalies are due to errors in prestack migration. The green Woodford Shale layer is faulted with the fault dying out in the deeper blue Hunton Limestone layer. (c) Model to evaluate fractures filled with low impedance material. In this model we represent a variable number of 20 ft wide fracture zones with lower impedance inclusions. Velocities are in ft/s, while densities are in g/cm^3. 59
Figure 3.9 (a) Prestack time migrated stacked seismic section generated from 100 common shot gathers over the model shown in Figure 3.8b. Note the amplitudes across these faults are a very continuous, indicating that prestack time migration preserves amplitude across faults with such small throw. The top Woodford at t~0.35 s is clearly visible. The faults with throws of 10 and 20 ft fall below seismic resolution, while faults with throw greater than 40 ft are more easily identified. Stacked seismic amplitude co-rendered with (b) coherence shows the faults with 40 ft and higher throws, (c) Curvature was able to see the all the faults. (d) Acoustic impedance also maps the fault and does not suffer from imaging loss amplitudes. 60
Figure 3.10 (a) Prestack time migrated stacked seismic section generated from 100 common shot gathers over the model shown in Figure 3.8c. The top Woodford at t~0.35 s is clearly visible. As in the real data, the velocity model for prestack migration did not include the perturbation due to the fractures. While the top of the fracture zones are accurately imaged (yellow arrow) the base is overmigrated because the velocity used was

too fast (orange arrow). In addition, the base of the limestone layer experiences a velocity pushdown effect (cyan arrow). Stacked seismic amplitude co-rendered with (b) coherence shows the faults with 4 and 8 fracture zones clearly, (c) Curvature was able to delineate fractures. (d) In contrast to the fault model, the fracture zones give rise to a low impedance anomaly, as seen in the real data shown in Figure 3.7b and c. 61

Figure 3.11 (a) A cross section through the envelope of the seismic data (time domain) corresponding to lines AA' from a survey acquired over Liuhua field reservoir, offshore China. The dotted white line indicates the top Miocene carbonate reservoir. (b) Horizon slice along the top reservoir through the coherence volume. Yellow arrows indicate karst collapse chimneys. Note the incoherent image above the karsted reservoir in (a) indicated by the white arrow. Such poor imaging indicates the data were migrated using an incorrect velocity model, consistent with the collapse chimney hypothesis. High amplitude reflections (black arrow) that ring the chimney are consistent with gas charge from below. (After Story et al., 2000)..... 62

Figure 3.12 Seismic cross section showing four karst depressions. Note the two karsts on the left have smaller diameters and steeply dipping reflection (blue arrows) while the two on the right have larger diameters and less steeply reflectors (red arrows). Model parameters defined from well W. (Data courtesy Devon Energy). 63

Figure 3.13 (a) An illustration of the karst model used. (b) A low velocity gas chimney model used. Both models are based on Figure 3.12. In both the models V_P is in ft/s while density ρ is in g/cm^3..... 64

Figure 3.14 Seismic cross section through the depth migrated (converted to time) (a) karst collapse model of Figure 3.13a and (b) the gas chimney model of Figure 3.13b. 65

Figure 3.15 (a) Time-structure map of top basement horizon. The northern part of the horizon is noisy and difficult to pick. Since the top basement and the top evaporite are close to each other, the rugose appearance of the northern top basement is not geophysical noise, but rather geology, represent the weathered, eroded, and fractured top basement. Geologic relief of the top basement is as high as 360 ft. (b) Co-rendered image of k_1, k_2, and coherence along the top basement horizon. We suspect that some of the NW-SE lineaments may be acquisition footprint. The k_1 lineament is displaced ~200 ft to the south of the k_2 lineament. 66

Figure 3.16 Flat-layered Earth model with hypothesized fractures in the basement (a) with, and (b) without a weathering zone. Velocity and density generally increased with depth, except for the low-density evaporate. The fractures are 20-ft thick and have lower velocity and density than the basement. This model in (b) is designed to avoid the reverberation effect of seismic wave in the weathering zone..... 67

Figure 3.17 (a) Acoustic-modeled gather on model shown in Figure 3.16b with interpreted events. Head wave, reflections, diffractions, and reverberation are identified on the gather by alternatively examining the snapshots of the wave field. (b) Elastic-modeled gather on model shown in Figure 3.16a with interpreted events. Head wave, reflections, ground roll, and reverberation are identified. Note that diffractions are not identified because it was overlaid by strong reverberation from the weathering zone. (c) Real shot gather with interpreted events. Head wave, reflections, ground roll, and reverberation are identified. Note that the reverberation effect of the weathering zone is much less in the real gather than the modeled gather due to finite Q (1/attenuation). At the target depth (t=0.57s), critical refraction occurs at offset h = 3200 ft. Beyond this

point, the signal are highly contaminated by coherent, moderate bandwidth refracted waves and must be muted after NMO correction. 68

Figure 3.18 Acoustic-modeled shot gather sorted by absolute offset corresponding to the model with no weathering zone Figure 3.16b and (a) with and (b) without fractures. (c) Difference between (a) and (b), showing diffractions. Note that diffractions are not centered at zero offset. 69

Figure 4.1 (a) Timeslice at t=0.41s through most negative curvature volume from real seismic dataset. The North-South lineaments are aligned with the receiver lines. These artifacts contaminate attribute volumes. (b)Timeslice at t=0.41s through coherence volume from real seismic dataset. The North-South lineaments are aligned with the receiver lines. These artifacts are weaker at depth but overprint the objective at t=1.0s. 81

Figure 4.2 The synthetic model's geometry. Sources are in red and receivers are in green. The geometry is perfectly rectilinear which is not the case with actual seismic data due to surface obstructions. 82

Figure 4.3 Shot vs absolute offset sorted (a) modeled seismic data with four reflectors and groundroll with a large bandwidth (0-50Hz). b) F-K modeled groundroll to be removed from the modeled seismic data (a). (c) Result of subtracting F-K modeled groundroll (b) from modeled seismic (a). Notice large amounts and high amplitude groundroll is removed, but residual remains. 83

Figure 4.4 (a) Inline through the synthetic seismic data. (green horizon is displayed in Figure 6a) (b) Inline of real seismic data (yellow horizon is displayed in Figure 4.6b) . Notice the undulation anomalies caused by inadequately removed groundroll in Figure

4.6a and similar undulation features can be seen in Figure 4.6b most likely caused by groundroll. 84

Figure 4.5 (a) Time slice at t=1.320s through most negative curvature of the synthetic seismic data. Notice the undulation anomalies caused by inadequately removed groundroll. (b) Coherence at t=1.320s of the synthetic seismic data. Similar undulation features can be seen causing lateral discontinuity in the reflectors. 85

Figure 4.6 Horizons tracked through (a) synthetic data, displayed on Figure 4.4a as green horizon. (b) real seismic data, displayed on Figure 4.4a as yellow horizon. The linear striations (red arrows) are due to residual groundroll overprinting P-wave reflections. 86

Figure 5.1 (a) Fold Map of the four merged surveys. Before reprocessing (b) vertical section of seismic amplitude (c) time slice at t =1.1 sec at the level of Mississippian chert for coherence. Note the strong EW and NS footprint in both images (indicated by yellow arrow). 100

Figure 5.2. After 5D interpolation before eliminating coherent noise (a) vertical section of seismic amplitude (b) time slice at t =1.1 sec at the level of Mississippian chert for coherence. Notice footprint seen in Figure 5.1c appears to be interpolated. 101

Figure 5.3. (a) A representative shot gather (sorted by shot vs channel) before ground roll suppression. Figure 4 shows the geometry of receiver lines R1-R6 for this shot. (b) Bandpass filtered 40 Hz <f < 50 Hz image shows ground roll having high frequency components masking the target zone (indicated by the green rectangle). 102

Figure 5.4. A representative receiver patch. The common shot gather associated with source location indicated by blue dot is shown in Figure 5.3. These 18 sources into 360

channels forms an 18x360 trace 3D seismic volume. If we flatten the noise in this volume using linear moveout, we can use multiwindow structure oriented filters to model it. 104
Figure 5.5. The groundroll suppression workflow presented in this paper. 105
Figure 5.6. (a) Common shot gather sorted by absolute offset x after a high cut filter removing reflections with f >50 Hz, strong ground roll window indicated by top and base mutes parallel to the group velocity of approximately 1000 m/s. (b) Windowed data shown sorted by common shot vs channel number. (c) The same gather after linear moveout using a phase velocity of v=1524m/s (5000 ft/s). Note the ground roll events are relatively flat while the underlying signal is steeply dipping. 107
Figure 5.7. (a) Local residual linear moveout (dip) in Inline direction, where increasing channel numbers are “in-line” and increasing shot numbers are “cross-line” in reference to the 18x360 trace patch geometry. Crossline dips are computed but not shown. (b) Coherence computed on the windowed, flattened patch, high coherence indicates coherent ground roll. (c) Modeled ground roll using a Karhunen-Loeve filter within those windows exhibiting a coherence, $c > 0.3$. 108
Figure 5.8. A simplified cartoon showing a suite of nine overlapping 3 shot by 3 receiver Kuwahara (1976) windows used to filter the ground roll. The red star and triangle indicate the target trace to be filtered such as the blue shot point into a channel on receiver line R5 in Figure 4. First we compute the coherence along local 3D dip for each of the nine windows. The window with the highest coherence value best represents the coherent ground roll. Within this window, we then apply a 9-trace Karhunen Loeve filter along dip to model the desired ground roll for the red source-receiver pair. In actual implementation, we also allow our windows to vary vertically over ±10 samples, such

that we search 21x9 =189 windows, all of which include the target time sample at the target shot-receiver trace. 110

Figure 5.9 (a) Modeled ground roll, after reverse linear move on the gather shown in Figure 5.7c. Notice that the modeled ground roll has dominant frequency range of 25-40 Hz. (b) The same shot gather (sorted by shot vs channel) after ground roll suppression, obtained by subtracting modeled ground roll (Figure 5.9a) from the original gather (Figure 5.3a). (c) Amplitude spectrum of seismic shot gather before (in blue) and after (in red) ground roll suppression. 113

Figure 5.10. Synthetic prestack gather data generated with 18 sources and 360 channels, the acquisition patch is shown in the upper right corner of the figures. Shot vs channel gather for blue source (a) before ground roll suppression (b) after ground roll suppression (c) removed coherent noise. 114

Figure 5.11. After ground roll suppression (a) vertical section of seismic amplitude (b) time slice at t =1.1 sec at the level of Mississippian chert for coherence. Compare this figure with the Figure 1, to see improvements after ground roll suppression. 117

Figure 5.12. After ground roll suppression as well as prestack seismic data conditioning (a) vertical section of seismic amplitude (b) time slice at t =1.1 sec at the level of Mississippian chert for coherence. Compare this figure with the Figure 5.1, to see improvements after ground roll suppression. 118

Figure 5.13. A different seismic data set, (a) before ground roll suppression, (b) after ground roll suppression. Notice, the elimination of aliased ground roll and preservation of signal after ground roll removal. 119

Figure 6.1. Areal extent of the Mississippian Barnett Shale, Fort Worth Basin, Texas (Aydemir, 2011). The red circle indicates the approximate location of cored well A, used in this study. 140

Figure 6.2. Location of cored wells A and B with respect to the seismic survey. 141

Figure 6.3. Interpretation of baseline for Density and ILD on Well A. The ideal baseline would be a shale/silt stone with zero total organic carbon. Black solid straight line on bulk density (RHOB) curve indicates RHOB_base and red solid straight line on ILD (deep resistivity) curve indicates RTD_Base. 141

Figure 6.4. (a) Mean vitrinite reflectance (R_o) map of Barnette Shale (Pollastro, 2007). Red circle indicates the approximate location of study area. (b) Vitrinite reflectance (R_o) vs Level of Maturity (based on Crain's Petrophysical Handbook, 2015). 142

Figure 6.5. Gamma ray(GR), bulk density(RHOB), neutron porosity (NPHI), deep resistivity (RTD) and core TOC (in green) and TOC computed with Passey's (1990) method (TOC_Passey, in pink) on (a) well A (on which we define the baseline), and (b) well B. 144

Figure 6.6. Crossplot between core measured TOC and ROC computed with Passeys's method (a) well A on which I define the baseline, and (b) other cored well B. 145

Figure 6.7. Work flow for creation of BI and TOC volumes. 146

Figure 6.8. Cross section AA' showing subsurface stratigraphic correlation using gamma ray log (Singh, 2008). 146

Figure 6.9. Multilinear regression and input and output. 147

Figure 6.10. Cross plot between core measured TOC and neural network estimated TOC, (a) well A which was used to train the neural network, and (b) other cored well B. ... 148

Figure 6.11. Gamma ray (GR), bulk density(RHOB), neutron porosity(NPHI), deep resistivity(RTD), P-Sonic, TOC estimated with Passey's method (TOC_Passey), normalized stratigraphic height, core measured TOC (in green) and neural network estimated TOC (TOC_PNN, in black) at (a) training well A, and (b) validation well B. 149

Figure 6.12. Gamma ray well log and core measured mineralogy, quartz, total limestone, total clay, dolomite along with core measured TOC and brittleness index computed with Wang and Gale (2009) formula, on cored wells (a) well A, and (b) well B. 150

Figure 6.13. Cross plot of cored well A in lower Barnett Shale; (a) Core measured TOC vs Wang and Gale BI with FTIR mineralogy, (b) FTIR measured total clay % vs core measured TOC. BI and TOC has an inverse trend in deeper part of Lower Barnett Shale, as well as TOC increases with clay. 151

Figure 6.14. Gamma ray (GR), bulk density, neutron porosity (NPHI), deep resistivity (RTD), P-Sonic, neural network estimated TOC (TOC_PNN), normalized stratigraphic height, Wang and Gale computed BI (BI_W_G, in black) and neural network estimated BI (BI_PNN, in pink) at (a) training well A, and (b) validation well B..... 152

Figure 6.15 Cross plot between core computed BI and neural network estimated BI, (a) well A which was used to train the neural network, and (b) other cored well B..... 153

Figure 6.16. Map of top of Lower Barnett Shale surface. For neural network analysis, the circled wells were kept as blind wells and non-circled wells were used as the training wells..... 154

Figure 6.17. Probabalistic Neural Network work flow used to predict the TOC volume from seismic attributes. 154

Figure 6.18. Cross-plot between predicted TOC using a neural network and TOC well log with 30 wells used in neural network training. 155
Figure 6.19. Vertical slice along the line XX' through estimated TOC volume (location shown in Figure 6.16). Notice the estimated TOC volume shows a good match at the blind wells (70 % correlation). 156
Figure 6.20. Cross-plot between predicted BI using a neural network and BI well log with 30 wells used in neural network training. 157
Figure 6.21 Vertical slice along line XX' through estimated BI volume (location shown in Figure 6.16. Notice the estimated BI volume shows a fair match at the blind wells (50% correlation). 158
Figure 6.22. Map view of microseismic event locations corresponding to (a) Well C and (b) Well D the orientation of the fracture lineaments formed by the microseismic events align with the current maximum horizontal stress direction in the Fort Worth Basin (NE-SW). (c) Horizon slice along the top Viola Limestone through the most positive curvature seismic attribute volume. The majority of the microseismic event locations fall into the areas with negative curvature values (bowl shapes). Red vectors indicate velocity anisotropy where the length of the vector is proportional of the degree of anisotropy while the direction indicates the azimuth of maximum anisotropy.The seismic data were acquired after 400 wells stimulated, such that the velocity anisotropy represents the post-frack stress regime. (Modified from Perez, 2013 and Thompson, 2010). The maximum distance of a posted event from a well is 1000 ft, which will be used for as R_{max} in Figure 6-23. 159

Figure 6.23. Illustration of the cigar probe workflow, horizontal well is drilled in the Lower Barnett Shale. The flow (production) to each perforation can be approximated by the impulse response of Green's function $1/R^2$. I assume all the sections are perforated and each point on the well is producing equally. Integration of all the points to along the well bore path to get the weighted average property can be correlated to the production. 160

Figure 6.24 Crossplot between, relative EUR, and (a) TOC, and (b) BI. There is almost no-correlation between production and TOC or BI. 161

Figure 6.25. Neural network training with relative EUR as target property and TOC and BI as input. Training was done on 100 wells. (a) Cross plot between actual relative EUR and predicted EUR on training wells. (b) Plot of actual vs predicted for training wells and validations wells. Notice the training correlation is 54% and validation correlation is 38%. 162

ABSTRACT

Shale resource plays are fairly new to the petroleum industry, but they have reinvigorated oil and gas production in North America. Brittleness and TOC are the two most important parameters for shale resource characterization. Ideally, of the multilinear and non-linear regression can be used to correlate TOC and brittleness measured on core to well logs forming a proxy for TOC and brittleness with in the seismic survey. In turn seismic attributes correlated to TOC and brittleness predictions from well logs. The success of such integration depends on data quality. In Texas and the mid-continent much of our seismic data have been merged and reprocessed using modern technology. I will expose one pitfall on merged seismic surveys due to offset range variation. Other pitfalls are best addressed by seismic modeling.

Legacy seismic data acquired in the mid-continent region have low fold, resulting in a rise to low signal to noise ratio. Such data often exhibit a strong acquisition footprint, which can be caused by the presence of aliased ground roll. Conventional processing techniques cannot suppress such groundroll without damaging the signal. I developed and applied a coherence-based technique to remove highly aliased ground roll present in a survey of North Central Texas Mississippi Lime play.

The predicted TOC and brittleness volumes showed a fair correlation with production in the Barnett Shale of Fort Worth Basin. The areas of good production are associated with high brittleness in the vicinity of high TOC.

CHAPTER 1 **: INTRODUCTION**

Shale resource plays have formed attractive oil and gas resource plays for the past decade. Brittleness and TOC are two primary parameters which are required to characterize such plays. While one can use cored wells to compute brittleness and TOC from well log data, lateral heterogeneity of shales makes interpolation of such parameters solely from well control inaccurate.

Modern quantitative interpretation (QI) workflows are commonly used to integrate well logs with seismic amplitude and attribute volumes to predict volumetric estimates of porosity. Predictions of brittleness and TOC are more recent objectives brought on by the interest in shale reservoirs. QI is heavily based on prestack seismic inversion for P-impedance, S-impedance, Poisson's ratio, lambda-rho, mu-rho and (for high quality long offset data) density. Other attributes often provide softer information. Curvature measures strain which may be correlated to natural fractures, coherence often shows geohazards such as small fault and collapse features, while spectral decomposition can be correlated to depositional stacking patterns. Multilinear regression and non-linear regression, such as neural networks, can be used to provide a relationship between seismic volumes and petrophysical property logs. Such regression relations can be applied to 3D seismic attribute volumes to obtain a TOC volume.

Success of QI depends on seismic and well log data quality. QI is sensitive to ambient noise and accuracy of processing parameters. Not addressing data quality can lead to erroneous predictions.

In Chapter 2, I address some of the pitfalls associated with prestack seismic inversion. In the 1990's most seismic surveys were acquired with smaller offset ranges

than used today. Over the intervening two decades the increase in recording capacity has resulted in both longer offset and wider azimuth surveys. While ideally, one would reshoot a target with more modern technology, cost and limited access often justifies reprocessing legacy surveys. In order to improve lateral resolution by increasing migration aperture, companies often merge multiple contiguous surveys. In this chapter, I analyzed a mega merged seismic data composed of more than five different surveys acquired over 20 years with different ranges of source-receiver offset. These seismic data were processed by a commercial acquisition and processing company, where they used the survey with the higher offset range as the reference survey. Migration noise fills the far offset bins in areas where there are no data. Performing pre-stack seismic inversion without discounting this migration noise leads to erroneous estimates of impedance. In this chapter, I describe and illustrate how one can find the usable range of offset. By limiting the offsets used in our prestack inversion, I obtain less aggressive but still useful results.

In Chapter 3, I demonstrate the use of seismic modeling to determine common pitfalls in seismic analysis. Seismic modeling allows the geophysicist to evaluate alternative hypothesis and thereby define the uncertainty in seismic interpretation. In case study two of this chapter, I focus on the Woodford Shale of the Arkoma basin, where low impedance anomalies may be due to fractures associated with faulting, or due to the inability to accurately preserve amplitudes near a fault. With the help of modeling, I show that the hypothesis of increased porosity is correlated to the occurrence fractures rather than amplitude dimming due to poor fault imaging.

In Chapter 4, I investigate remnant groundroll as the source of acquisition footprint on modeled stacked seismic data. The most important component of groundroll is radially travelling dispersive Rayleigh waves. Significant groundroll remained in the gathers and stack after *f-k* filtering, giving rise to false structural artifacts. In this chapter, I show that insufficiently suppressed groundroll leads to artifacts that one can result in an erroneous interpretation.

In Chapter 5, I reprocess a legacy 3D merged survey with a Mississippi lime target. Currently seismic acquisition companies use 4000 or more channels to acquire the data with nominal fold ranging between 200 and 1000. The seismic survey discussed in Chapter 5 was acquired in 1990's with 360 channels, with the nominal fold of this merged survey being15. Such sparse sampling causes the groundroll to be spatially aliased. I design and implement a new data adaptive coherence-based workflow to suppress aliased groundroll, resulting in improved the data quality. The improvement can be seen not only on the vertical slices through the seismic amplitude data but also on 3D seismic attributes. For example, coherence computed from reprocessed data shows faults which were previously masked by acquisition footprint.

In Chapter 6, I estimate TOC and brittleness volumes using seismic, core and well data. In general, TOC can be computed on well logs using Passey's method. The major weakness associated with Passey's method is that, it requires an interpreter-driven definition of a baseline. In order to be more quantitative, I compute a multilinear regression relation between TOC measured on core samples and well logs of two cored wells. I use this multilinear regression relation to predict TOC on wells, which were not

cored providing a TOC “proxy” with in 3D seismic survey. I correlate Wang and Gale’s estimates of brittleness based on mineralogy to elastic logs on the cored well, and use same multilinear regression to compute brittleness on other wells without elastic logs. These forty wells form the well control for neural network estimation of TOC and brittleness from the 3D seismic attribute volumes.

CHAPTER 2 : INTERPRETATION PITFALLS

PITFALLS IN PRESTACK INVERSION OF MERGED SEISMIC SURVEYS

Sumit Verma[1], Yoryenys Del Moro[2], and Kurt J. Marfurt[1]

[1]The University of Oklahoma, ConocoPhillips School of Geology and Geophysics.

[2]Noble Energy, Houston, Texas, USA.

This paper was published by SEG journal Interpretation in 2013.

ABSTRACT

Modern 3D seismic surveys are often of such good quality and 3D interpretation packages so user-friendly that seismic interpretation is no longer exclusively carried out by geophysicists. This ease-of-use has also been extended to more quantitative workflows, such as 3D prestack inversion, putting it in the hands of the "non-expert" – be it geologist, engineer, or new-hire geophysicist. Indeed, given good quality input seismic data, almost any interpreter who can generate good well ties and define an accurate background model of P-impedance, S-impedance and density, can generate a quality prestack inversion.

Two of the authors are new geophysicists who fell into the prestack inversion "pit". Fortunately, they were, able to recognize that something was wrong. We applied prestack inversion to gathers that were carefully reprocessed by a major service company. The problem however was not with the processing, but with our lack of understanding of the input legacy data that formed part of a larger "megamerge" survey. Not all of the surveys that were merged had the same offset range. In the migration step, gaps in long

offsets of the older surveys were not muted. Migration noise from newer surveys was allowed to fill this space.

In this paper we share our initial workflow and suspicious results. We also clarify the meaning of "fold" and "offset" for prestack-migrated gathers. In addition to presenting some QC tools useful in analyzing megamerge surveys, we show how by limiting the offsets used in our prestack inversion, we obtain less aggressive but still useful results.

INTRODUCTION

Much of midcontinent USA and Texas is covered by legacy 3D seismic surveys. During the period of low oil prices in 1980s and 1990s, many of these properties were sold, traded, or consolidated, while licenses to the 3D surveys were in turn traded to data brokers in exchange for seismic data over areas of more active interest. Most data brokers (some of whom are major service companies as in this study) pride themselves in their ability to pull more information out of legacy data. They do this in two ways. First, they reprocess the data using modern surface-consistent statics, noise-reduction, spectral balancing, and seismic imaging techniques. Second, they merge the prestack data with adjacent surveys, thereby increasing the migration aperture, resulting in improved lateral resolution of steeply dipping faults, channel edges, and other discontinuities, particularly near the internal edges of the surveys that form the megamerge.

Such processing can be difficult. The megamerge survey discussed in this paper was acquired with dynamite in some areas, and vibroseis with different sweeps and number of vibrators in other parts of the survey. The geophones may be grouped in

different arrays and may have different spectral responses. It is common for the shot and receiver line spacing and also for the line orientations to change from survey to survey. Nevertheless, careful processing can produce significantly improved results. Using the stacked version of the data discussed here, Del Moro et al. (2013) illustrate the improvements of the megamerge versus a unmerged legacy survey in mapping incised Pennsylvanian age Red Fork channels using seismic attributes.

The advent of resource shale, tight sand, tight lime, and other resource plays has renewed interest in these legacy surveys. Most resource plays are exploited through horizontal drilling followed by either hydraulic fracturing, acidation, or both. In addition to identifying horizontal drilling hazards (geohazards), we wish to better quantify the geomechanical properties (for hydraulic fracturing) and lithology (for higher porosity sweet spots) through the use of prestack impedance inversion.

The survey of interest was shot at various times, beginning in the mid 1990s. CGG-Veritas acquired licenses for these surveys, shot infill data where necessary, and carefully reprocessed them, resulting in a megamerge survey (Figure 2.1). Many of these surveys were shot to map Pennsylvanian age Red Fork sandstones. While the Red Fork is the focus of this paper, the major focus of most of the operators is now on the deeper Mississippian age Woodford Shale, Mississippi Lime, Hunton Limestone resource plays (Figure 2.2).

We encountered a pitfall while attempting prestack impedance inversion of the megamerge survey. The data were very carefully reprocessed, with most of the events quite flat and relatively noise free on common reflection point gathers. Our objective was to use prestack inversion to identify what are known as “invisible” Red Fork sands –

sands that are not seen on conventional stacked or P-impedance seismic data volumes where polarity reversals give rise to a low amplitude stack. Such sands are commonly logged while drilling for deeper Woodford Shale objectives. Barber and Marfurt (2010) applied fluid substitution to such wells in a neighboring county and similar megamerge survey, and hypothesized that there should be a shear impedance anomaly if the data could be processed using prestack inversion.

We begin with data description and follow up with an overview of the assumptions required by prestack inversion. Next we briefly review prestack migration, explaining the meaning of offset and fold on common offset migrated results. This background allows us to discuss the pitfall that befell us. We show the suspicious results, and follow with some simple quality control plots and representative CRP gathers that illustrate what happened. With this understanding, we performed a less-aggressive (offset-limited) prestack inversion and quality control the results. We conclude with a summary of the pitfall, as well as a series of steps which should be included in a conventional workflow which will alert the interpreter to its occurrence.

Data Description

The study area is located in the eastern part of Anadarko Basin in west central Oklahoma (Figure 2.1). The target is the Red Fork sand of Middle Pennsylvanian. It lies approximately at a depth of 2680 m (~8800 ft), and is composed of clastic facies deposited in deep marine (shale/silt) to shallow water fluvial dominated system. The Red Fork sand is, sandwiched between limestone layers, with the Pink lime on top and the Inola lime on

the bottom (Figure 2.2). The Oswego lime which lies above the Pink lime and Novi lime which lies below the Inola lime, are very prominent reflectors on seismic amplitude data.

There are 21 wells with P-wave sonic and density logs distributed throughout the survey. In addition, two of these wells also have shear sonic logs. The pre-stack data from six different surveys were phase matched and pre-stack time migrated, which together resulted in common reflection point gathers (CRP), covering approximately 630 km^2 (245 mi^2). These gathers served as input to prestack inversion in order to estimate the lithology of the different architectural elements of the incised channel system.

The post stack seismic had a 65-85% correlation with the synthetics generated at the wells. The prestack data were converted from 300-5200 m (~1000-17100 ft) offset gathers to 2°-42° angle gathers using a well (sonic log) velocity model. We prepared low frequency P-impedance, S-impedance and density background models from the 21 wells and four seismic horizons. So, the background models incorporate strong impedance changes at limestone/clastic boundaries. Following a standard workflow (Hampson and Russel 2005; Russel et al. 2006), we extracted wavelets for 2°-15°, 14°-28° and 27°-42° angle-limited stacks. Then using Fatti's equation (equation 1), we simultaneously inverted three angle limited stacks to obtain P and S -impedance. We will revisit the assumptions of the inversion workflow in the next section.

We expected that fold would be a good measure of seismic data quality. Prior to prestack inversion we not only examined the fold in the headers, but also computed the fold using the inversion software. The astute reader may now see us walking towards the pit. We were reassured to find that the megamerge survey had good, consistent fold throughout, ranging between 25 and 30 (Figure 2.3).

Although the major stratigraphic features, including fluvial channels and overbank deposits were well resolved, the resulting P-impedance (Z_P), as well as S-impedance (Z_S) images were suspicious where white arrows indicate linear artifacts and black arrows indicate circular artifacts (Figure 2.4). We wanted to know the reason behind the creation of such artifacts. We therefore begin our analysis on the input data that went into the megamerge seismic data as well as a review of the assumptions made by our inversion process.

PITFALLS ANALYSIS

Input data

We did know that of the six constituent seismic surveys, the first acquisition survey was carried out by Amoco in 1993 followed by two connected surveys, also by Amoco, in 1994 and 1996 (Peyton et al., 1998), using hardware and best practices available at that time. These surveys covered the north-east part of the megamerge survey area. Other operators acquired seismic surveys imaging in the adjacent acreage from the years 1999-2005 with a relatively larger source-receiver offsets, which further analysis will indicate to be larger source receiver offsets of 4600m (15000ft). In 2006, the data from different companies were licensed to CGG-Veritas. CCG-Veritas acquired some additional data to fill in important gaps prior to merging all the component surveys into a single prestack dataset using modern (year 2008) statics solutions, noise attenuation, and seismic imaging technology.

Assumptions for Prestack Inversion

We use commercial software prestack seismic inversion based on

Fatti et al.'s (1994) approximation to the Zoeppritz equations

$$R(\theta) \approx \frac{\Delta Z_P}{2Z_P}(1 + tan^2\,\theta) \; - 8\left[\frac{Z_S}{Z_P}\right]^2 \frac{\Delta Z_S}{Z_S} sin^2\,\theta, \qquad (1)$$

where

Z_P = average or background model P-impedance,

Z_S = average or background model S-impedance,

ΔZ_P and ΔZ_S = the vertical change in P- and S-impedances, and

θ = the angle of incidence.

The modeled prestack response using equation 1 was tied to a well in the survey (Figure 2.5). The synthetic represents an NMO-corrected gather such that the reflectors are aligned. Examining the reflector marked by the red line shows amplitudes becoming more negative with increasing angle of incidence, θ. In conventional AVO analysis, we would simply measure this change and call it the amplitude "slope" or "gradient" while the value at θ=0^0 would be called the "intercept". Many modern prestack inversion software implementations use iterative modeling based on either simulated annealing or genetic algorithms using equation 1 to fit the data and thus estimate Z_P and Z_S.

The derivation of the gradient term, or alternatively estimation of Z_P and Z_S, requires the reflectors to be aligned across the incident angle. Although it is well understood that the inversion on misaligned prestack gathers produces incorrect results, users can easily encounter a pitfall if they do not carefully examine the data or have too much faith in their technology. Such residual moveout is best corrected by residual velocity analysis, although trim statics may work within a relatively small analysis window. The red curve in Figure 2.5c shows the plot of amplitude variation with angle of the synthetic modeled for 0°-45° corresponding to the picked horizon in Figure 2.5a.

In Figure 2.5b, we replace the farther 25°-45° angles in the gather with zero amplitude traces. The gradient corresponding to the amplitudes along the cyan pick in Figure 2.5b are displayed as the cyan curve in Figure 2.5c. Obviously, this latter amplitude variation with the angle will generate an inaccurate gradient and inaccurate estimate of Z_P and Z_S.

Modeled to measured data misfit

In order to better understand the problem, we examined a suite of migrated CRP gathers at different locations across the megamerge survey (Figure 2.6). We note that the reflector along the green Oswego pick has strong amplitudes aligned up to offsets of 4250 m (~14,000 ft) at location A. At location C (Figure 2.6c) the alignment is good to about 4000 m (~12,000 ft). At locations B and D (Figure 2.6b and d) this event is aligned up to only 3050 m (~10,000ft). Beyond this point, the amplitudes are close to zero.

To validate our impedance inversion, we generated the synthetic data with the inversion products. Then, we subtracted the synthetic from the original gathers and created a mean squared error volume. A horizon slice through this error volume along the top Oswego shows that the highest error areas (appearing as red) are in the northeast and east side of the megamerge survey (Figure 2.7). This includes the gathers shown in Figure 2.6b and d. This area also corresponds to the suspicious artifacts seen on the Z_P and Z_S slices shown in Figure 2.4. The best fit was in the northwest part of the survey, which includes the gather shown in Figure 2.6a. An interpreter might incorrectly use Figure 2.7 to risk-weight the impedance estimates shown in Figure 2.4.

Offsets, fold, and prestack migration

The pitfall occurs when one does not understand the mechanics of prestack common offset migration and what this does to the concepts of fold. To be specific, we will base our arguments on prestack common offset Kirchhoff migration, though the concepts are appropriate to wave equation and reverse time migration as well. Unlike 2D data, which will often have a finite discrete number of source-receiver offsets, 3D data will have an almost continuous distribution of source-receiver offsets. Early common-offset migration algorithms introduced the concept of an offset "bin". Each trace corresponding to a given source-receiver pair is accurately migrated using an offset measured to a fraction of a meter, then added to a result that has been binned to say, the nearest 100 m, thereby forming a "partial stack". A more recently-introduced variation is to define irregular width annular offset bins, each of which contains approximately the same number of traces. Yet another "offset vector-tile" implementation is closely tied to a specific acquisition design, and is designed to produce migrated gathers suitable for azimuthal anisotropy analysis. In this case, traces with source-receiver offsets and azimuths that fall within a (typically square) tile will be independently migrated and formed into a partial stack for that tile.

Our megamerge data contains data that were acquired at different times by different companies using different sources, receivers, and recording systems. Specifically, the more modern 2000-2005 constituent surveys contained larger offsets (up to approximately 5200 m) than the older 1993-1995 vintage surveys (up to approximately 2700 m). To accommodate the newer data, the megamerged survey was migrated using offset bins that ranged between 0 and ≈5000 m.

One can think of prestack Kirchhoff migration as taking every sample of the unmigrated data and projecting it onto a 3D ellipsoid. The shape of the ellipsoid is a function of the two way travels time of the sample and the migration (time or depth) velocity model. These ellipses are truncated radially by a value called the "migration aperture". If one were to take a sample at a two-way travel time of 4 s and migrate it with a velocity of 5000 m/s, it could image a reflector or diffractor 10,000 m away. Such large apertures are common for deep-water marine data to image overturned flanks of salt dome where the water velocity is accurately known and the attenuation is often moderate. For land data, extremely large migration apertures are usually avoided, not only for cost, but because of problems in accurately defining the attenuation and velocity models. This restricted approach is more common in relatively flat lying areas such as those imaged by this survey. We do not know the migration aperture used for this megamerge, but a reasonable guess would be somewhat less than 5,000 m. Using this number, we then found that the far offset data acquired in the northwest part of the survey would be migrated or "swung" 5000 m into areas covered by the short-offset vintage surveys. Interpreters commonly encounter such "migration swings" on migrated stacked data volumes at the edges of their surveys or underneath obstacles such as towns and lakes. Thus, the "data" at the farther offsets shown in Figure 2.6b-d are not from the overlying survey, but rather migrated noise from an adjacent, more modern survey. Far offsets that have little to no data in them will appear to have been "padded" with near-zero value traces. A small amount of migration swing will cause a trace to have data in it, preventing it from being flagged as "dead". Thus, the "fold" map represents the 30 offset bins of the migrated data, not the fold of the original unmigrated surveys (Figure 2.3). The lower

"fold" seen in the northeast corner of the megamerge clearly shows the circular limits corresponding to the migration aperture from the corners of neighboring longer offset constituent surveys.

Validation of our hypothesis

The original input surveys and their acquisition and processing information were not available; the only seismic data available were the gathers of the migrated megamerged survey. In order to identify the useable offset ranges for the data, we picked the peak, which corresponds to the Oswego lime horizon on the full stack volume, and generated horizon slices through a suite of offset-limited stacks. Because of the AVO effects we do not expect these slices to show a consistent polarity. Figure 2.8a-c show a nearly constant blue value corresponding to a positive peak for offset-limited stacks of 0-1520 m (~0-5000 ft), 1520-2450m (~5000-8000 ft), and 2450-3350 m (8000-11,000 ft). The change from blue (positive) to green (less positive) values in Figure 2.8c is an acceptable AVO effect. However, as we examine the horizon slice through the offset-limited stack at 3350-4250 m (~11000-14000 ft), we note lower (positive and negative) amplitudes and less continuous anomalies in the northeast part of the megamerge survey. Finally, the horizon slice through the offset-limited stack of 4250-5200 m (~14000-17100 ft) shows zero or near-zero amplitude (white area) in the northeast corner of the megamerge corresponding to the shorter offset acquisition of the 1993-1995 Amoco surveys (Peyton et al., 1998). Note the circular migration "impulse responses" seen in this part of the survey where some of the more modern, longer offset infill data has been migrated into the shorter offset data.

The Solution – inversion using shorter offsets

Given the result of this analysis, it is inappropriate to use the images shown in Figure 2.4 for the entire survey. To obtain a uniform quality inversion for the entire survey we simply limit the offsets of our inversion to the range 0-2750m (0-9000ft). At the target Red Fork horizon (below the Oswego), these offsets correspond to an angle range of 2°-22°. Such a near angle limitation precludes inversion for density (Aki and Richards, 1980); however, we can still invert for Z_P and Z_S using equation 1, though with lower confidence (Plessix and Bork, 2000) than we had originally anticipated using larger angles. We used the same low frequency background model used for Figure 2.4, but this time extracted three wavelets for inversion at 2°-9°, 9°-15°, and 14°-22°. The prestack simultaneous inversion shown in Figure 2.9 has none of the artifacts seen in Figure 2.4. The background amplitude varies relatively smoothly, showing the incised channels of variable fill more clearly. Readers interested in the geological analysis of these inversions should refer to Del Moro (2012).

Following our earlier quality control steps, we computed the squared difference between the modeled and measured data for 2°-22°, and displayed a time slice along the Oswego top through the error volume in Figure 2.10 using the same color bar and scale as in the 2°-42° inversion shown in Figure 2.7. Although we have restricted the input seismic to 2°-22° to avoid the error, we still see some areas of misfit, such as about the NNW-SSE trending highway imaged using the 1993 acquisition. Interestingly, the E-W trending highway to the south is much more heavily traveled but was acquired by a more recent survey. The pink polygon in Figure 2.9 and 10 appears to be associated with subsurface geology though not with the channels, or to the present day river flowing in

NW-SE direction. This suggests that the offset restriction of 0-4250m is good for most of the areas, but the actual offset range was even smaller than 4250m in some areas. A more careful inversion would be adaptive for different angle ranges in different parts of the megamerge survey.

CONCLUSIONS

Legacy seismic data acquired by different companies using different acquisition parameters over adjacent acreage can be merged into a larger survey that can be subsequently imaged using a larger migration aperture, thereby improving lateral resolution. "Fold" on migrated data traces should be suspect, and depends on whether the processor retained the fold of the input surveys through the complete data equalization and reprocessing flow, or carefully computed the illumination at each subsurface point using a more sophisticated imaging technique. Fold count after migration can be misleading as a proxy to measure signal strength.

If a given input survey is acquired using shorter offsets, Kirchhoff and other common-offset migration algorithms will generate numerical noise on the padded far offset empty traces. It can also generate steeply dipping signals. In general, such far offsets should not be used in prestack inversion. Because of migration "swings", these unilluminated offsets will rarely, if ever, be zero, making automatic detection of dead traces difficult. This leads the unsuspecting interpreter and inversion algorithm to believe that such traces contain measured data. Prestack inversion will attempt to find impedances and densities that will fit all the migrated data, including unilluminated offsets that are close to zero, giving erroneous results.

To avoid such pitfalls, we first suggest that interpreters generate RMS error maps of the modeled-to-measured data misfit for any inversion product. Such maps can be used in subsequent risk analysis. It is valuable to see the pre-stack gathers of different parts of the megamerge survey, but this could be really time consuming. So, for megamerge surveys where the offsets of the constituent input survey volumes are unknown, the interpreter should generate time or horizon slices through amplitude volumes for each of the offsets. Subsequent inversions should be offset- (and implicitly, angle-) limited to include only those offsets with physically reasonable amplitudes.

ACKNOWLEDGEMENTS

We thank CGG-VERITAS for providing the megamerge seismic survey and Chesapeake Energy for the well data used in this project. Special thanks to Alfredo Fernandez of OU, for his help and support. Funding for the research was provided by the industry sponsors of the Attribute-Assisted Seismic Processing and Interpretation (AASPI) consortium. Finally, we thank Schlumberger for Petrel and Hampson-Russell for Strata software licenses provided to The University of Oklahoma for research and education.

FIGURES

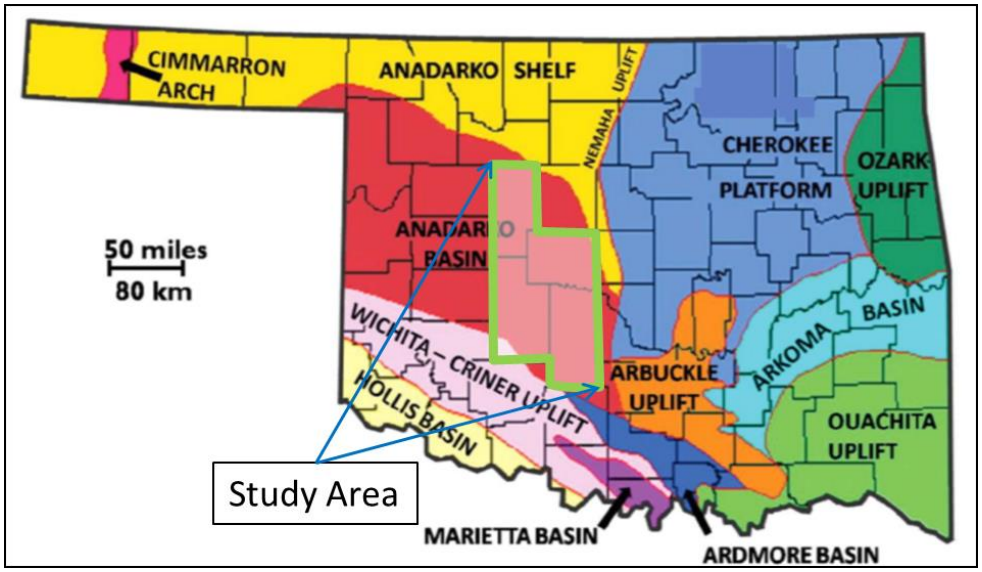

Figure 2.1. Location map of Anadarko basin area on map of Oklahoma, and location of study area in Anadarko basin marked by green boundary (modified from Northcutt and Campbell, 1988).

SYSTEM	SERIES	GROUP	FORMATION BED	ROCK TYPE	OROGENY
PENSYLVANIAN	VIRGLIAN	WABUNSEE	WABUNSEE SS.	WICHITA MOUNTAIN FRONT C AND GRANITE WASH	
		SHAWNEE	HEEBNER SH.		
			LOVELL LM.		
		DOUGLAS	TONKAWA SS.		ARBUCKLE OROGENY
	MISSOURIAN	OCHELATA	AVANT LM.		
			COTTAGE GROVL SS.		
		SKIATOOK	HOGSHOOTER LM.		
			LOWER LAYTON SS. (MARCHAND)		
			CHECKBOARD LM.		
			CLEAVELAND SS.		
	DESMONESIAN	MARMATON	BIGLIME		
			OSWEGO LM.		
			PRUE SS.		
		CHEROKEE	VERDIGRIS LM.		
			SKINNER SS.		
			PINK LM.		
			RED FORK LM.		
			INOLA LM.		
	ATOKAN		NOVI LM.		
			13 FINGER LM.		
	MORROWAN		UPPER MORROW FM.		WICHITA OROGENY
			LOWER MORROW FM.		
	SPRINGERAN		CUNNINGHAMSS.		
			BRITT SS.		
			BOATWRIGHT SS.		
MISSISSIPPIAN	CHESTERIAN		CHESTER LM.		
			GODDARD SH.		
			MANNING SS.		
	MERAMECIAN		STE. GENEVIEVE LM.	BASINAL SHALES	
			ST. LOUIS LM.		
			CANEY SH		
			SPERGEN LM.		
			WARSAW LM.		
	OSAGEAN		SYCAMORE LM. MAYES SH.		
	KINDERHOOKIAN		WOODFORD FM.		
			MISNER SS.		

Figure 2.2. Stratigraphy of Anadarko basin in Pennsylvanian and Mississippian age, here Red Fork Formation and two of the geologic formations that appear as strong reflectors on seismic are highlighted in pink. Hunton (highlighted in blue) and Woodford (highlighted with green) are also formation of interest for current operators in the area (Modified from Clement, 1991).

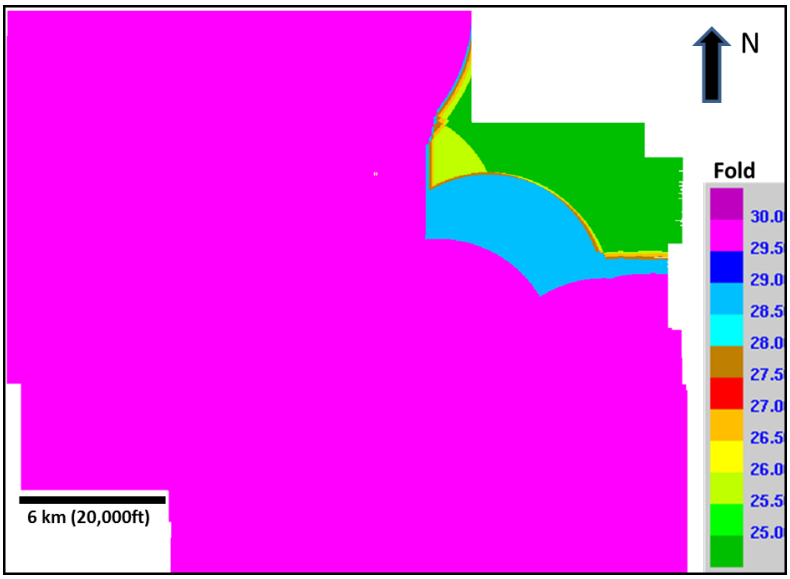

Figure 2.3. "Fold Map" of the reprocessed megamerged 3D seismic data volume. Superficially, this gives the impression that the data are greater than 25 fold throughout the survey.

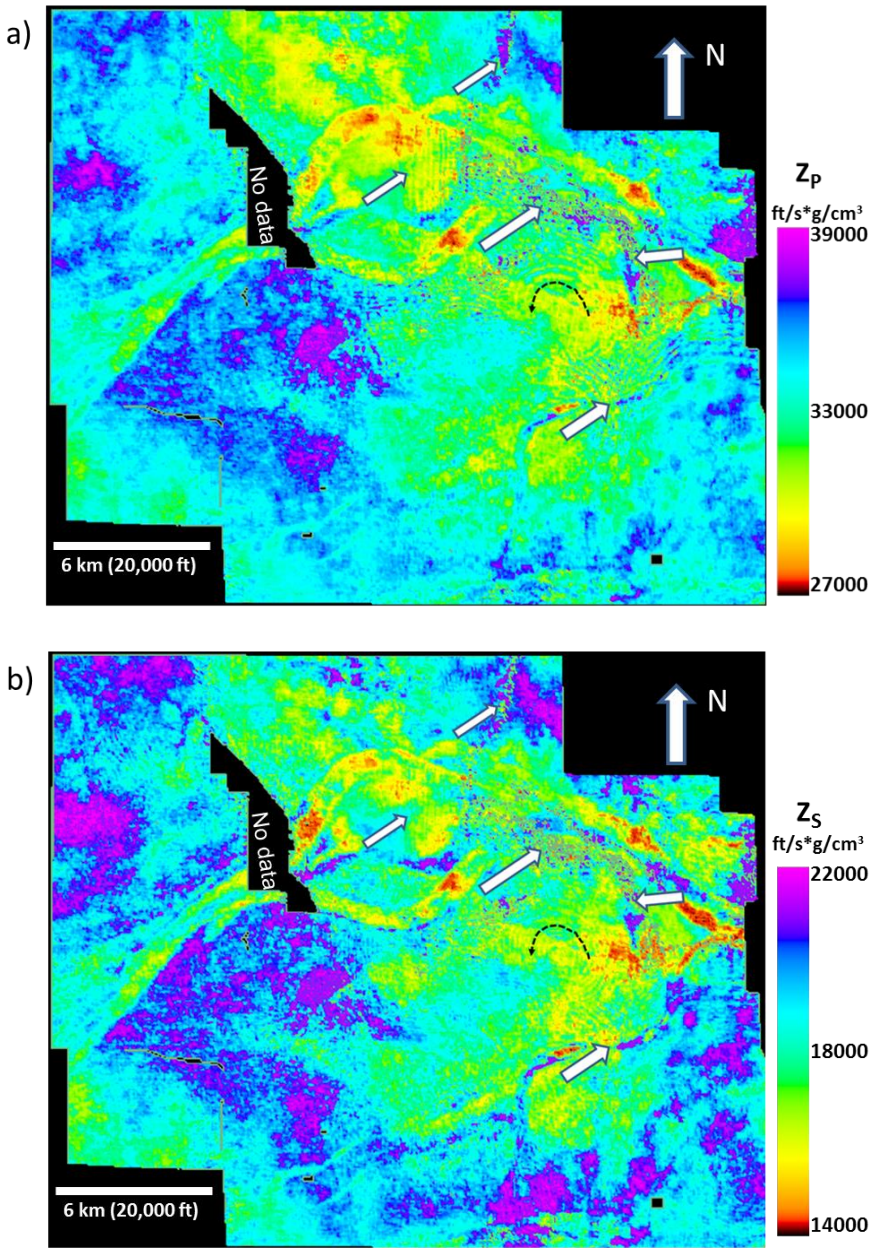

Figure 2.4. Phantom horizon slices 80 ms below Oswego cutting the Red Fork incised channels through (a) the P-impedance volume, Z_P, (b) the S-impedance volume, Z_S, computed from 2°-42° input migrated gathers. For both of the figures, white arrows indicate artifacts in the resulting image. Black dotted arrow indicates a circular artifact.

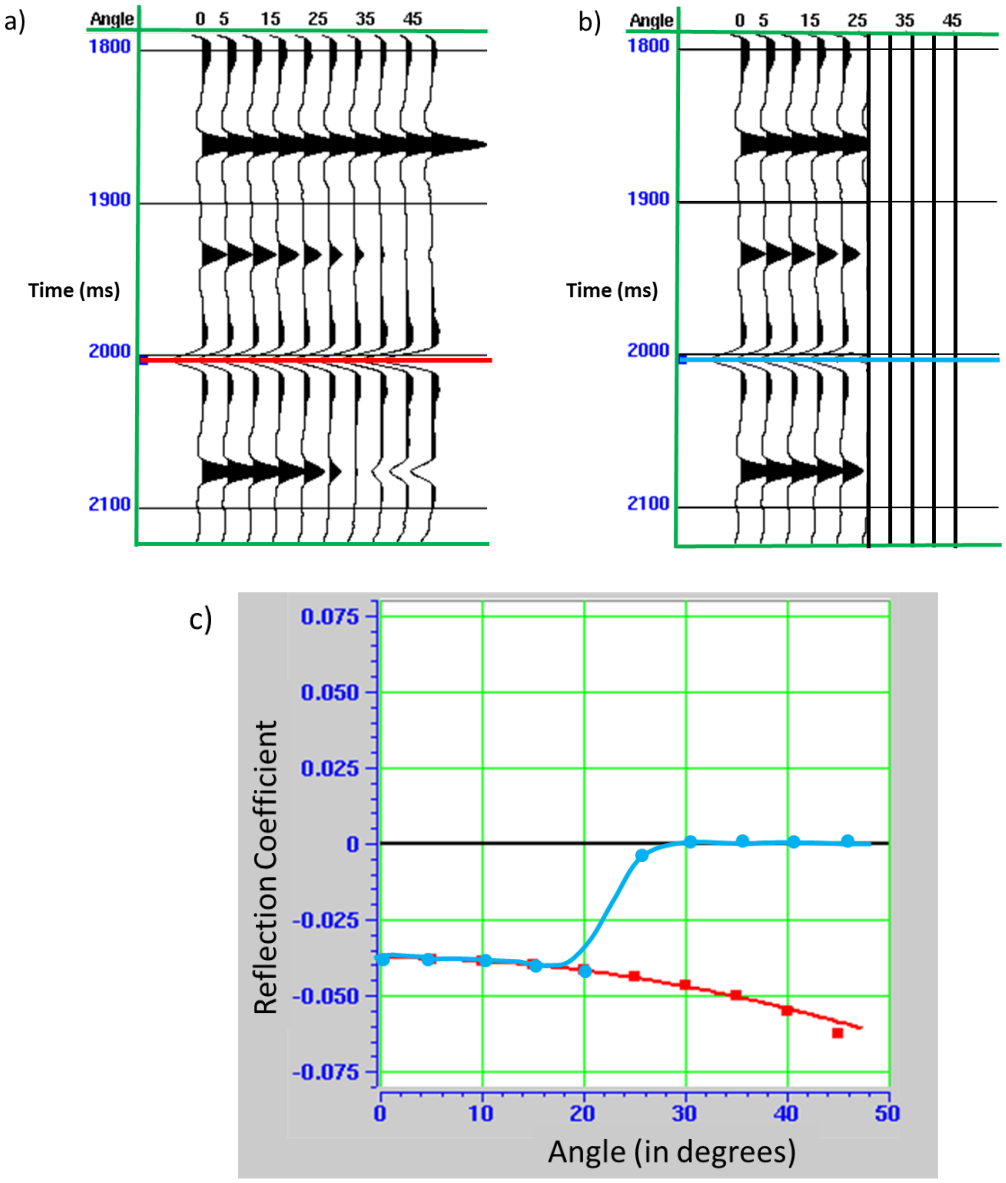

Figure 2.5. (a) Synthetic gather generated at a well, with angles ranging between 0°-42°. (b) Synthetic gather generated at a well, with offset range 0°-22°, and padded with zero traces from 24° -42°. (c) Extracted amplitudes corresponding to the red and cyan picks in (a) and (b).

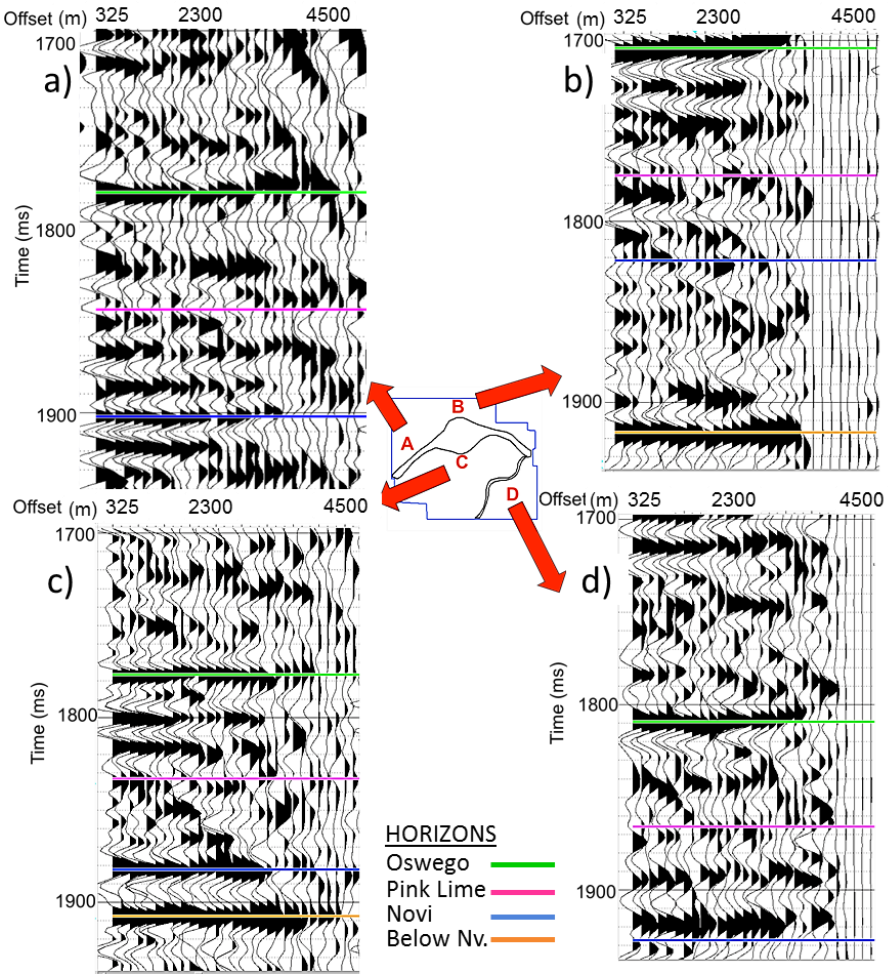

Figure 2.6. Representative gathers and base map indicating their locations. Note that location A and D have moderate amplitudes while B and C have low amplitudes at the farther offsets. The small residual amplitudes beyond these ranges are due to migration swings from the longer offset surveys.

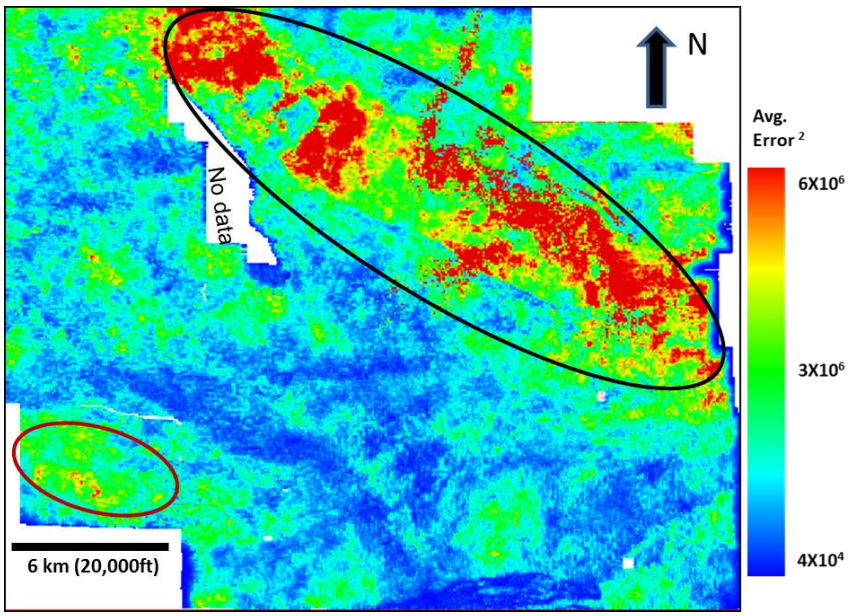

Figure 2.7. Mean-squared error map showing the difference between the measured and modeled seismic gathers for the 2°–42° inversion.

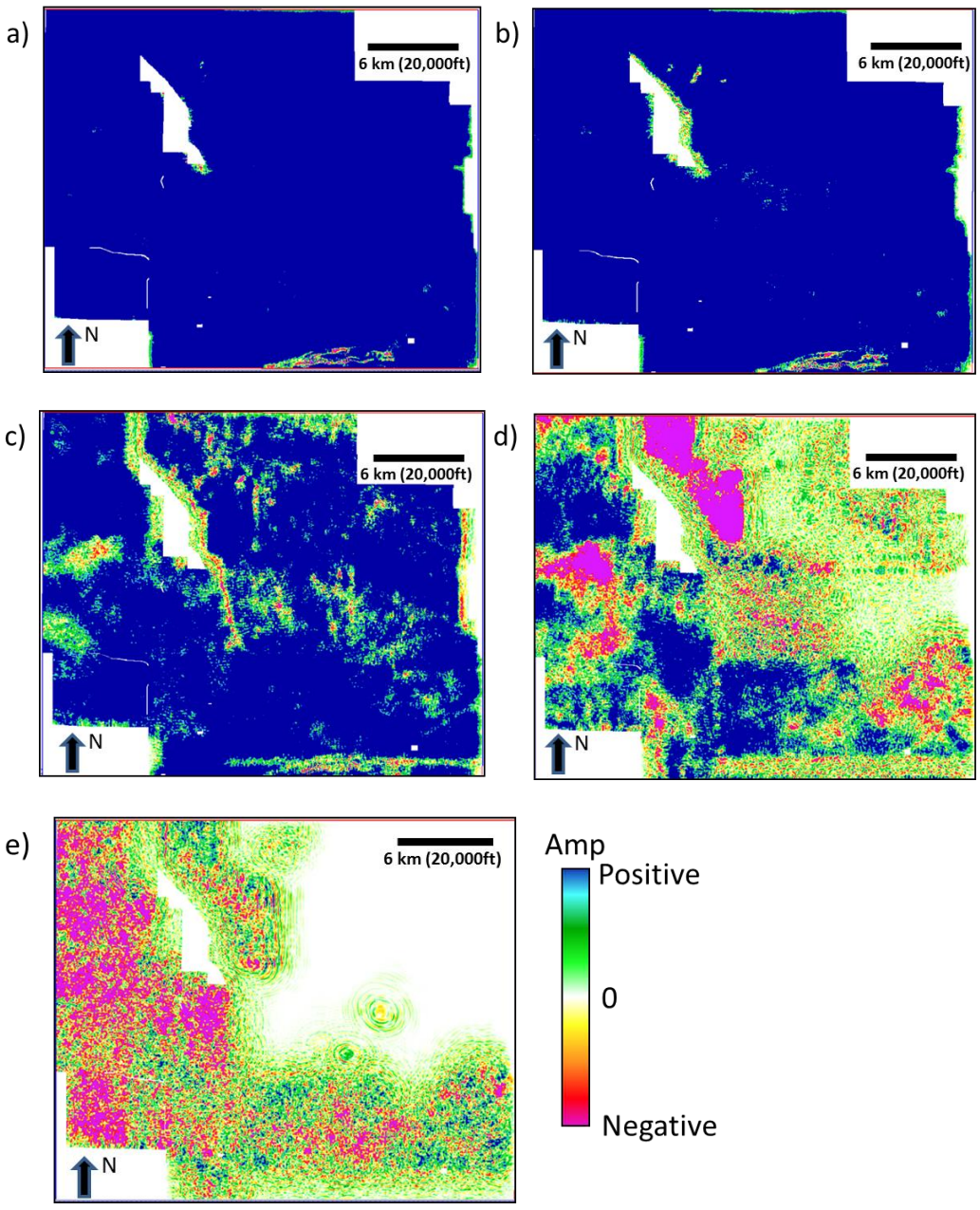

Figure 2.8. Horizon slices along the Oswego surface through offset-limited stacked amplitude volumes: (a) 0-1520 m (~0-5000 ft) (b) 1520-2450 m (~5000-8000 ft) (c) 2450-3350 m (~8000-11,000 ft) (d) 3350-4250 m (~11000-14000 ft) and (e) 4250-5200 m (~14000-17100 ft). The Oswego Lime was interpreted as a strong peak in the stacked seismic volume. Amplitude changes in c may be valid AVO effects. Often, inaccurate velocities (including anisotropic effects) result in misaligned gathers giving rise to zero crossings and troughs at far offsets. However, note how the amplitude approaches zero in the top right corner of the megamerged survey in (d) and (e) indicating that these large offsets were never recorded in these areas. White polygons in (c) indicate amplitude anomalies that will be used in subsequent quality control. White arrows indicate the major highways.

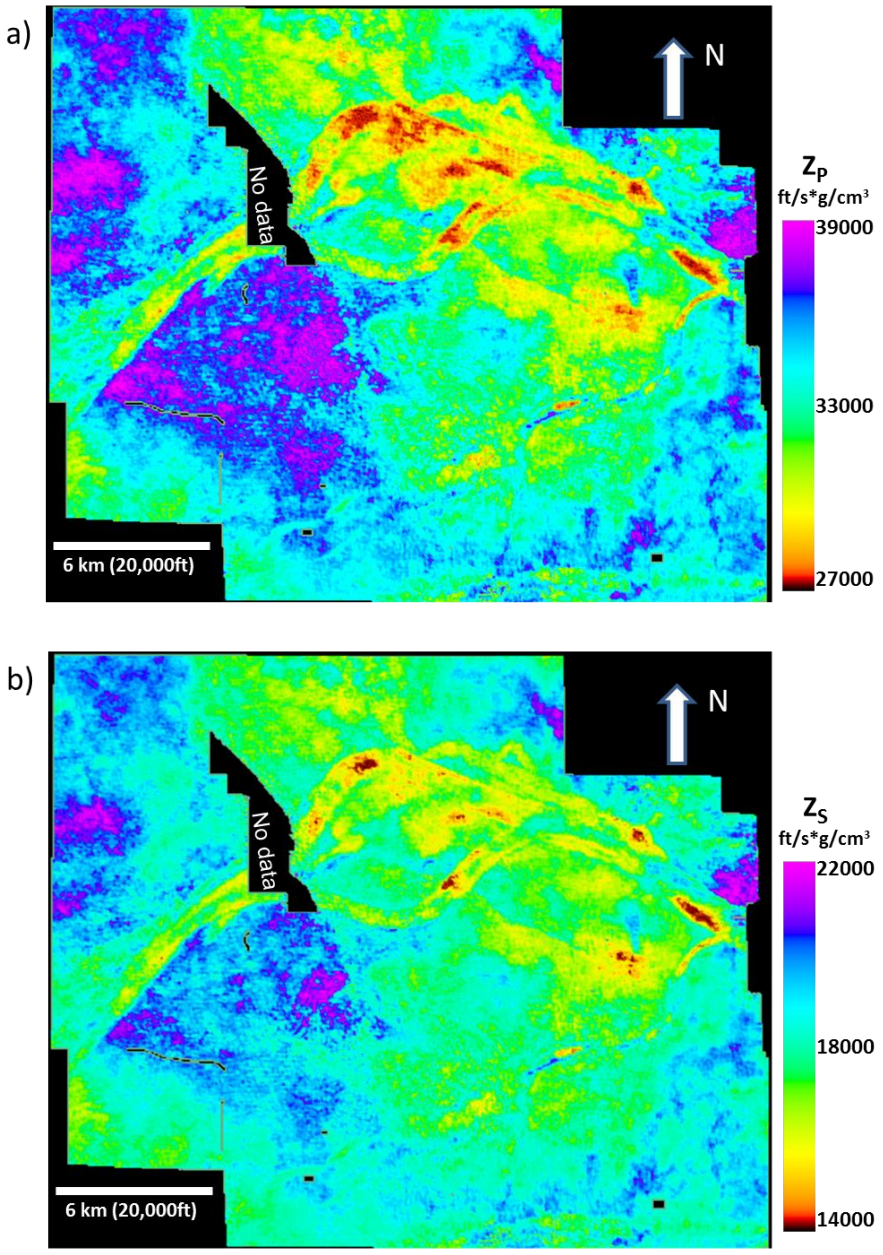

Figure 2.9. Phantom horizon slices 80 ms below the Oswego through (a) the P-impedance volume, Z_P, (b) the S-impedance volume, Z_S, computed from 2°-22° input migrated gathers. Pink polygons correspond to an area of high error shown in Figure 2.10.

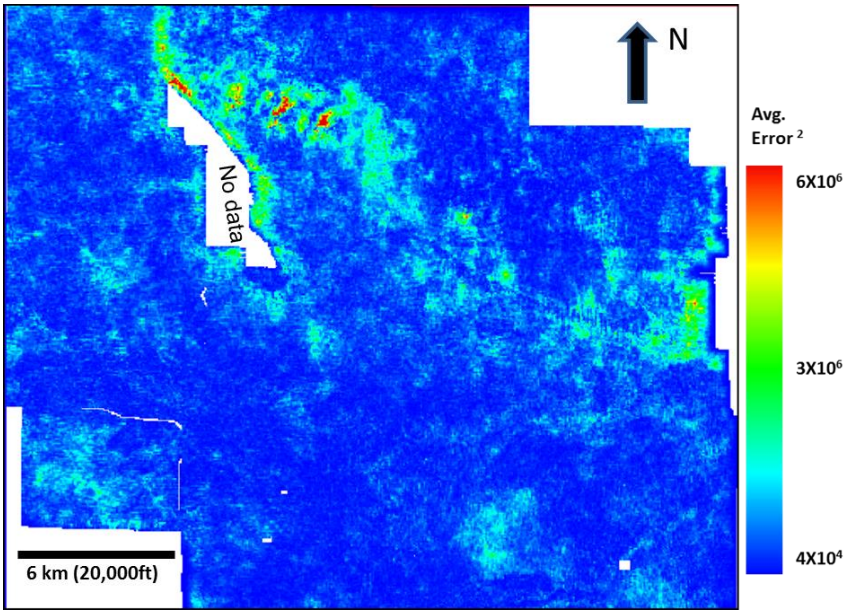

Figure 2.10. Mean squared error map showing the difference between the measured and modeled seismic gathers for the 2°-22° inversion. To compare with Figure 6 the squared error was normalized with respect to the number of traces in each gather. White arrow corresponds to those drawn about amplitude anomalies shown in Figure 8c. Pink polygons encircle an area of high error that is posted on Figure 2.9.

REFERENCES

Aki, K., and P. G. Richards, 1980, Quantitative seismology: Theory and methods, Freeman and Co., New York.

Barber, R., K. J., Marfurt, 2010, Challenges in Mapping Seismically Invisible Red Fork Channels, Anadarko Basin, Oklahoma, The Shale Shaker, **61**, 147-163.

Clement, W., 1991, East Clinton Field-U.S.A. Anadarko Basin, Oklahoma: AAPG Special Volumes, **TR**: Stratigraphic Traps II, 207-267.

Del Moro, Y. P., A. Fernandez-Abad, and K. J. Marfurt, 2013, Why Should We Pay For A Merged Survey That Contains the Data We Already Have? An Oklahoma Red Fork Example, The Shale Shaker, **63**, 336-357.

Del Moro, Y.P., 2012, An integrated seismic geologic and petro-physical approach to characterize the Red fork incised valley fill system in the Anadarko basin: Oklahoma: MS thesis, The University of Oklahoma.

Fatti, J. L., Smith, G. C., Vail, P.J., Strauss, and P. R. Levitt, 1994, Detection of gas in sandstone reservoirs using AVO analysis: A 3-D seismic case history using the Geostack technique. Geophysics, **59**, 1362-1376.

Goodway, B., T. Chen, and J. Downton, 1997, Improved AVO fluid detection and lithology discrimination using Lame petrophysical parameters; ‘λρ', ‘μρ', & ‘λ/μ fluid stack' from P and S inversions: 67th Annual International Meeting, SEG, Expanded Abstracts, 183-186.

Hampson, D. and B. H. Russell, 1990, AVO inversion: Theory and practice. 60th Annual International Meeting, SEG, Expanded Abstracts, 1456-1458.

Hampson, D. P., B. H. Russell, and B. Bankhead, 2005, Simultaneous inversion of pre-stack seismic data: 75th Annual International Meeting, SEG, Expanded Abstracts, 1633-1637.

Northcutt, R.A., and J. A. Campbell, 1988, Geologic provinces of Oklahoma, Oklahoma Geological Survey. accessed Feb 4, 2013; http://www.faqs.org/sec-filings/111201/North-Texas-Energy-Inc_S-1/ex99-1.htm#b.

Peyton, L., R. Bottjer, and G. Partyka, 1998, Interpretation of incised valleys using new 3D seismic techniques: A case history using spectral decomposition and coherency: The Leading Edge, **17**, 1294-1298.

Plessix, R. E., and J. Bork, 2000, Quantitative estimate of VTI parameters from AVA responses, Geophysical Prospecting, **48**, 87–108.

Russell, B., D. Hampson, and B. Bankhead, 2006, An inversion primer: CSEG Recorder, Special issue, 96-103.

CHAPTER 3 : SEISMIC MODELING

CALIBRATION OF ATTRIBUTE ANOMALIES THROUGH PRESTACK SEISMIC MODELING

[1]Sumit Verma, [2]Onur Mutlu, [1]Thang Ha, [1]William Bailey, and [1]Kurt J. Marfurt

[1]The University of Oklahoma, ConocoPhillips School of Geology and Geophysics.

[2]Turkish Petroleum,Ankara , Turkey.

This paper is submitted to SEG journal Interpretation and is under 2nd revision.

ABSTRACT

Seismic modeling is commonly used to determine subsurface illumination of alternative seismic survey designs, in the calibration of seismic processing and imaging algorithms, and in the design of effective processing workflows. Seismic modeling also forms the mathematical kernel of impedance inversion and is routinely used to predict the AVO response as a function of rock and fluid properties. However, the use of seismic models in seismic attribute studies is less common. We present four case studies where 2D synthetic common shot gathers were computed (acoustic or elastic) and processed (including migration) to evaluate alternative interpretation hypothesis. Modeling showed that, the lack of continuous coherence anomalies in a faulted Chicontepec Basin survey were due to overprinting by coherent interbed multiples. Attributes computed from the resulting processed model data show that subtle curvature anomalies in a Mississippi Lime survey were due to karst collapse rather than to velocity pushdown related to vertical gas migration. Impedance attributes computed from a Woodford Shale model favor the hypothesis of increased porosity correlated to the occurrence of subtle faults

rather than amplitude dimming due to poor fault imaging. Finally modeling of a fractured basement survey in the Texas Panhandle survey showed that, aggressive headwave suppression preserved the basement fracture response while increasing the signal to noise ratio. Seismic attribute study on seismic models helped significantly to determine between the two alternative hypothetis in our case studies.

INTRODUCTION

Seismic modeling has been used as a tool to help seismic acquisition survey design (Cordsen et al., 2000), to quantify subsurface illumination as a function of offset and azimuth (Fagin, 1991), to calibrate processing algorithms as well as workflows, and to calibrate and justify the use of alternative seismic velocity analysis and migration algorithms (Versteeg, 1994). Seismic modeling is routinely used in rock physics fluid substitution to predict the AVO response (Russell et al., 2001). Seismic modeling is also used in understanding the feasibility of 4D seismic acquisition (Mukherjee et al., 2012).

The use of seismic modeling to calibrate and interpret seismic attributes is less common. Hart and Chen (2004) used simple 1D acoustic convolutional models constructed from well control to validate the subsequent interpretation of seismic attribute anomalies. Clawson et al. (2003) computed 3D convolution models from an outcrop-generated 3D interpretation of a Brushy Canyon turbidite system. He then computed coherence, P-impedance, and other attributes from the modeled seismic data to determine which attributes may help in the seismic prediction for improved hydrocarbon reserve estimation.

The generation of 3D common shot gathers is computationally intensive, and their use is presently limited to major oil and service companies, or collaboration through a modeling consortium (Fehler, 2012). Conversely, the generation of 2D acoustic and elastic models can be computed on modern desktop computers using commercially available software. In this paper, we show examples using such software to answer specific questions about the attribute response to alternative geologic hypotheses. Specifically, we use 2D models to quantify the response of coherence, curvature, and acoustic impedance through four case studies.

Coherence and curvature are widely used attributes in structural interpretation. Coherence measures the similarity of the seismic waveform within analysis window using cross-correlation, semblance, eigen structure (Chopra and Marfurt, 2007). In this paper we have used eigen structure coherence along the reflector dip. Curvature is a measure of the deviation of the reflector surface from a plane (Chopra and Marfurt, 2007). Murray (1968) correlated curvature to fracture-enhanced production while McQuillan (1974) correlated fracture patterns to basement-controlled lineaments. Al-Dossary and Marfurt (2006) expanded these ideas to volumetric computations. In the first case study we calibrate curvature and coherence attributes through seismic modeling to understand the tectonic structures of a structurally-complex Chicontepec Basin. Mai (2010) described lateral relationships between coherence and curvature, in order to give a better understanding of the complex geology of the Chicontepec Basin. Pena (2010) used coherence and curvature attributes to map igneous bodies in the Chicontepec Basin. However, many faults clearly identified on seismic amplitude vertical sections are not delineated by coherence. We will model two cross sections to determine why.

The second case study addresses the Woodford Shale in Oklahoma where fractures play a very important role. Open fractures provide porosity as well as permeability, while hydraulic fracturing can often open previously healed fractures creating good permeability as well. Staples (2011) found intense natural fractures in the Hunton Limestone correlated with curvature. Nissen et al. (2009) found that diagenetically altered fractures in the Mississippi Lime were filled by the overlying Pennsylvanian Cherokee Shale. Baruch et al. (2009) found increased accommodation space and differential compaction of the Barnett Shale lying above the karsted Ellenburger Dolomite in the Fort Worth Basin. Similar features were observed by Gupta et al. (2013) and Guo et al. (2010) in the Woodford Shale overlying the Hunton Limestone reflectors. While seismic amplitudes adjacent to large faults are often inaccurate due to limited migration aperatures and inaccurate velocities, the faults imaged by Guo et al. (2010) often exhibited offsets less than ¼ wavelength. In this paper, we generate, process, image, and invert a suite of prestack seismic models to determine whether the anomalies are seismic artifact or geologic feature of interest.

Our third case study uses modeling to evaluate alternative hypotheses of sags seen over karst collapse features in a Fort Worth Basin survey – are they structural karst collapses or a pushdown effect due to overlying gas chimneys? Discriminating these two hypotheses can be critical to guide horizontal wells so they reach the reservoir.

The fourth case study is different in that we know from well control that fractures in the basement exist. In this Texas Panhandle oil and gas field, the high velocity basement is overlain by a high velocity Permian Evaporite and then low velocity Mesozoic clastics, resulting in two rock units that give rise to strong headwave

generation. We also observed strong linear events cutting the shallow basement reflections and diffractions of interest. In this example we create seismic models to calibrate an aggressive processing workflow that suppresses headwaves and preserves the deeper diffractions that image the basement fractures.

The unifying principle in all four case studies is that seismic attributes are a function not only of the impedance contrasts but also of the signal-to-noise ratio of the data after processing that include prestack migration.

METHODS

We used commercial software, which grids a 2D geological model and then uses the finite difference method to solve the wave equation to generate synthetic seismic data. Figure 3.1 shows the flowchart used for generating synthetics. First, we create a simple geologic cross-section based on real seismic data. We choose the velocity, density and depth of formations from well logs. We simplify the geology other than the target features to be modeled. Next, we define parameters for the target feature of interest (e.g. fault's throw, karst width and thickness). We choose the number of source points, source spacing, receiver points and receiver spacing similar to the real data (Table 3.1). We then propagate a wave field through the 2D geological model creating synthetic shot gathers. Last, we process the synthetic seismic data through prestack migration and stack the migrated data to obtain the final results.

CASE STUDIES

CASE STUDY 1: SEISMIC MODELING OF CHICONTEPEC BASIN'S TECTONIC STRUCTURE

Chicontepec Basin, discovered in 1925, is one of the most productive basins in Mexico. It is a structurally complex basin, and the tectonic evolution controlled the influx and deposition of the tight sand turbidite reservoir. The deeper and interfingered shale source rock is a potential unconventional resource play (Sarkar, 2011). Time slices and horizons through seismic attributes such as coherence and curvature derived from a 3-D seismic volume helps visualize the tectonic deformation within and below reservoir. These attributes allow us to map faults, fractures, channels, folds, pop-up structures, horsts and grabens, and other geologic features (Figure 3.2 and Figure 3.3). Murray (1968) correlated curvature to fracture-enhanced production; McQuillan (1974) correlated fracture patterns to basement-controlled lineaments.

The seismic expression of tectonic structures in the Chicontepec Basin is a function of the acquisition parameters, seismic wave propagation, imaging and the underlying geology. While there are areas of low fold and poor data quality due to shallow volcanics (Pena et al., 2009), overall data quality is quite good. We generated two seismic models to investigate the performance of coherence in delineating the faults seen in Figure 3.3. Results were somewhat deceiving in that they did not delineate faults that were clearly identifiable by a human interpreter (Figure 3.2). To better understand this result, we used a commercial finite difference wave-equation modeling software package to evaluate representative pop-up and graben structures. We construct both models with

parallel bedding geometries and no significant thickness changes along the beds in order to make the model geologically consistent to those seen in the Chicontepec Basin. Simplification, such as reducing the number of layers, aids in extracting key information from the seismic modeling and imaging workflow. Through this simplification, key geological features can be more easily identified on real data. Survey parameters (Table 1) were kept similar to those used in the real seismic survey. In both acoustic models, we use a Ricker wavelet with 25 Hz dominant frequency as the source wavelet, and generate raw common shot gathers. These common shot gathers are then prestack time and depth migrated using a Kirchhoff migration algorithm. Finally, seismic attributes are computed on both models, and the results compared to those computed from the real data. The values of the P-wave velocity and density are taken from a well log in the survey (Figure 3.4a).

Seismic modeling of a pop-up structure

The pop-up model shown in Figure 3.4b is constructed based on a cross section through the 3D seismic survey shown in Figure 3.2 and Figure 3.3. In the model, there are two symmetric reverse faults on either side of the pop-up block. Both faults have a 25 m (83 ft) throw. The units above the top Paleocene level horizon are deformed, but not faulted. On the other hand, the units below the top Paleocene are deformed and faulted. We assume that formation velocities increase with depth. Figure 3.5a shows the prestack depth migrated (in time) seismic sections of the pop-up model. The thin-bedded turbidites give rise to significant interbed multiples.

We computed seismic attributes on the depth migrated section as it provided a better image than the time migrated section. While time migration works well for smooth velocities and flat reflectors, it cannot handle sudden velocity changes in the overburden. In contrast, depth migration uses a more exhaustive interval velocity model, and accurately handles velocity changes. Snapshots of seismic wavefronts (Figure 3.4d) help to verify if a recorded reflection is a primary or a multiple. Figure 3.5b shows that the reflector dip (Marfurt , 2006) has higher values at the edges of the pop-up structure. Figure 3.5c shows that 2D curvature has positive values at the inside edges of the pop-up structure and negative values at the outside edge of the pop-up structure. Figure 3.5d shows that (unlike the curvature and dip) coherence anomalies are absent in the shallower part where the strata are folded but not faulted. We do see low coherence anomaly in the lower faulted region. Although the fault inclination and placement are not exactly the same, the results computed from the model are quite similar to the results computed from the real data, thereby quantifying our interpretation of the attribute anomalies.

Seismic modeling of a graben structure

The graben model shown in Figure 3.4c is constructed from the vertical slice through the actual seismic survey shown in Figure 3.3b. In the graben model, the thickness of units, P-wave velocity and density values are kept the same as those used in the pop-up model. There are two symmetric normal faults on either side of the graben structure. Both faults have a 25 m (83 ft) throw. The units above the top Paleocene level horizon are not deformed or faulted, while the units below the top Paleocene are faulted. We assume that velocity increases with depth. Figure 3.6a shows the prestack depth

migrated (in time) seismic sections of the graben model. Figure 3.6b shows that the reflector dip has higher values at the edges of the graben structure. Figure 3.6c shows 2D curvature has negative curvature at the inside edge of the graben structure and has positive values at the outside edge of the graben structure. Figure 3.6d shows discontinuous coherence anomalies in the lower faulted region.

The results of both the pop-up as well as graben models are quite similar to the real 3D seismic data thereby, validating our interpretation of the attribute anomalies.

Discussion of results for case study 1

Synthetic seismic modeling confirms that the pop-up and graben structures in the Chicontepec area give rise to coherence and curvature anomalies. Seismic modeling results are similar to those from the real data. Synthetic modeling gives us an idea of how the pop-up and graben structures in the area look like in reality. Specifically, it shows how continuous interbed multiples break up curvature and coherence anomalies that would otherwise be continuous. This allows us to recognize such anomalies as an artifact, not as geology, thereby preventing a potential interpretation pitfall.

CASE STUDY 2: SEISMIC MODELING OF IMPEDANCE ANOMALIES ASSOCIATED WITH FAULTS IN THE WOODFORD SHALE

Guo et al. (2010), working on a Woodford survey in the Arkoma Basin and Gupta et al. (2013), working on a Woodford survey in the Anadarko Basin both noted a strong correlation between lows in acoustic impedance and subtle structural lineaments seen in the most-negative principal curvature (Figure 3.7). These lineaments can be enhanced by computing 1) 2^{nd} derivatives along structural dip and azimuth and 2) the magnitude and strike of the most-positive and most-negative 2nd derivative changes, or "amplitude curvature" (Chopra and Marfurt, 2013). In both cases, the Woodford Shale directly overlies the fractured and karsted Hunton Limestone. The simplest geologic hypothesis is that these fractures and faults continue into the overlying Woodford, thereby increasing permeability. Supporting this hypothesis is the lack of correlation between positive curvature lineaments and impedance. The alternative hypothesis is that 3D pre-stack time migration does not accurately reconstruct the amplitudes around the faults. While such imaging artifacts do occur for faults with large vertical throws (or steep dips) and limited migration apertures, the throw seen in Figure 3.7a is so small that we hypothesize the amplitude variation to be geological. We therefore construct two simple seismic (acoustic) models to evaluate the hypotheses mentioned above.

As in case study 1, we use a commercial finite difference wave equation modeling software package to evaluate the fault imaging artifact versus the fracture/diagenetic alteration hypotheses. Model parameters were kept the same in the both models (Table 3.1). We setthe Woodford Shale top at a target depth of 914 m (3000 ft), resulting in incident angles up to 40^{o}. These common shot gathers were then prestack time and depth

migrated using a Kirchhoff migration algorithm, with the later using travel times computed using a first arrival eikonal solver. In both models, we used a Ricker wavelet with 60 Hz dominant frequency as the source wavelet. Seismic attributes were extracted and an acoustic impedance inversion was computed on both models. The P-wave velocity, S-wave velocity and density values were taken from a typical log of the area (Figure 3.8a).

The Fault Model :

We prepared a fault model with four faults in the Woodford and Hunton layers, at regular offset intervals (Figure 3.8b). The faults were kept as simple vertical fault with throws ranging between 6 m (20 ft) to 24 m (80 ft). We terminate the faults at the top of the Woodford Shale (green unit). The faults with throws of 12 m (40 ft) and higher can be identified on the time-migrated seismic amplitude (Figure 3.9a) and the coherence (Figure 3.9b), whereas all the faults are visible on the curavature (Figure 3.9c). The acoustic impedance (Figure 3.9d) shows quite smooth varitions near the faults.

The Fracture Model :

We prepared a fracture model with variable numbers of fractures that begin in the Hunton Limestone (blue unit) and terminate in the middle Woodford Shale (green unit) (Figure 3.10a). All of the fracture zones are 6 m (20 ft) wide and 91 m (300 ft) in height, and have low velocity and density values. On the time-migrated seismic section, highly fractured areas (4 and 8 fracture zones) can be identified easily, while the less fractured areas (1 and 2 fracture zones) are harder to identify because of the limited seismic

resolution (Figure 10a). Curvature was able to detect all the modeled fractured zones (Figure 3.10c). In contrast to the fault model, the changes in acoustic impedance (Figure 3.10d) allowed us to identify the fracture zones easily and accurately.

Discussion on results for case study 2

Seismic modeling confirms our hypothesis that the impedance anomalies seen in the two surveys are not due to a processing artifact of fault imaging but rather correlated to fracturing (or may bekarsting) in the underlying Hunton Limestone. Operators in Oklahoma frequently drill horizontal wells in both formations. In the Hunton, they look for natural fractures and complete the wells with acidation. In the Woodford Shale, most operators attempt to define the strike of natural fractures and maximum horizontal stress to optimally place and orient their wells, completing them with hydraulic fracturing. We suspect these two reservoirs to be coupled, thereby providing opportunities for more innovative completion strategies. Modeling therefore confirms the hypothesis that the low impedance lineaments associated with small faults are associated with a fractured or otherwise diagenetically altered low zone rather than limitations in seismic imaging.

CASE STUDTY 3 : MODELING SAGS - ARE THEY KARST COLLAPSE OR GAS CHIMNEYS PUSHDOWN?

Seismic interpretation can be ambiguous in certain cases, due to alternative geologic causes of the resulting seismic image. Karst features have an easily identifable seismic signature (Qi et al., 2014). In some cases, poor resolution in the shallower section

(e.g. Story et al., 2000) is due to a gas chimney associated with deeper karst, such that the incoherent expression of the karst collapse is due to velocity pushdown and inaccurate seismic focussing (Figure 3.11). In karst collapse seen in the Ellenburger Dolomite of the Fort Worth Basin (e.g. Sullivan et al., 2006; Kwatamadi et al., 2014) the shallower Marble Falls, Atoka, and Caddo reflectors are also deformed, but well focused using a laterally smooth time migration velocity, suggesting that the depressions are structural lows rather than velocity pushdown artifacts. These two hypotheses can produce identical seismic images using a 1D convolutional acoustic model. To better understand these events on seismic images and attributes we create prestack wave equation models to observe karst and gas chimney effects on wave propogation and to observe the results on the processed stacked data. Specifically, we expect that long source-receiver offsets will undershoot a gas chimney and provide a different (conflicting) image than that of a collapse feature.

Karst Collapse Model:

We model karst collapses based on the seismic cross section shown in Figure 3.12 from a seismic survey in the Fort Worth Basin (Sullivan et al., 2006). The area has many karst collapse features that are well imaged by the 3D seismic data. We then constructed a model with a structural collapse at the top Ellenburger Dolomite filled with the Barnett Shale (Figure 3.13a).

Gas Chimney model:

For the gas chimney model we assume that the top of the karsted Ellenburger Dolomite was structurally flat and the "collapse feature" was an artifiact of velocity

pushdown due to an overlying gas chimney similar to that seen in Figure 3.11. To build prepare the gas chimney model, the karsts were replaced with a vertical column of low velocity "gas-charged" rock. The velocities in the chimney model of Figure 3.13b were chosen to construct the same 1D convolution model as the structural collapse of Figure 3.13a and Figure 3.14a. The gas chimney model took several iterations to attain the desired results. The difficulty came in creating a gas chimney that extended through all of the desired layers while still maintaining the underlying layer boundaries (Figure 3.13b and Figure 3.14b). The modeled synthetic gathers were prestack time migrated using a laterally smooth velocity model that ignored the chimney in order to imitate a typical processing workflow in the Fort Worth Basin (Fernandez, 2013).

Discussion on results for case study 3

The resulting migrated and stacked images bear a close resemblance to the actual seismic data (Figure 3.12). One noticeable difference are the migration artifacts associated with the gas chimney model. The velocity pushdown at the top Ellenburger is both smoother and less focused than the input model. It is also consistent with the misalignment of ray paths traversing vertically through the chimney versus those that undershoot the chimney from its flanks. There are also diffractions and a complex velocity pushdown at the base of the Ellenburger Dolomite that are not evident in the karst collapse model or in the real data.

Alai et al. (2011) described the elastic wave field propagation through gas clouds that are similar to the gas chimneys that we have modeled with acoustic wave field. The key to this observation is that the pushdown effect will continue into the deeper medium

below the gas chimneys. This is an effect we can expect to see from all gas chimneys. Structural collapse can cause a similar behavior, such as the low velocity sand filled karst of the Tarim Basin (Zhao et al., 2014). The Barnett Shale fill also has a high velocity similar to that of the Ellenburger Dolomite. Furthermore, Sullivan et al. (2006) show that the shallower isochrons are smooth across the karst with no local temporal thickening due to a gas chimney, suggesting that the karst collapse occurred after the shallower layers were deposited.

CASE 4 : IDENTIFYING PROCESSING CHALLENGES WITH SEISMIC MODELING

Our final example is more traditional in that we use modeling to aid in the selection of processing parameters. The study area is located within the Texas Panhandle oil and gas field where wells have encountered hydrocarbons in basement fractures. These fractures are charged by fluid migration from deeper sedimentary source rocks in the Anadarko Basin to the North and East. The basement fractures are well imaged by seismic attributes such as curvature and coherence (Figure 3.15) as well as by P-wave impedance. Our goal was to design a workflow that preserved the amplitude response at far offsets to facilitate a prestack inversion to better differentiate weathered and fractured basement from tighter rocks. The high velocity basement is overlain by slower clastics and then by a very high velocity Permian Evaporite, with a final layer of low velocity Mesozoic sediments. Both the basement and Permian Evaporite give rise to strong P- and S-

headwaves that overprint the shallow (2500 ft deep, equivalent to t=0.57 s) basement reflections and diffractions of interest.

Ground roll and air waves were successfully removed, and the evaporite and basement provided good refractors for tomographic inversion, as seen by Xu (2014), we decided to model the possible impact of these refraction events on the processing of reflections.

To better understand the effect of noise, we generated a synthetic shot gathers using a simple, flat-layered model with hypothesized fractures within the basement (Figure 3.15a). The elastic modeled gather (Figure 3.17b) is highly contaminated by reverberations in the weathering zone. For the real data (Figure 3.17c), the weathering zone has higher attenuation, thereby damping waves reverberating within it. Thus, we created an additional model without the weathering zone (Figure 3.16b) as well as a simpler model without fractures. Acoustic-modeled gathers with diffractions, without diffractions, and their difference, are shown side-by-side in Figure 3.18.

To further interpret the modeled gathers, we also generated several snapshots of the acoustic wave field. By alternatively examining the snapshots and the surface seismic acoustic-modeled gather, we were able to correlate and thereby identify noise and signal, and then mark those events on the acoustic-modeled gather, elastic-modeled gather, and real shot gather (Figure 3.17a- c). Acoustic gathers are synthetic gathers that contain only P-wave information. They are simple and good for interpreting primary reflections and some dominant multiples. Elastic gathers are synthetic gathers that contain P-wave, S-wave, and converted wave information, and thus resemble real gathers better than acoustic gathers, but may be too complicated to interpret. Real gathers are extracted from

the 3D-survey data set. Diffractions are only marked in the acoustic-modeled gather; they are overlain by reverberations in the elastic-modeled gather. Diffractions in real gathers are much less prominent than in synthetic gathers, suggesting that fractures in real life are of smaller scale than those in the model. At the target depth (t=0.57s), critical refractions from basement tangent to the reflections occur at offset h = 975 m (3200 ft) and must be muted prior to subsequent prestack inversion.

CONCLUSIONS

The attribute expression of the subsurface depends not only on the impedances and geometric configuration of the various facies, but also on the acquisition and subsequent processing and imaging of the seismic data. Unlike the classic convolutional model, prestack seismic modeling using the acoustic wave equation models both signal and noise. In our first case study our synthetic seismic modeling confirms that pop-up and graben structures in the Chicontepec area give rise to coherence and curvature anomalies. Seismic modeling results are similar to those from the real data. However, by using snapshots of the wavefront we are able to see that interbed multiples give rise to coherent, continuous reflections that overprint our faulted structures of interest. This overprinting disrupts what should otherwise be a continuous fault anomaly on the seismic section. In many areas of the survey, interbed multiples from the overlying volcanics are stronger than the reflection of interest. Modeling does not solve our problem, by removing the interbed multiples, but it helps to identify primaries and interbed multiples and motivates future processing workflows as well as quantifies the confidence we have in our attribute images.

Our next case study from the Woodford Shale of the Arkoma Basin of Oklahoma shows the conjugate situation, where we are concerned that the interpretation of low-impedance anomalies visually correlated with small-offset faults are artifacts of imaging. Here, seismic modeling confirms the geologic hypothesis that the impedance anomalies seen in the two surveys are correlated to fracturing and karsting in the underlying Hunton Limestone. We suspect these two reservoirs to be coupled, thereby providing opportunities for more innovative completion strategies.

Our third case study evaluates two geologic hypotheses of a karst collapse versus a gas chimney, for which a convolutional model would result in the exact same image. Prestack data with large source-receiver offset undershoot much of the hypothesized gas chimney, thus allowing us to differentiate the scenarios. The resulting images are different, with the gas chimney being a smoother, smeared, pushdown anomaly, and with the karst collapse being a surface with sharp edges as seen in the real 3D survey.

Our fourth and final case study is different in that we know from the well bore that there are hydrocarbon-bearing fractures in the shallow basement of a Texas Panhandle survey. Here, our problem was one of validating alternative processing workflows to preserve the fracture-generated diffractions while rejecting the strong overprinting coherent P- and S- headwaves. Modeling showed that we could not preserve the farthest offset ($>45^0$) data since the filtering contaminated the reflection of interest.

ACKNOWLEDGEMENTS

The wave equation modeling used in this paper was conducted using Tesseral 2D (Tesseral Technologies Inc. seismic modeling software package). Log analysis and seismic inversion were done using Hampson Russell's Geoview, elog and strata (by CGG). Display of the seismic data was done on Petrel (by Schlumberger). Real data are courtesy to PEMEX, CGG Veritas, Devon Energy and Cimarex. Funding for the research was provided by the industry sponsors of the Attribute-Assisted Seismic Processing and Interpretation (AASPI) consortium.

FIGURES AND TABLES

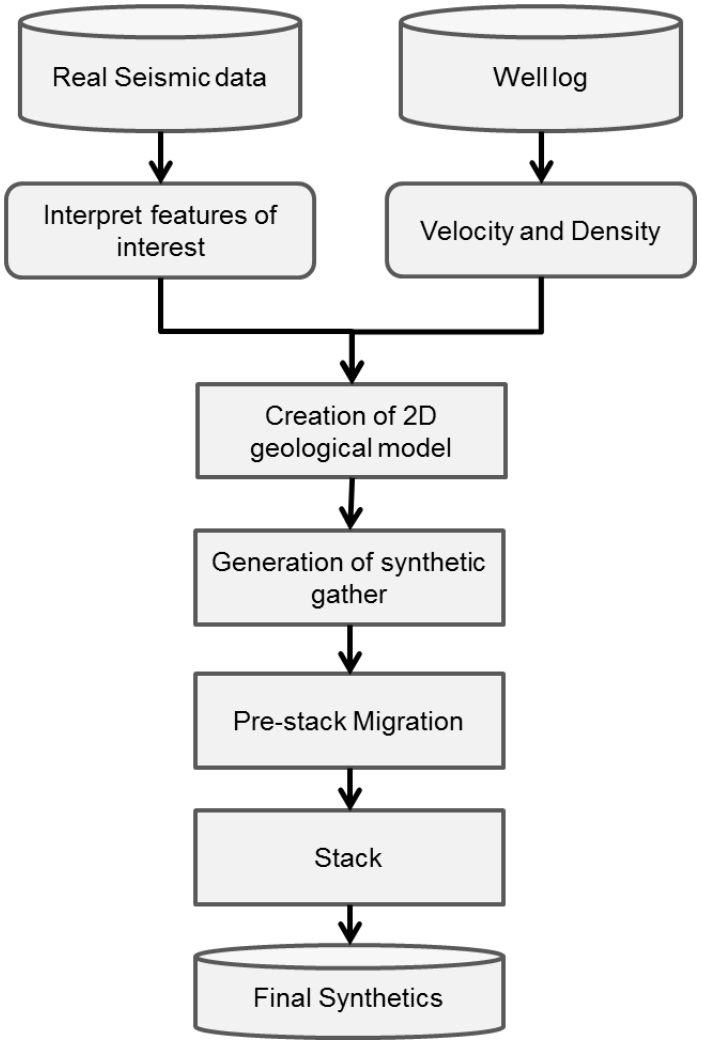

Figure 3.1 Flowchart for generation of synthetics.

Param. \ Model	Case 1	Case 2	Case 3	Case 4
No. of Source points	120	100	51	1
Source spacing	50 m (166 ft)	30 m (100 ft)	60m (200 ft)	-
No. of receiver points	240	100	200	100
Receiver spacing	25 m (83 ft)	30 m (100 ft)	15 m (50 ft)	16.5m (55 ft)
Cross section length	6096 m (20000 ft)	3048 m (10000 ft)	3048 m (10000 ft)	1676 m (5500 ft)
Modeling type	Acoustic	Acoustic	Acoustic	Acoustic and Elastic

Table 3.1 Survey geometry created for models.

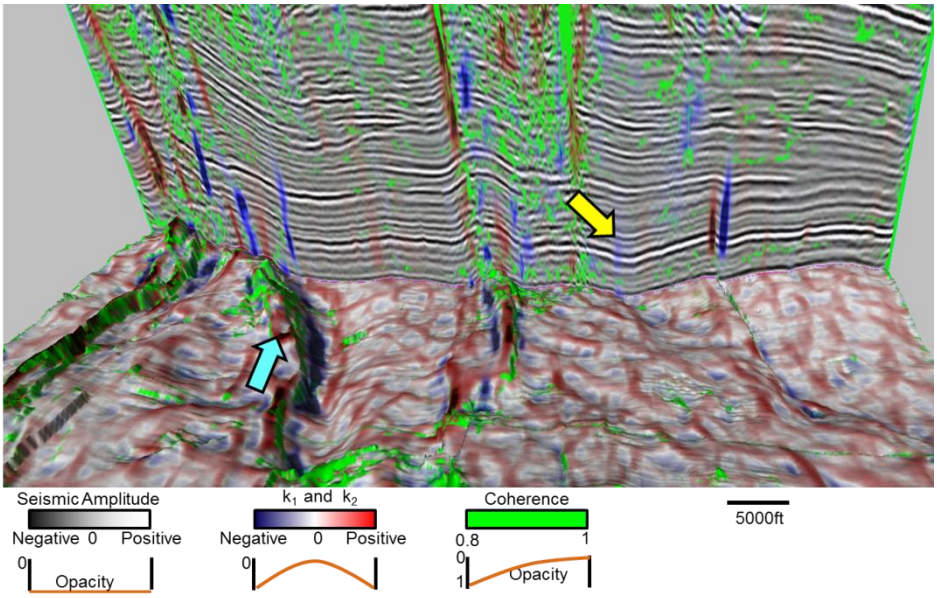

Figure 3.2 Horizon slice along the top Jurassic through co-rendered coherence, most-positive curvature, and most-negative curvature. The same three attributes are co-rendered with amplitude on the vertical slice, which shows a pop-up feature (yellow arrow) and a graben (cyan arrow). Although the edges of these features are well delineated by curvature, the coherence anomaly (in green) appears to be broken. In subsequent images, we will generate 2D models over these features to better understand the lack of a coherence anomaly. (Data courtesy of PEMEX).

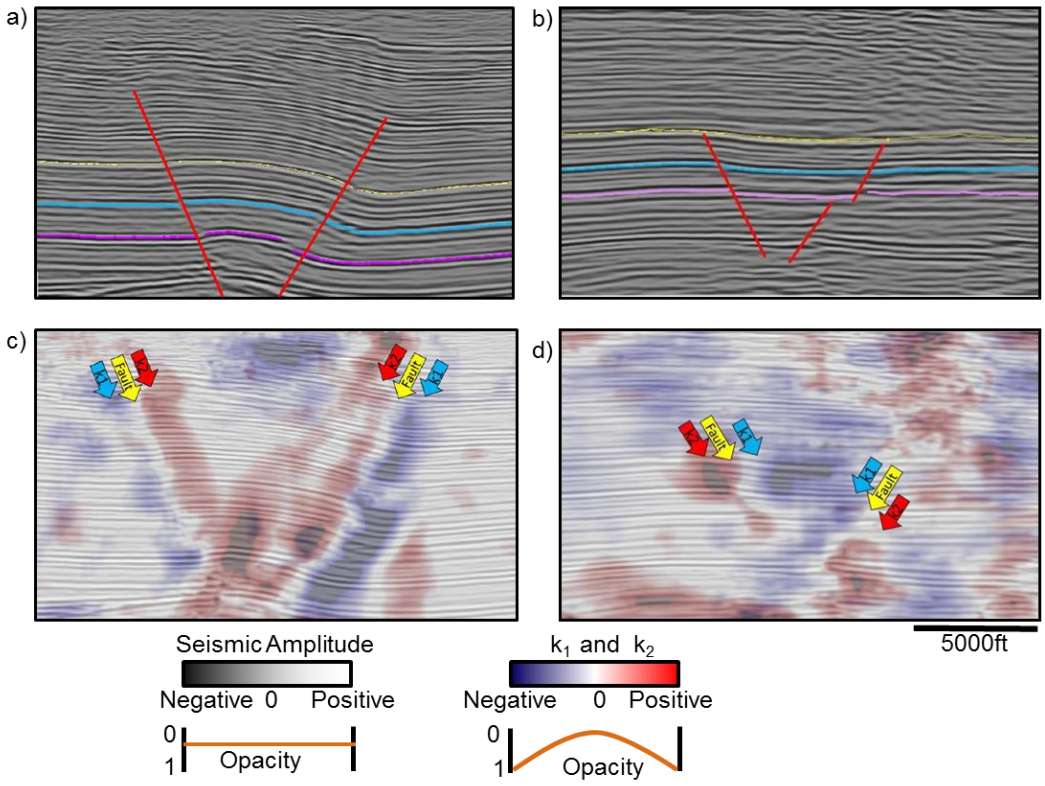

Figure 3.3 Vertical slices through the seismic amplitude volume through (a) a pop-up block and, (b) a graben previously shown in Figure 3.2. Fault traces are shown in by red lines. (c) and (d) The same images are co-rendered with most-positive and most-negative curvature. Figures displayed at 1:1 scale.

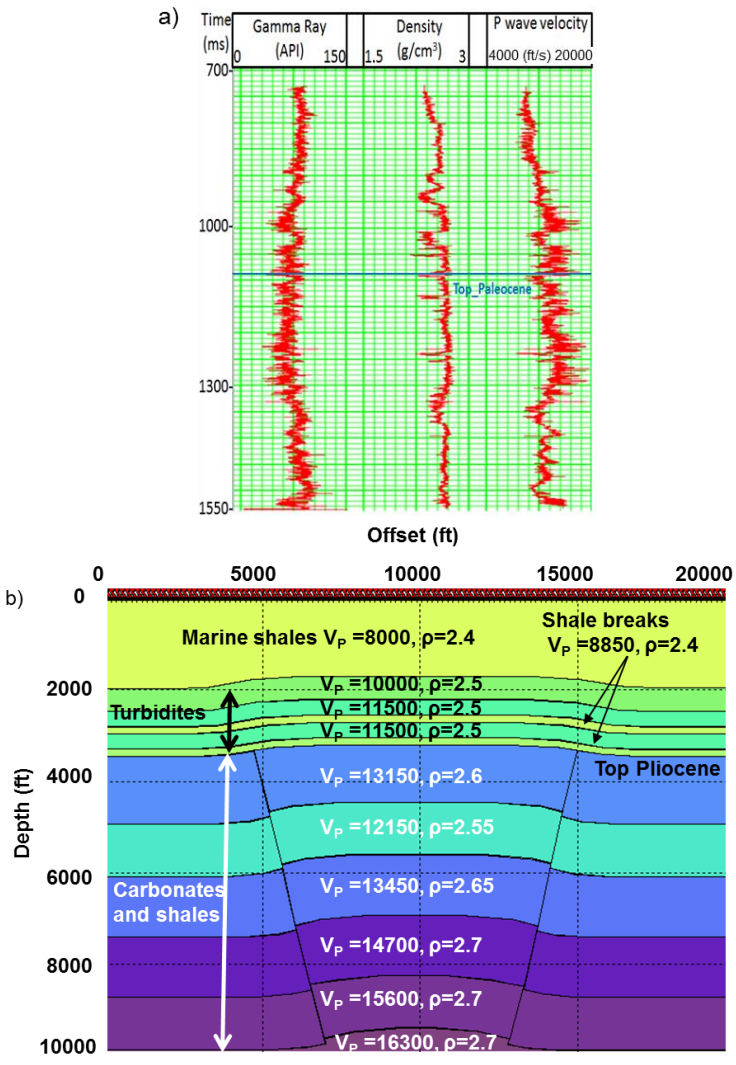
a)
Time (ms)
Gamma Ray (API)
0
150
Density (g/cm3)
1.5
3
P wave velocity
4000 (ft/s) 20000
700
1000
1300
1550
Top_Paleocene
Offset (ft)
b)
0
5000
10000
15000
20000
Depth (ft)
2000
4000
6000
8000
10000
Marine shales VP =8000, ρ=2.4
Shale breaks
VP =8850, ρ=2.4
VP =10000, ρ=2.5
VP =11500, ρ=2.5
VP =11500, ρ=2.5
Turbidites
Top Pliocene
VP =13150, ρ=2.6
VP =12150, ρ=2.55
VP =13450, ρ=2.65
Carbonates and shales
VP =14700, ρ=2.7
VP =15600, ρ=2.7
VP =16300, ρ=2.7

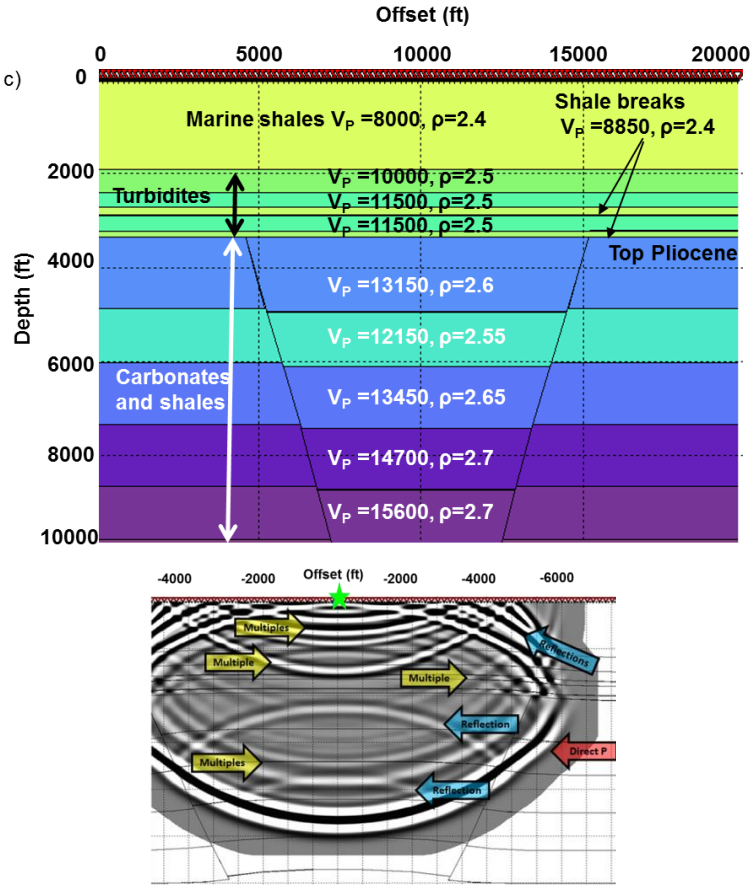

Figure 3.4 (a) A representative well in the study area showing gamma ray, density, and P-wave sonic logs. (b) The model of the pop-up feature seen in Figure 3.3a. (c) Graben model based on image shown in Figure 3.3b. The units below the top Paleocene are faulted. P-wave velocity V_P is in ft/s while density ρ is in g/cm3. (d) Snapshot at 0.7sec, green star represents source location and the red inverted tringles represent receiver position, blue arrow represents primaries and yellow arrow represents multiples.

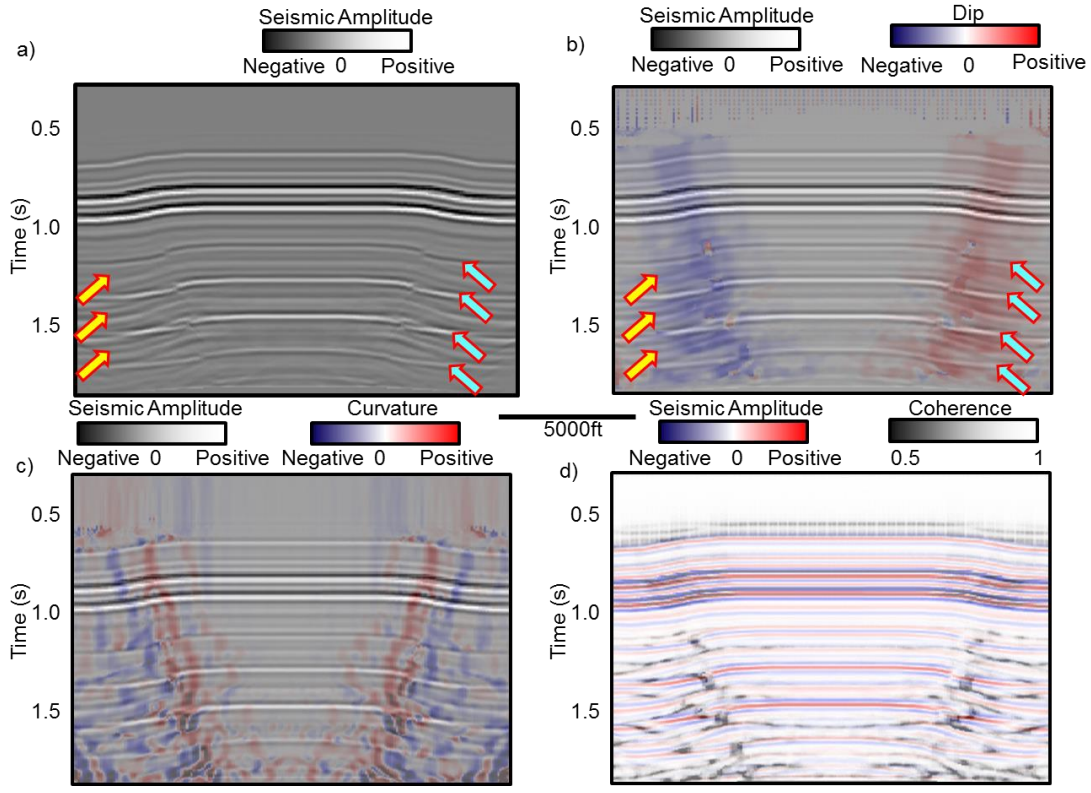

Figure 3.5 (a) Modeled prestack depth migrated (time converted) data from 120 common shot gathers based on model displayed in Figure 3.3a. The same section co-rendered with (b) dip, (c) 2D curvature, and (d) coherence. Primaries are indicated by cyan arrow and multiples are indicated yellow arrow. Note that the multiples from the shallower horizon disrupt the anomalies on dip and curvature. The fault plane reflection appears only above the stronger reflection. These fault plane reflections give rise to a continuous response such that the coherence anomalies are minimal. All the attributes including seismic are displayed with 50% opacity.

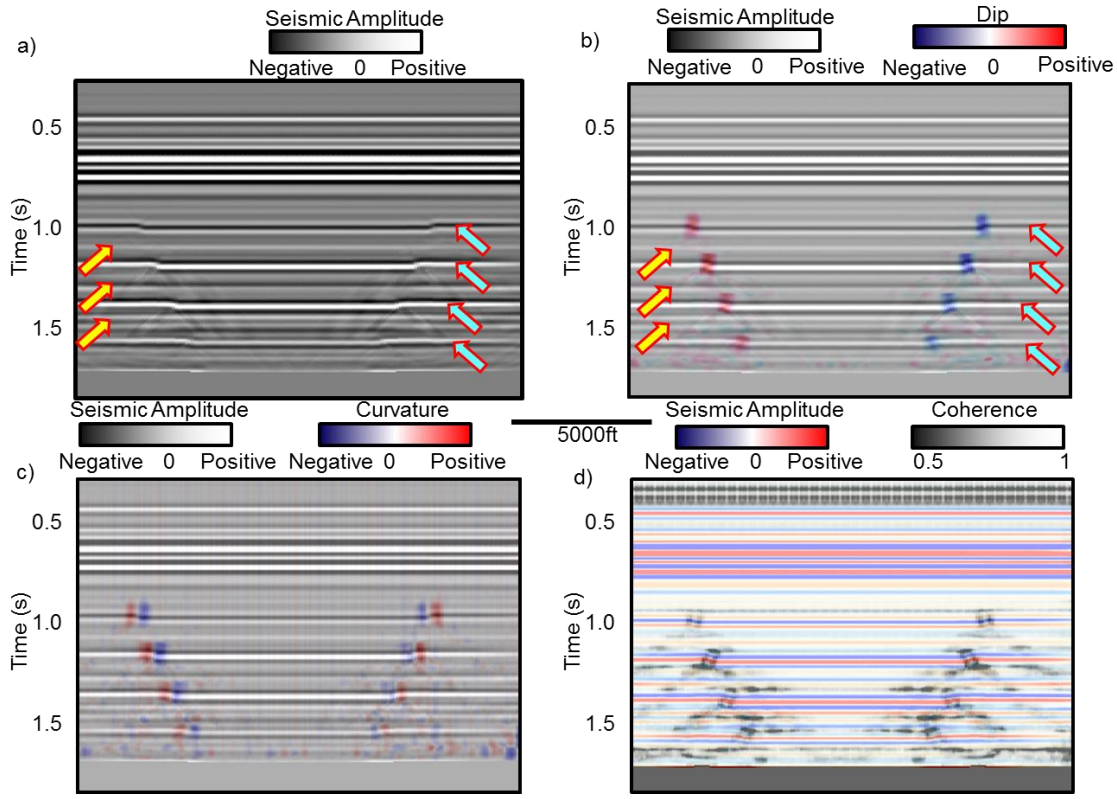

Figure 3.6 (a) Modeled prestack depth migrated (time converted) data from 120 common shot gathers on model displayed in Figure 3.3b (primaries are indicated by cyan arrow and multiples are indicated yellow arrow). The same section co-rendered with (b) dip, (c) 2D curvature, and (d) coherence. Note that the multiples from the shallower horizon disrupt the anomalies on dip and curvature. The fault plane reflection appears only about the stronger reflection. These fault plane reflections give rise to a continuous response such that the coherence anomalies are minimal. All the attributes including seismic are displayed with 50% opacity.

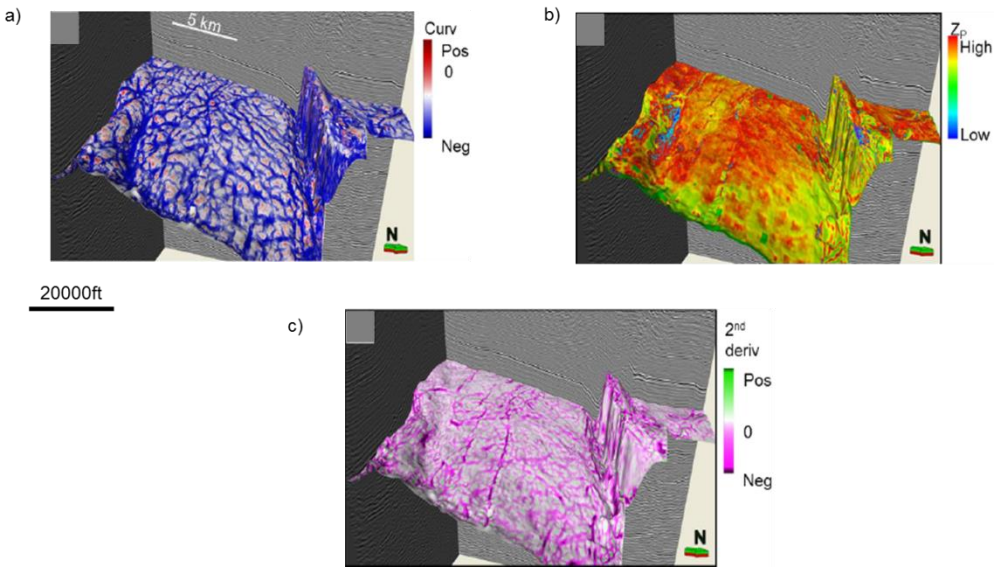

Figure 3.7 Horizon slices along the top Woodford Shale through (a) most negative principal structural curvature, (b) acoustic impedance, and (c) most-negative curvature (a 2nd derivative) of the acoustic impedance volumes. Note the correlation of structural curvature lineaments with subtle faults on the vertical slice through seismic amplitudes. These faults give rise to subtle changes in amplitude and hence to impedance, which are delineated through 2nd derivative (curvature) computations seen in (c). The correlation of the low impedance anomalies and structural lows implies that they are either fault- or fracture-related, though this correlation may be due to limitations in seismic imaging rather than to geology. (Data courtesy of CGG-Veritas. After Guo et al., 2010).

a)

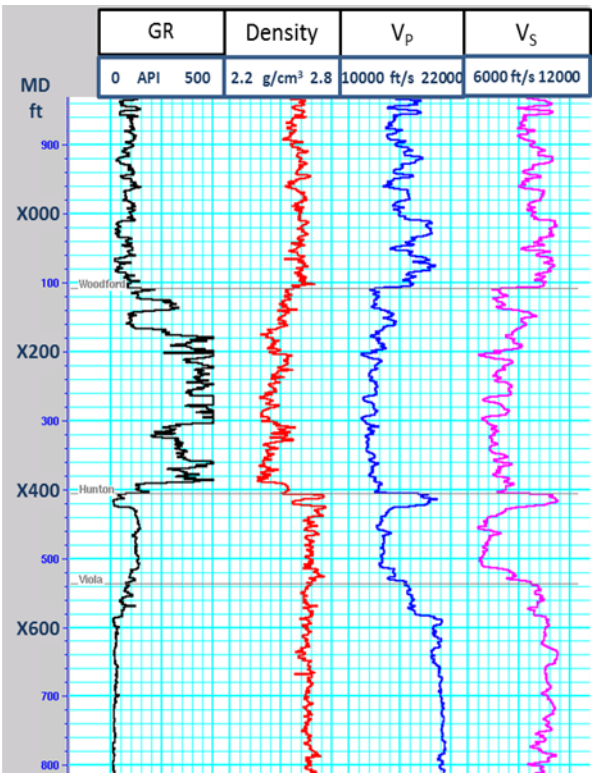
GR
Density
V_P
V_S
0 API 500
2.2 g/cm³ 2.8
10000 ft/s 22000
6000 ft/s 12000
MD
ft
X000
X200
X400
X600
Woodford
Hunton
Viola

b)

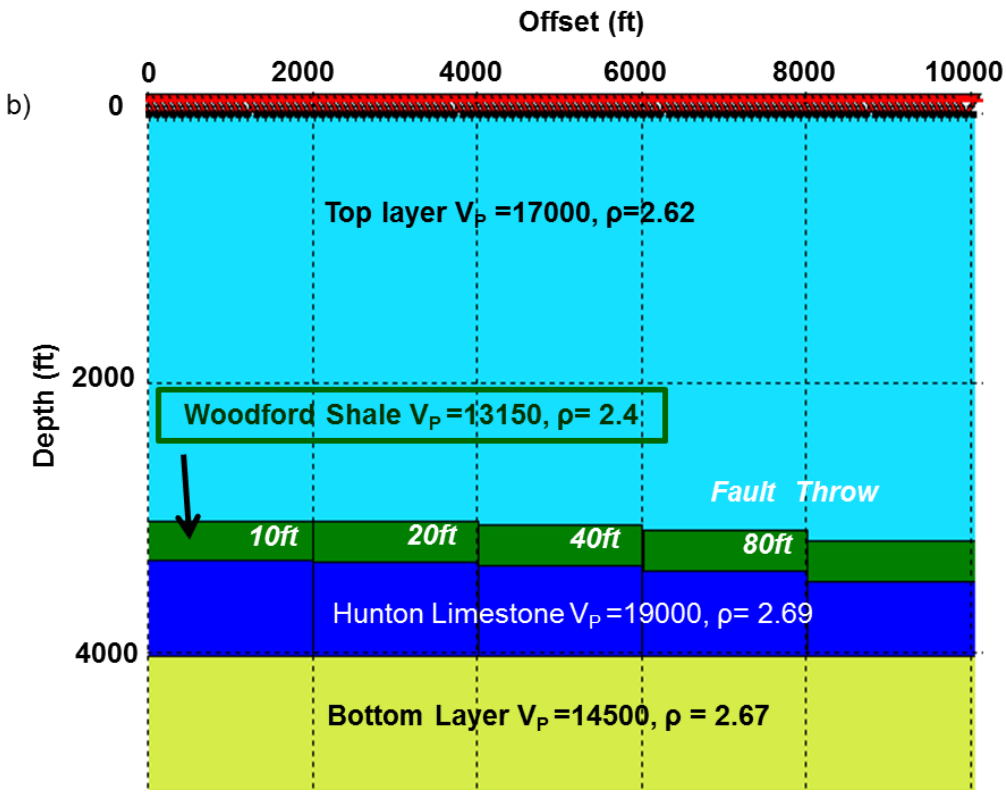
Offset (ft)
0
2000
4000
6000
8000
10000
Depth (ft)
0
2000
4000
Top layer V_P =17000, ρ=2.62
Woodford Shale V_P =13150, ρ= 2.4
Fault Throw
10ft
20ft
40ft
80ft
Hunton Limestone V_P =19000, ρ= 2.69
Bottom Layer V_P =14500, ρ = 2.67

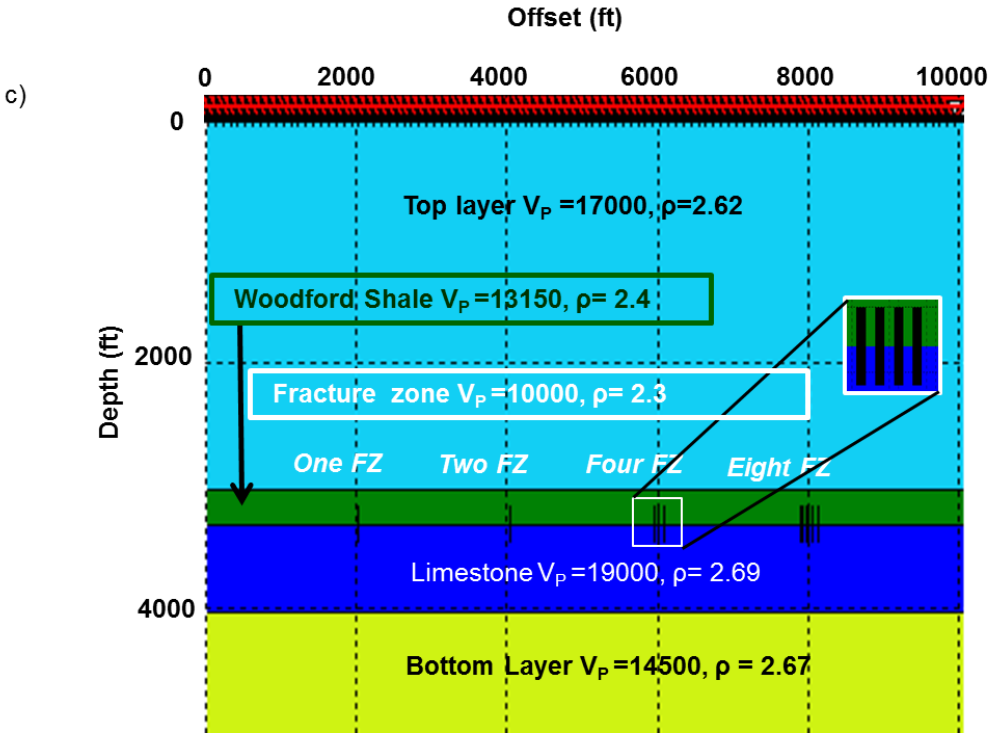

Figure 3.8 (a) A representative well log section of the study area, and (b) model of a suite of faults with variable throw constructed to evaluate the hypothesis that amplitude anomalies are due to errors in prestack migration. The green Woodford Shale layer is faulted with the fault dying out in the deeper blue Hunton Limestone layer. (c) Model to evaluate fractures filled with low impedance material. In this model we represent a variable number of 20 ft wide fracture zones with lower impedance inclusions. Velocities are in ft/s, while densities are in g/cm^3.

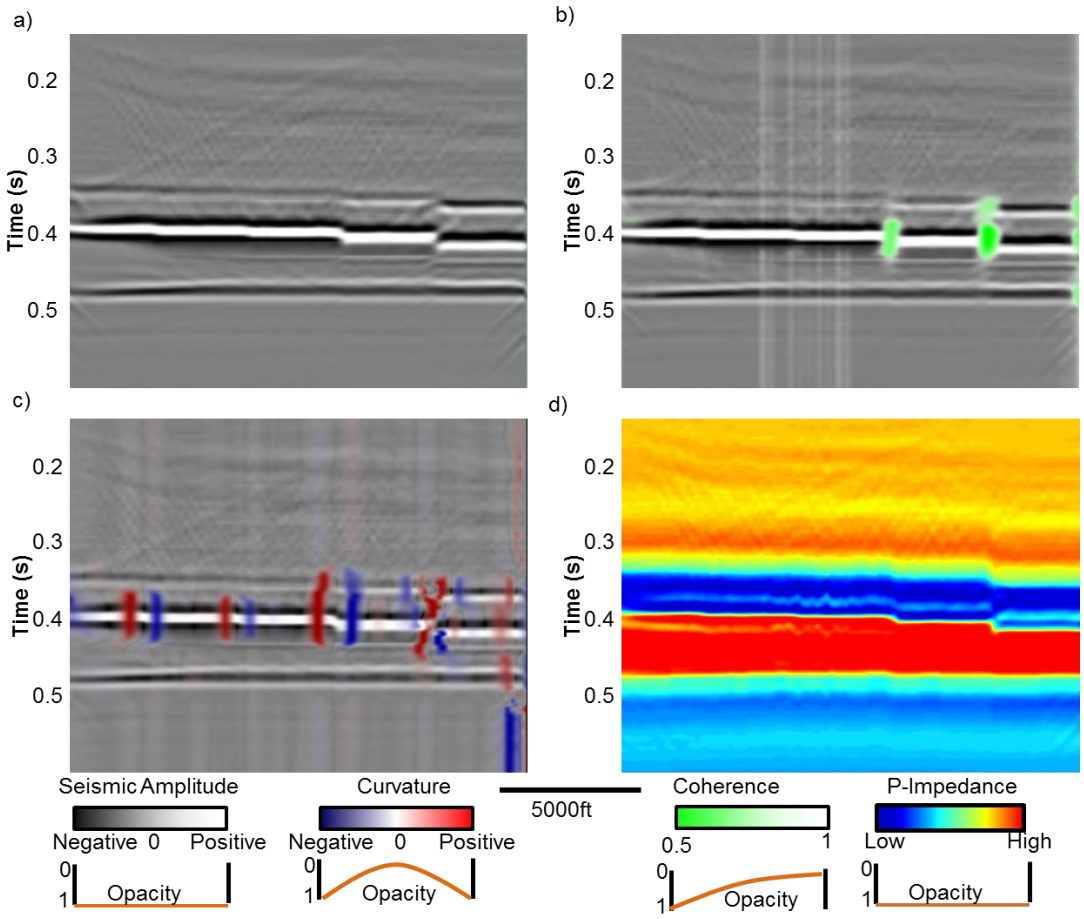

Figure 3.9 (a) Prestack time migrated stacked seismic section generated from 100 common shot gathers over the model shown in Figure 3.8b. Note the amplitudes across these faults are a very continuous, indicating that prestack time migration preserves amplitude across faults with such small throw. The top Woodford at t~0.35 s is clearly visible. The faults with throws of 10 and 20 ft fall below seismic resolution, while faults with throw greater than 40 ft are more easily identified. Stacked seismic amplitude co-rendered with (b) coherence shows the faults with 40 ft and higher throws, (c) Curvature was able to see the all the faults. (d) Acoustic impedance also maps the fault and does not suffer from imaging loss amplitudes.

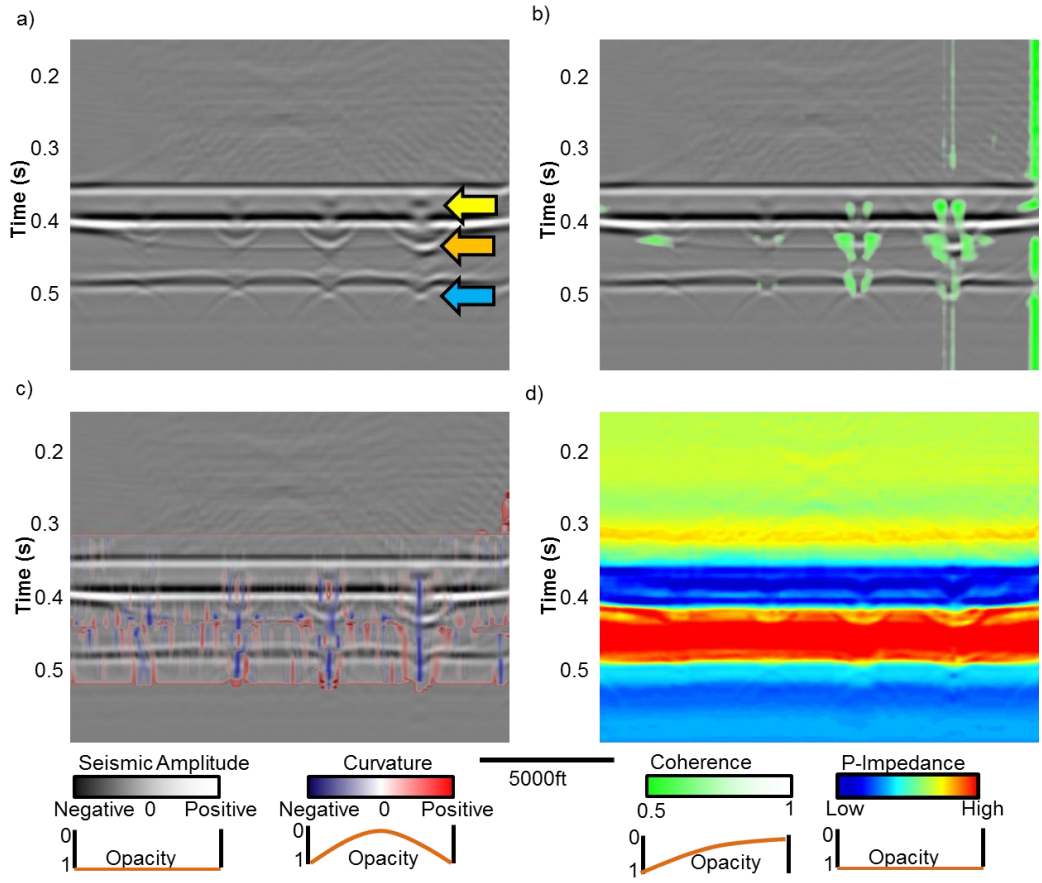

Figure 3.10 (a) Prestack time migrated stacked seismic section generated from 100 common shot gathers over the model shown in Figure 3.8c. The top Woodford at t~0.35 s is clearly visible. As in the real data, the velocity model for prestack migration did not include the perturbation due to the fractures. While the top of the fracture zones are accurately imaged (yellow arrow) the base is overmigrated because the velocity used was too fast (orange arrow). In addition, the base of the limestone layer experiences a velocity pushdown effect (cyan arrow). Stacked seismic amplitude co-rendered with (b) coherence shows the faults with 4 and 8 fracture zones clearly, (c) Curvature was able to delineate fractures. (d) In contrast to the fault model, the fracture zones give rise to a low impedance anomaly, as seen in the real data shown in Figure 3.7b and c.

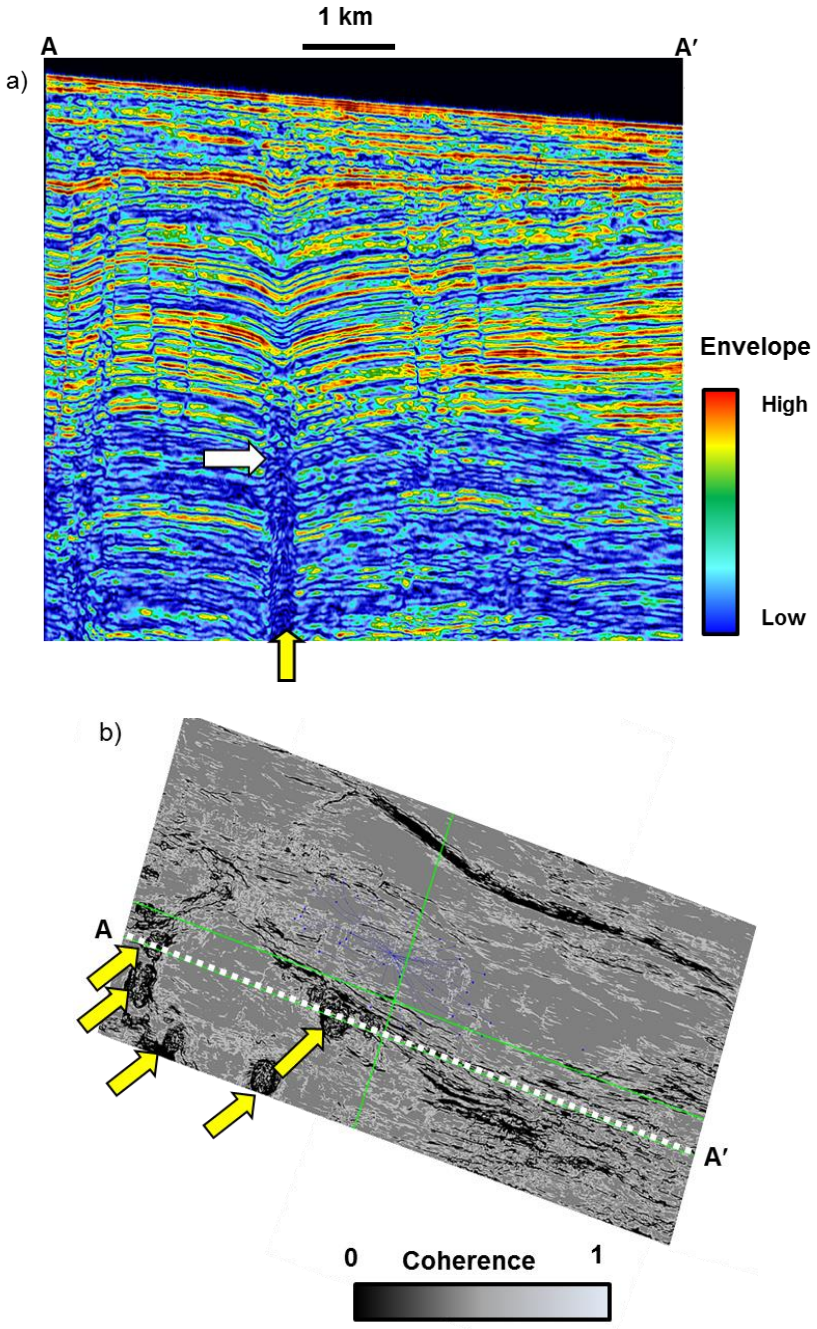

Figure 3.11 (a) A cross section through the envelope of the seismic data (time domain) corresponding to lines AA' from a survey acquired over Liuhua field reservoir, offshore China. The dotted white line indicates the top Miocene carbonate reservoir. (b) Horizon slice along the top reservoir through the coherence volume. Yellow arrows indicate karst collapse chimneys. Note the incoherent image above the karsted reservoir in (a) indicated by the white arrow. Such poor imaging indicates the data were migrated using an incorrect velocity model, consistent with the collapse chimney hypothesis. High amplitude reflections (black arrow) that ring the chimney are consistent with gas charge from below. (After Story et al., 2000).

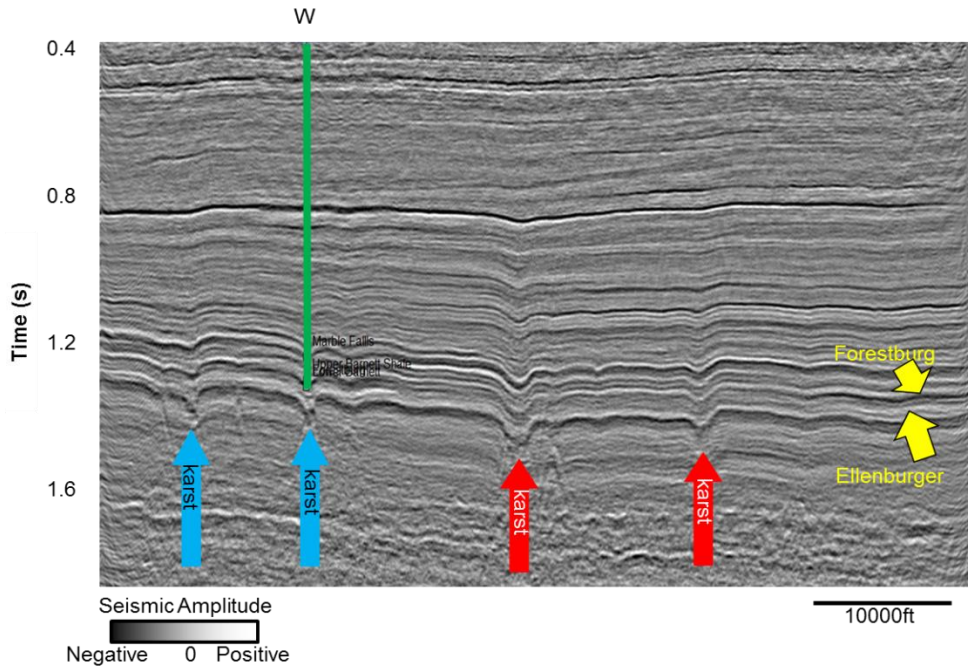

Figure 3.12 Seismic cross section showing four karst depressions. Note the two karsts on the left have smaller diameters and steeply dipping reflection (blue arrows) while the two on the right have larger diameters and less steeply reflectors (red arrows). Model parameters defined from well W. (Data courtesy Devon Energy).

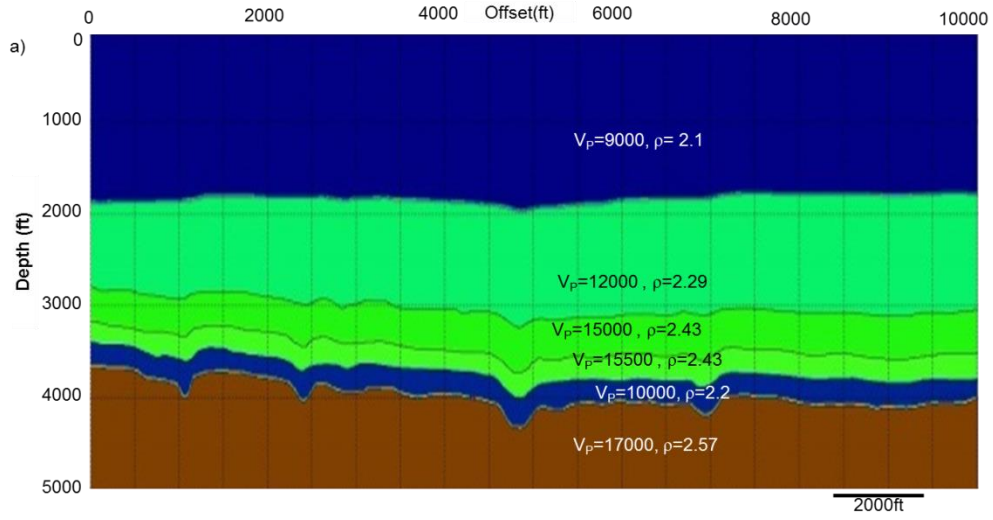

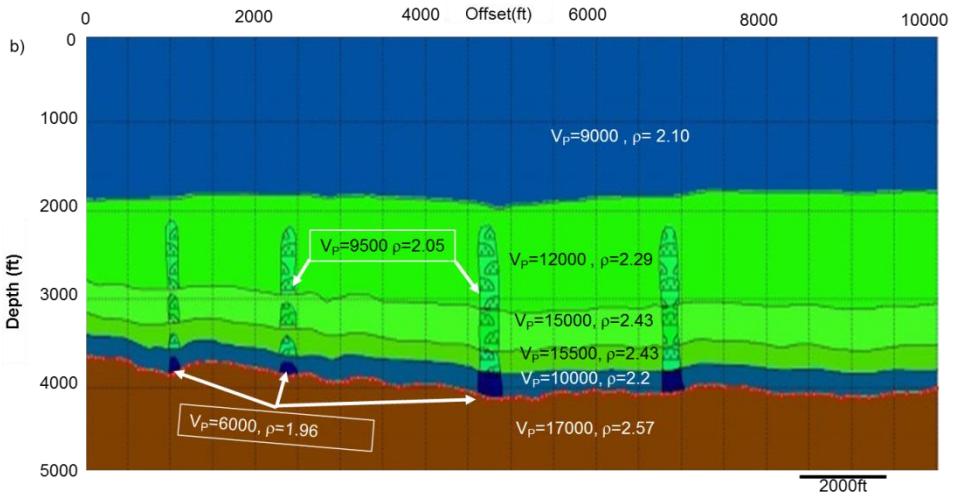

Figure 3.13 (a) An illustration of the karst model used. (b) A low velocity gas chimney model used. Both models are based on Figure 3.12. In both the models V_P is in ft/s while density ρ is in g/cm^3.

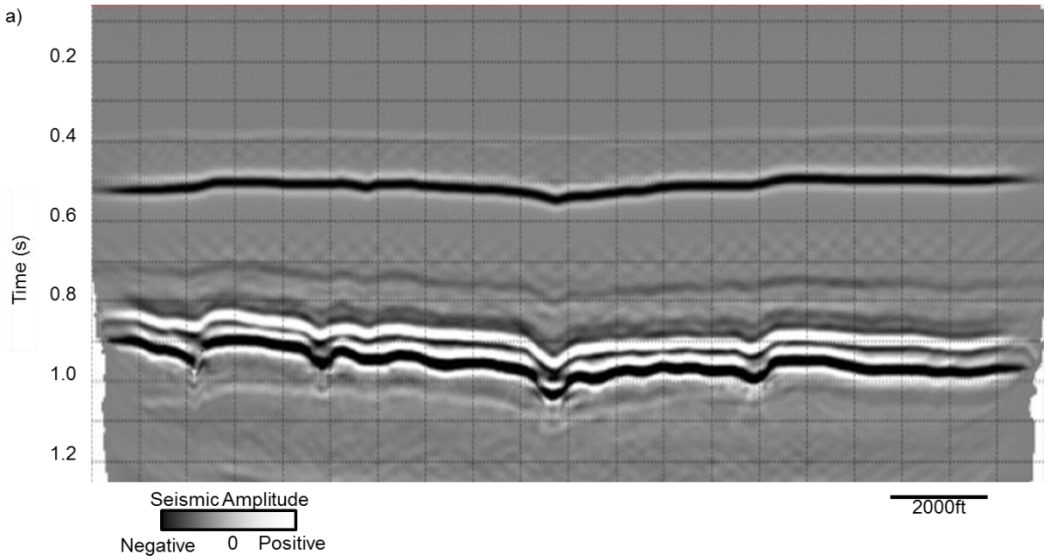

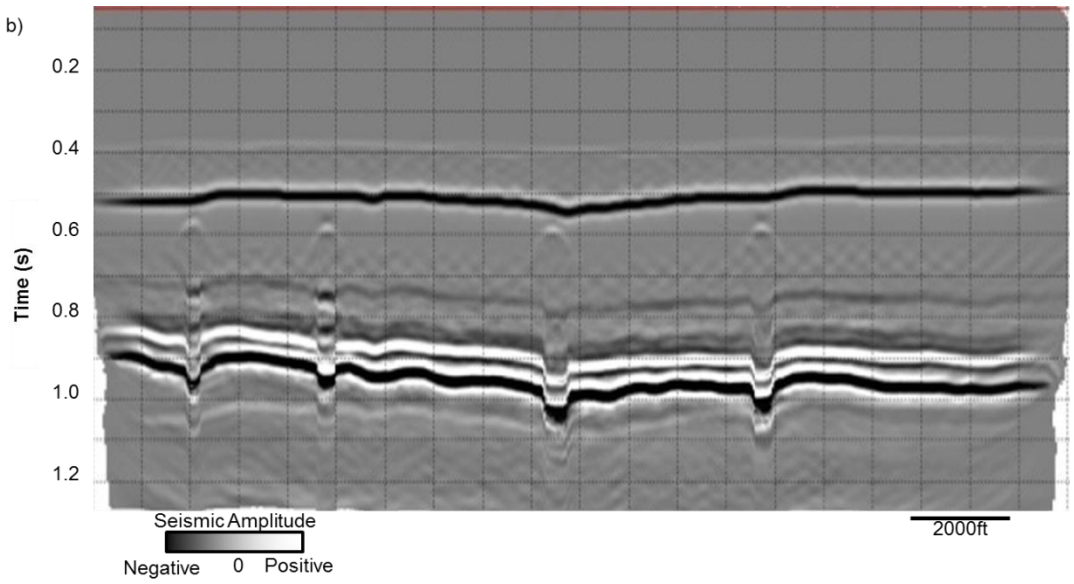

Figure 3.14 Seismic cross section through the depth migrated (converted to time) (a) karst collapse model of Figure 3.13a and (b) the gas chimney model of Figure 3.13b.

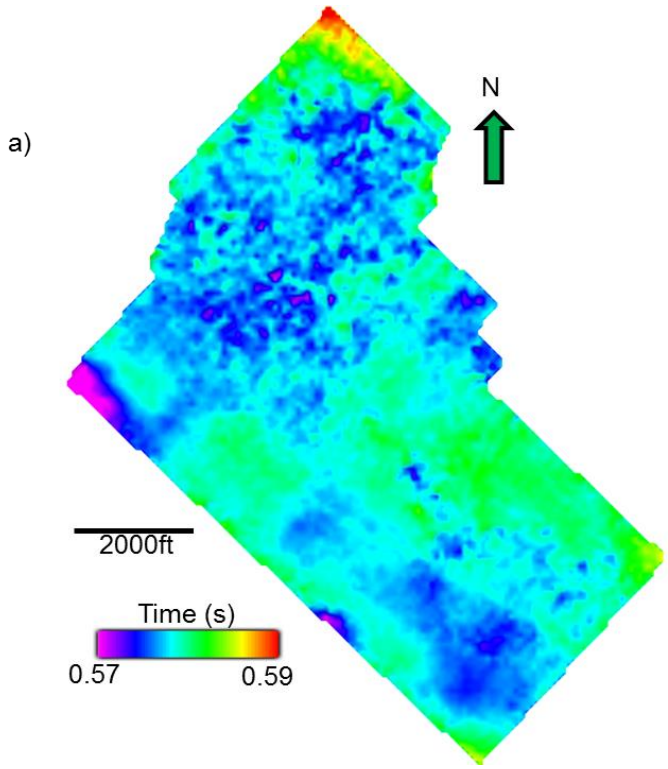

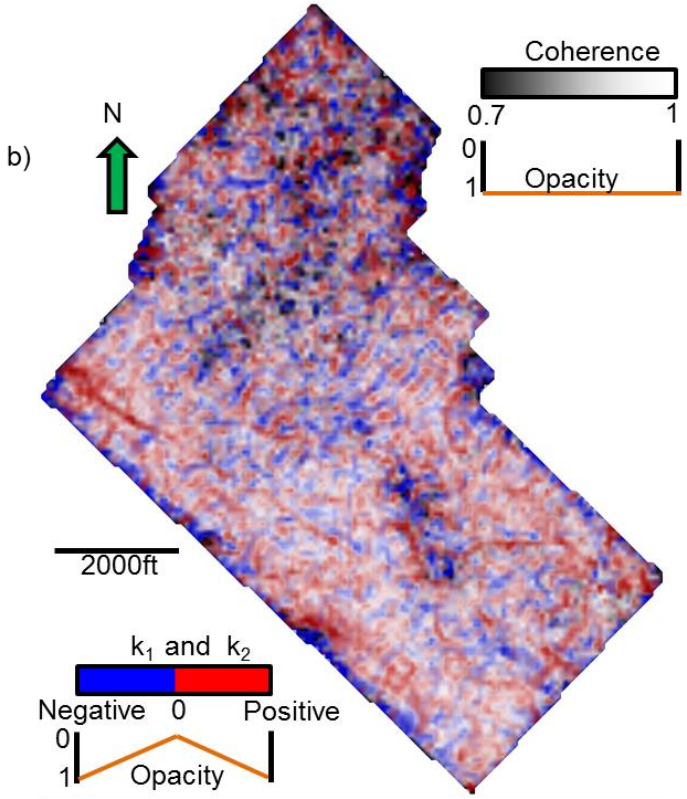

Figure 3.15 (a) Time-structure map of top basement horizon. The northern part of the horizon is noisy and difficult to pick. Since the top basement and the top evaporite are close to each other, the rugose appearance of the northern top basement is not geophysical noise, but rather geology, represent the weathered, eroded, and fractured top basement. Geologic relief of the top basement is as high as 360 ft. (b) Co-rendered image of k_1, k_2, and coherence along the top basement horizon. We suspect that some of the NW-SE lineaments may be acquisition footprint. The k_1 lineament is displaced ~200 ft to the south of the k_2 lineament.

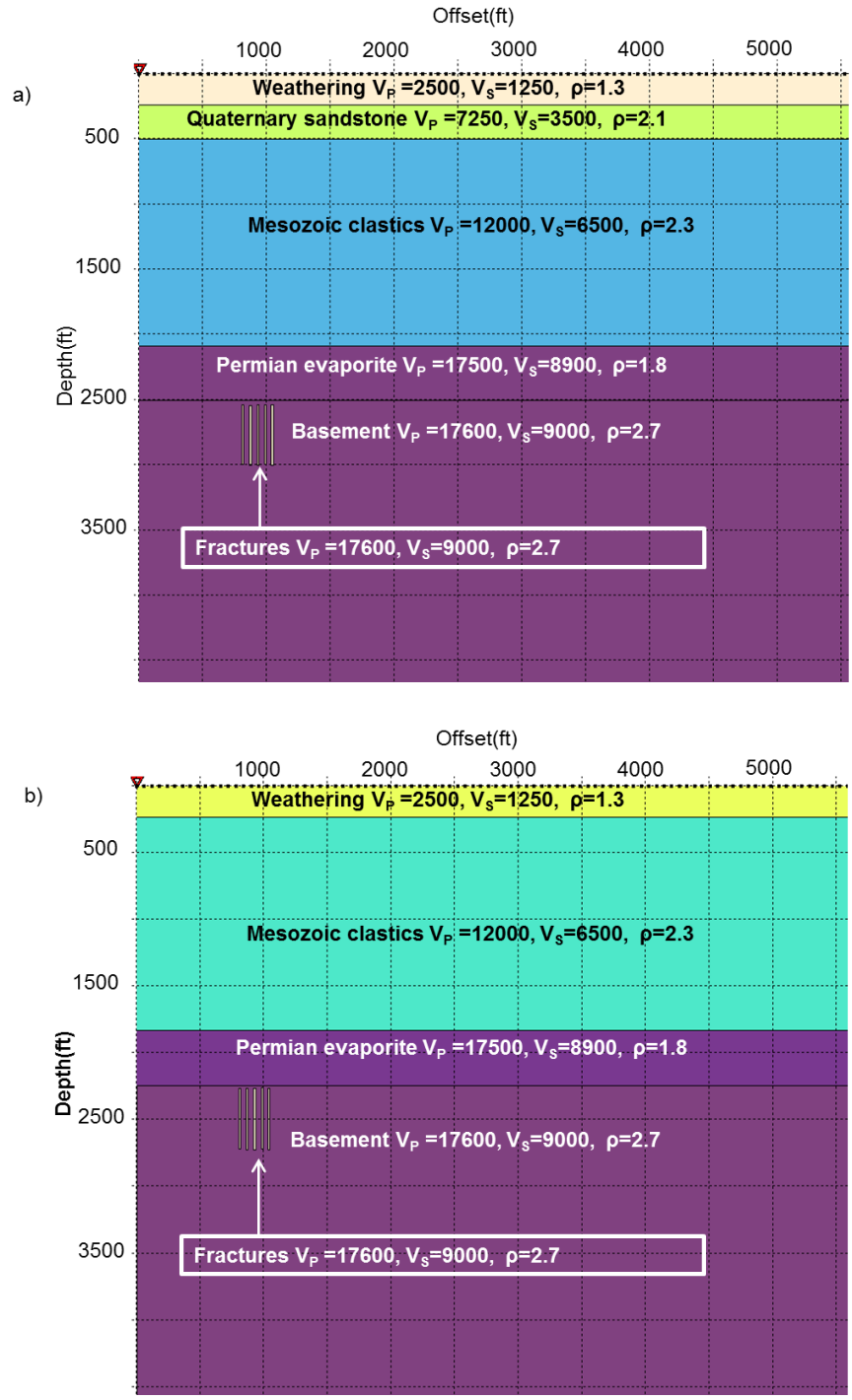

Figure 3.16 Flat-layered Earth model with hypothesized fractures in the basement (a) with, and (b) without a weathering zone. Velocity and density generally increased with depth, except for the low-density evaporate. The fractures are 20-ft thick and have lower velocity and density than the basement. This model in (b) is designed to avoid the reverberation effect of seismic wave in the weathering zone.

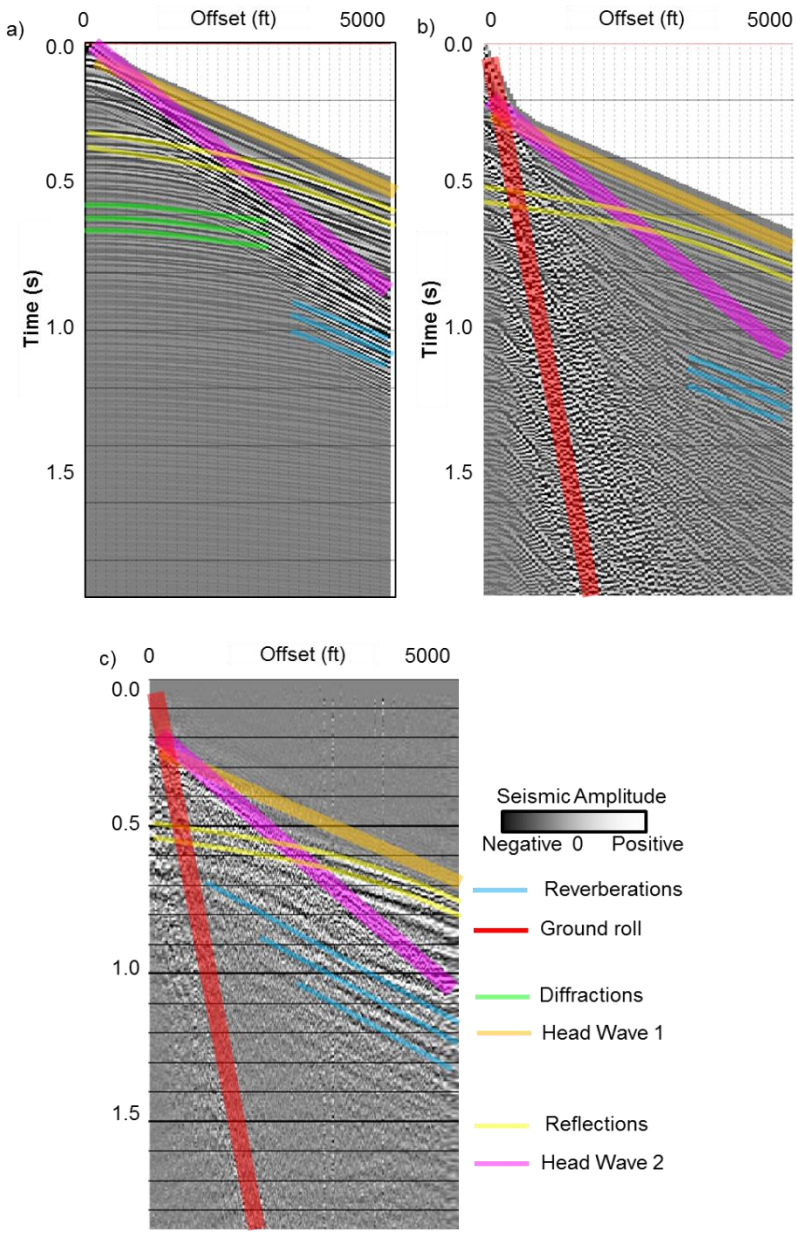

Figure 3.17 (a) Acoustic-modeled gather on model shown in Figure 3.16b with interpreted events. Head wave, reflections, diffractions, and reverberation are identified on the gather by alternatively examining the snapshots of the wave field. (b) Elastic-modeled gather on model shown in Figure 3.16a with interpreted events. Head wave, reflections, ground roll, and reverberation are identified. Note that diffractions are not identified because it was overlaid by strong reverberation from the weathering zone. (c) Real shot gather with interpreted events. Head wave, reflections, ground roll, and reverberation are identified. Note that the reverberation effect of the weathering zone is much less in the real gather than the modeled gather due to finite Q (1/attenuation). At the target depth (t=0.57s), critical refraction occurs at offset h = 3200 ft. Beyond this point, the signal are highly contaminated by coherent, moderate bandwidth refracted waves and must be muted after NMO correction.

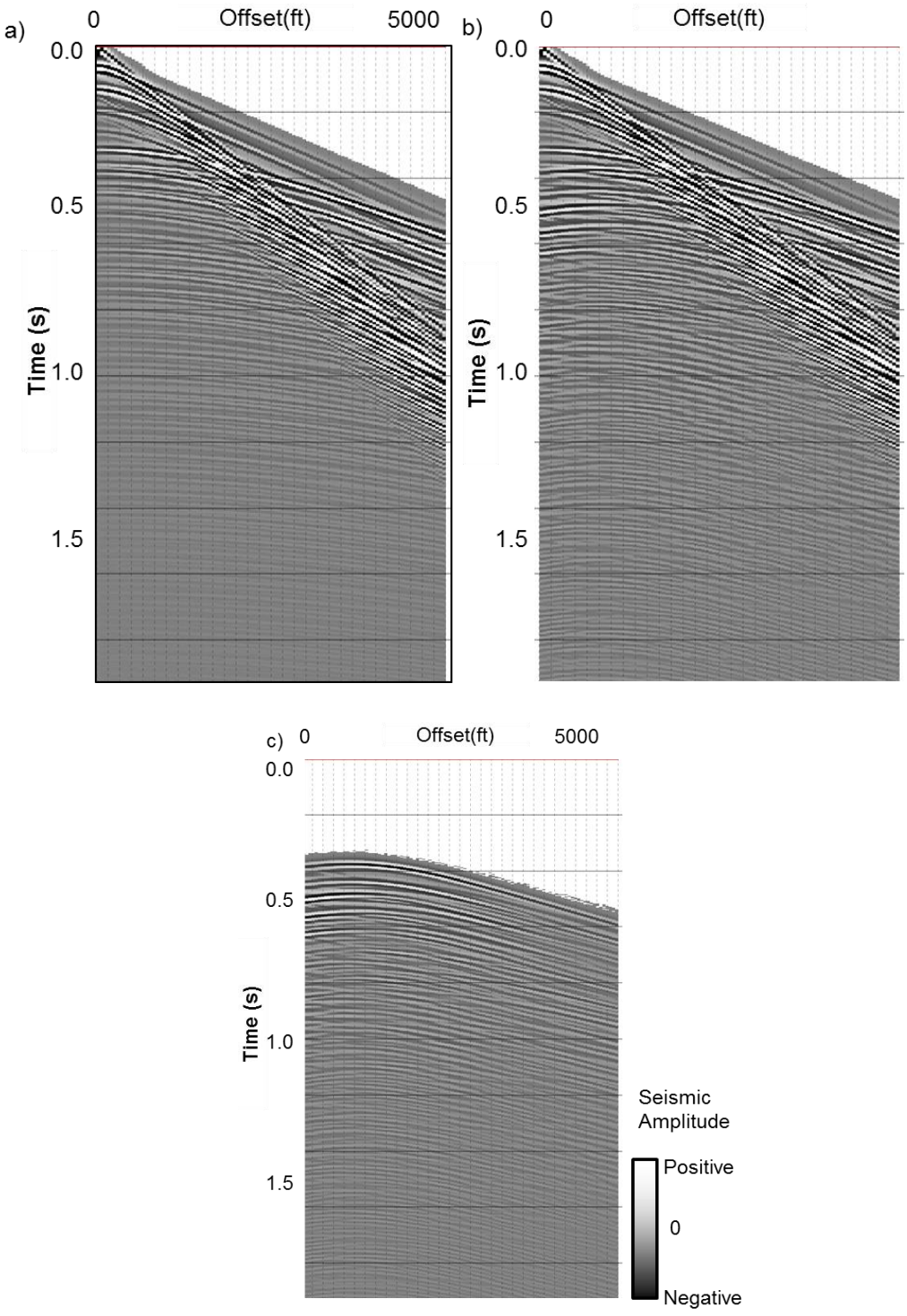

Figure 3.18 Acoustic-modeled shot gather sorted by absolute offset corresponding to the model with no weathering zone Figure 3.16b and (a) with and (b) without fractures. (c) Difference between (a) and (b), showing diffractions. Note that diffractions are not centered at zero offset.

REFERENCES

Alai, R., J. Thorbecke, and E. Verschuur, 2011, Analysis of elastic wave field propagation through gas clouds: 81st Annual International Meeting, SEG, Expanded Abstracts, 3002-3006.

Al-Dossary, S., and K. J. Marfurt, 2006, 3-D volumetric multispectral estimates of reflector curvature and rotation: Geophysics, **71**, P41–P51.

Baruch, E., O. Elebiju, and R. Perez, 2009, Geophysical evidence of basement controlled faulting in the Ellenburger Group and Viola Limestone, Fort Worth Basin, Texas: 79th Annual International Meeting, SEG, Expanded Abstracts, 995-999.

Chopra, S. and K. J. Marfurt, 2013, Structural curvature versus amplitude curvature: The Leading Edge, **32**, 178-184.

Chopra, S., and K. J. Marfurt, 2007, Seismic attributes for prospect identification and reservoir characterization: Society of Exploration Geophysicists, Tulsa, OK.

Clawson, S., H. Meng, M. Sonnenfeld, M. Uland, S. Atan, M. Batzle, M. Gardner, and M. S. Uman, 2003, The value of 3D seismic attributes for illuminating deep water deposits by seismic forward modeling of the Brushy Canyon formation: 73rd Annual International Meeting, SEG, Expanded Abstracts, 2431-2434.

Cordsen, A., M. Galbraith, and J. Peirce, 2000, Planning land 3-D seismic surveys: Geophysical Development Series, SEG.

Fagin, S. W., 1991, Seismic modeling of geologic structures: Applications to exploration problems: Geophysical Development Series, Society of Exploration Geophysicists.

Fernandez, A., 2013, 3D Seismic Attribute expression of the Ellenburger group Karst-Collapse features and their effects on the production of the Barnett Shale, Fort Worth Basin, Texas: M.S. Thesis, the University of Oklahoma.

Fehler, M., 2012, SEAM Update, TLE, **31**, 1424-1426.

Guo, Y., K. Zhang, and K. J. Marfurt, 2010, Seismic Attribute Illumination of Woodford Shale Faults and Fractures, Arkoma Basin, OK: 80th Annual International Meeting of the SEG, Expanded Abstracts, 1372-1376.

Gupta, N., S. Sarkar, and K. J. Marfurt, 2013, Seismic attribute driven integrated characterization of the Woodford Shale in west-central Oklahoma: Interpretation, **1**, no. 2, SB85-SB96.

Hart, B., and M. Chen, 2004, Understanding seismic attributes through forward modeling: The Leading Edge, **23**, no. 9, 834-841.

Marfurt, K. J., 2006, Robust estimates of 3D reflector dip and azimuth: Geophysics, 71, P29–P40.

McQuillan, H., 1974, Fracture patterns on Kuh-e Asmari anticline, southwest Iran: AAPG Bulletin, **58**, 236–246.

Mukherjee, T., K. Mehta, J. Lopez, and R. R. Stewart, 2012, Modeling in a time-lapse study of an EOR target in Oman: 82nd Annual International Meeting of the SEG, Expanded Abstracts, 1-5.

Murray, Jr., G. H., 1968, Quantitative fracture study-Spanish Pool, McKenzie County, North Dakota: AAPG Bulletin, **52**, 57–65.

Sarkar, S., 2011, Depositional history and reservoir characteristics of structurally confined foredeep turbidites, northern Chicontepec Basin, Mexico: PhD Dissertation, The University of Oklahoma.

Nissen, S. E., T. R. Carr, K. J. Marfurt, and E. C. Sullivan, 2009, Using 3D seismic volumetric curvature attributes to identify fracture trends in a depleted Mississippian carbonate reservoir: Implications for assessing candidates for CO_2 sequestration: AAPG Studies in Geology, **59**, 297–319.

Pena V., S. Chávez-Pérez, M. Vázquez-García, and K. J. Marfurt, 2009, Impact of shallow volcanics on seismic data quality in Chicontepec Basin, Mexico: The Leading Edge, **28**, 674-679.

Pena-Marino, V., 2010, Integrated geophysical investigation of shallow igneous bodies and the impact on seismic data quality, Chicontepec Basin, Mexico: M.S. Thesis, The University of Oklahoma.

Qi, J., B. Zhang, H. Zhou, and K. J. Marfurt, 2014, Attribute expression of fault-controlled karst — Fort Worth Basin, Texas: A tutorial : Interpretation, **2**, No. 3, SF91-SF110.

Russell, B. H., L. R. Lines, K. W. Hirsche, J. Peron, and D. P. Hampson, 2001,The AVO modelling volume : Exploration Geophysics, **32,** No. 3/4, 264-270.

Staples, E., K. J. Marfurt, and Z. Reches, 2011, Curvature-fracture relations in clay experiments: 81st Annual International Meeting, SEG, Expanded Abstracts, 1908-1912.

Story, C., P. Peng, C. Heubeck, C. Sullivan, and J. Lin, 2000, Liuhua 11-1 Field, South China Sea: A shallow carbonate reservoir developed using ultrahigh-resolution 3-D seismic, inversion, and attribute-based reservoir modeling: The Leading Edge, **19**, 834–844.

Versteeg, R., 1994, The Marmousi experience: Velocity model determination on a synthetic complex data set: TLE, **13**, 927-936.

Xu, X., 2014, Integrated geophysical studies of the Northeastern Caribbean Plate, Eastern Tibetan plateau in China and Panhandle field (Texas): Ph.D. dissertation, the University of Oklahoma.

Zhao, W., S. Anjiang, Z. Qiao, J. Zheng, and X. Wang, 2014, Carbonate karst reservoirs of the Tarim Basin, northwest China: Types, features, origins, and implications for hydrocarbon exploration: Interpretation, **2**, SF65-SF90.

CHAPTER 4 **: PITFALLS IN SEISMIC PROCESSING**

PITFALLS IN SEISMIC PROCESSING: PART 1 GROUNDROLL SOURCED ACQUISITION FOOTPRINT

Sumit Verma, Marcus P. Cahoj, Tengfei Lin, Fangyu Li, Bryce Hutchinson and Kurt J. Marfurt*

The University of Oklahoma, ConocoPhillips School of Geology and Geophysics.

This paper is accepted as Expanded abstract for SEG annual meeting 2015.

SUMMARY

Whether it is in reference to the limitations of interpretation or associated with seismic processing, usage of the phrase acquisition footprint is never in a positive context. Footprint contaminates both time structure map and impedance inversion. Although common, footprint is often poorly understood. Footprint is more common in older, lower fold surveys. Part of this mystery is due to the division of labor in most exploratory companies. Processing is usually conducted by specialists in a service company, while attribute analysis is conducted by interpreters (often geologists) in an oil company. Often, younger interpreters have never processed 3D seismic data, while younger processors have never analyzed attributes. As a part of a reprocessing effort for quantitative interpretation analysis, Cahoj (2015) encountered severe footprint masking his shallow exploration target. We attempt to modify his processing workflow to ameliorate the footprint lead to an effort to understand its cause, at least for this survey. Upon completion of seismic processing we are left with a stacked version of our synthetic data in which we can compute seismic attributes. We show that the subsequent attribute interpretation is greatly affected by footprint caused by residual groundroll. Lastly, we show an attribute

interpretation corresponding to real 3D seismic dataset and conclude that many artifacts seen in the dataset, often labeled under the broad category of acquisition footprint, are actually residual groundroll not properly removed during the processing flow. Because out of plane groundroll can have hyperbolic moveout common noise removal techniques, such as F-K filtering, that operate under the assumption of modeling noise with different linear moveouts, fail.

INTRODUCTION

Acquisition footprint refers to the imprint of acquisition geometry seen on seismic amplitude timeslices and horizons. Acquisition footprint can obstruct not only classical seismic interpretation but also affect interpretation based on seismic attributes (Marfurt and Alves 2015, Marfurt et al., 1998). Seismic attributes, especially coherence and curvature, often exacerbate the effect of footprint making their utility diminish (Marfurt and Alves 2015; Verma et al., 2014).

With footprint being such a common problem its occurrence and formation are often poorly understood (Chopra and Larsen, 2000). Although many methodologies have been developed to remove linear coherent noise and acquisition footprint (Cvetkovic et al., 2008 and Marfurt et al., 1998), little has been done in the way of illustrating its occurrence via modeling. Hill et al. (1999) investigated acquisition footprint is caused by inaccurately picked NMO velocity. Although groundroll is one of the prime causes of acquisition footprint, the footprint pattern caused by the presence of groundroll has not been modeled and documented.

One of the main causes of seismic acquisition footprint is sparse spatial sampling. It is particularly challenging to remove aliased groundroll. Because of this the residual groundroll's occurrence on the stacked seismic data can be strong enough to influence the interpretation. We study a low fold legacy seismic survey of North Central Texas and observed acquisition footprint with the North-South lineaments (Figure 4.1a) aligned with the receiver lines. We investigate what can cause such footprint to be present in our dataset; in this paper we present the findings.

MOTIVATION

We observed north–south acquisition footprint present on the curvature attribute shown in Figure 4.1a. The presence of this acquisition footprint hindered our attribute assisted interpretation. Because of this we had an incentive to understand its origin. We hypothesis that this acquisition footprint could have three potential sources:

1) Inadequate removal of groundroll,
2) NMO far offset stretch, and
3) Improper velocity analysis

In this paper we decide to investigate the effect of inadequately removed groundroll. In Part 2 (Cahoj et al., 2015) of this abstract we will try to understand the effect of NMO stretching and incorrect velocity analysis on our seismic interpretation. Equipped with an actual seismic dataset with acquisition footprint, we are able to construct a synthetic analogue.

METHODOLOGY

Seismic modeling

The objective of this model is to see the effect of residual groundroll on stacked seismic data after processing and its relation with reflectors.

To do so we created a simple 3D flat layer seismic model with four layers. The acquisition geometry is shown in Figure 4.2, with 6 receiver lines and 9 shot lines. Each receiver line contains 60 receiver groups totaling 360 geophones, and each shot line contains 18 sources totaling 162 shots. The model has a strong presence of broad bandwidth (0-50Hz) dispersive groundroll. We generated two separate models, one for groundroll using an elastic modeling approach with only the weathering layers and a second model with four layers using an acoustic modeling approach. We added these two models to simulate the final 3D acquisition geometry for our study.

Seismic processing

The seismic processing can be broken into 7 steps.

1) Importing the synthetic seismic data
2) Defining the geometry
3) Sorting the data by absolute offset
4) Identifying the noise corridor with a mute and finding its respective linear moveout velocity
5) Model the noise in the F-K domain
6) Inverse linear moveout and subtraction
7) NMO correction and stacking the synthetic data

Figure 4.3a shows a common shot the synthetic sorted by absolute offset. It is easy to identify the lower velocity groundroll crosscutting and overbearing the reflectors. Figure 4.3b shows the groundroll modeled by a standard F-K noise filtering procedure and Figure 4.3c shows the results after the modeled groundroll is subtracted from the input model. In this figure we see that most of the high amplitude groundroll has been removed and the reflectors, once overprinted, are now visible. Upon completion of groundroll removal the synthetic data were NMO corrected and stacked (Figure 4.4a).

Attribute interpretation

We computed a suite of seismic attributes using a commercial software package on both the modeled synthetic seismic data and the actual seismic data. Such attributes included dip and azimuth, energy ratio similarity and curvature. With these attributes we were able to determine footprint's response from improperly removed groundroll. Using the modeled seismic data we were able to make an analogue to actual seismic data to compare groundroll's response and effect on interpretation.

RESULTS

Figure 4.4a shows the inline of the stacked synthetic seismic data. The undulations in the shallow section are the responses of constructively and destructively interfering groundroll not properly removed by F-K filtering. Figure 4b shows the corresponding inline through the actual seismic data. It is evident that similar undulations exist in the shallow section of the real seismic data.

Figure 4.5a is a timeslice at t=1.320s through the most negative curvature response of the stacked synthetic seismic data. We find that the response of curvature, an attribute commonly used to map folds, flexures and deformation about faults, is greatly contaminated by the inadequately removed groundroll. Figure 4.1a shows the corresponding timeslice at t=0.410s through the most negative curvature of the real seismic data; containing a similar footprint expression.

Figure 4.6a shows a horizon tracked through the 2nd layer in the synthetic dataset. Because the layers were modeled to be horizontal we expect a uniform surface at a constant depth. However, we can see rectilinear features, particularly strong in the East-West direction. These features can also be seen in Figure 4.6b, the real seismic data.

CONCLUSIONS

Our analysis indicates that the undulations caused by residual groundroll will be present on the seismic, having strongest amplitude near the surface and attenuating with depth.

We conclude that inadequately removing groundroll can result in erroneous and more difficult interpretations. Furthermore, seismic attributes, often used by less experienced interpreters to accelerate there interpretations, are not immune to acquisition footprint caused by groundroll. In many cases, seismic attributes exacerbate the effects of this noise.

ACKNOWLEDGMENTS

We would like to thank the sponsors of the AASPI consortium, Schlumberger for the use of Petrel and VISTA and TESSERAL Technologies Inc. for the licenses to their software.

FIGURES

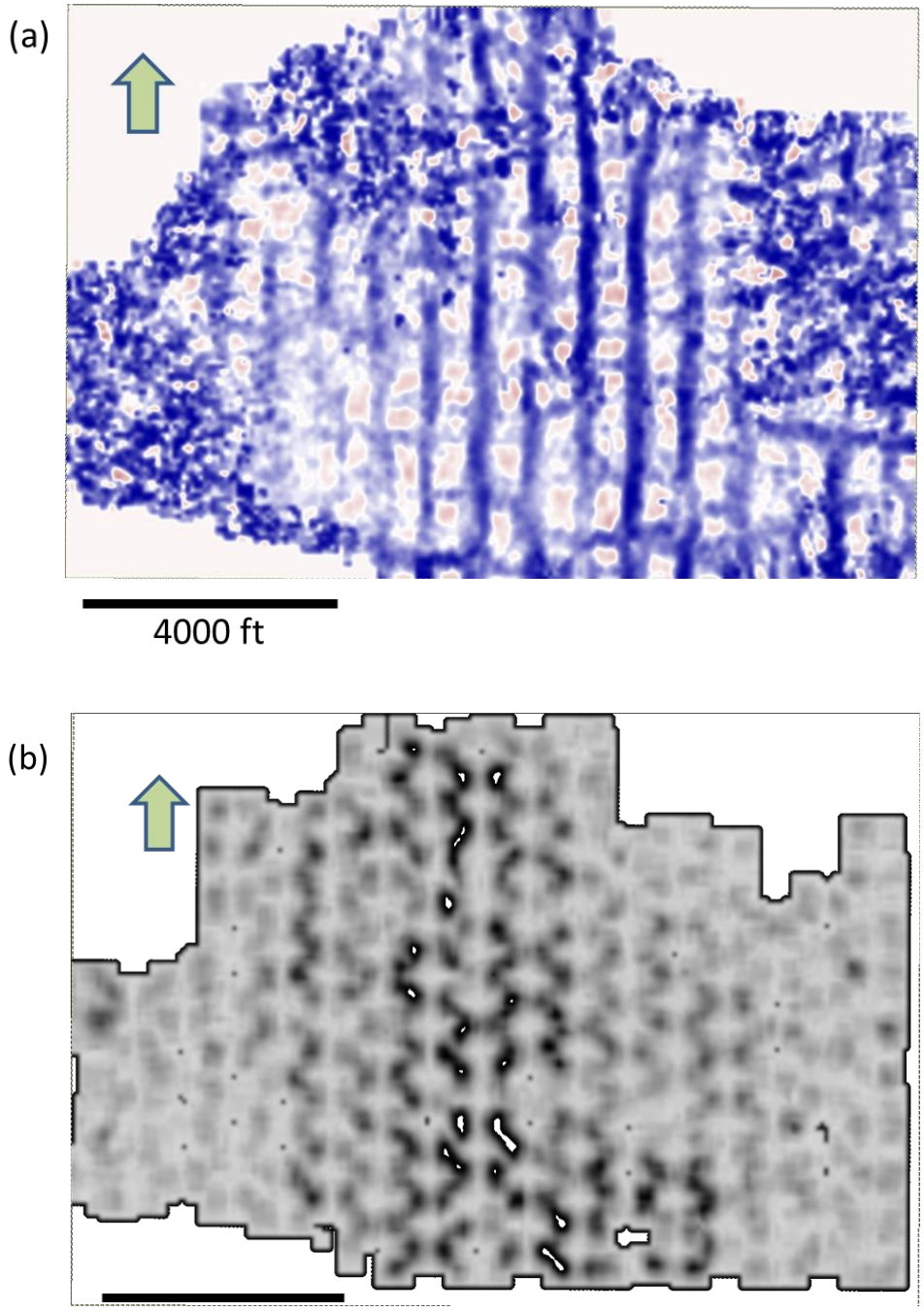

Figure 4.1 (a) Timeslice at t=0.41s through most negative curvature volume from real seismic dataset. The North-South lineaments are aligned with the receiver lines. These artifacts contaminate attribute volumes. (b)Timeslice at t=0.41s through coherence volume from real seismic dataset. The North-South lineaments are aligned with the receiver lines. These artifacts are weaker at depth but overprint the objective at t=1.0s.

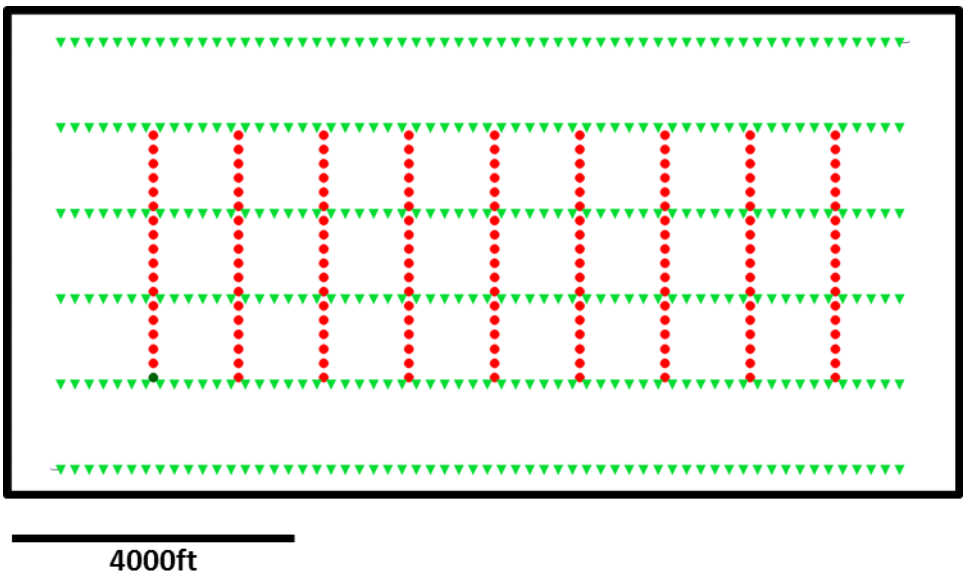

Figure 4.2 The synthetic model's geometry. Sources are in red and receivers are in green. The geometry is perfectly rectilinear which is not the case with actual seismic data due to surface obstructions.

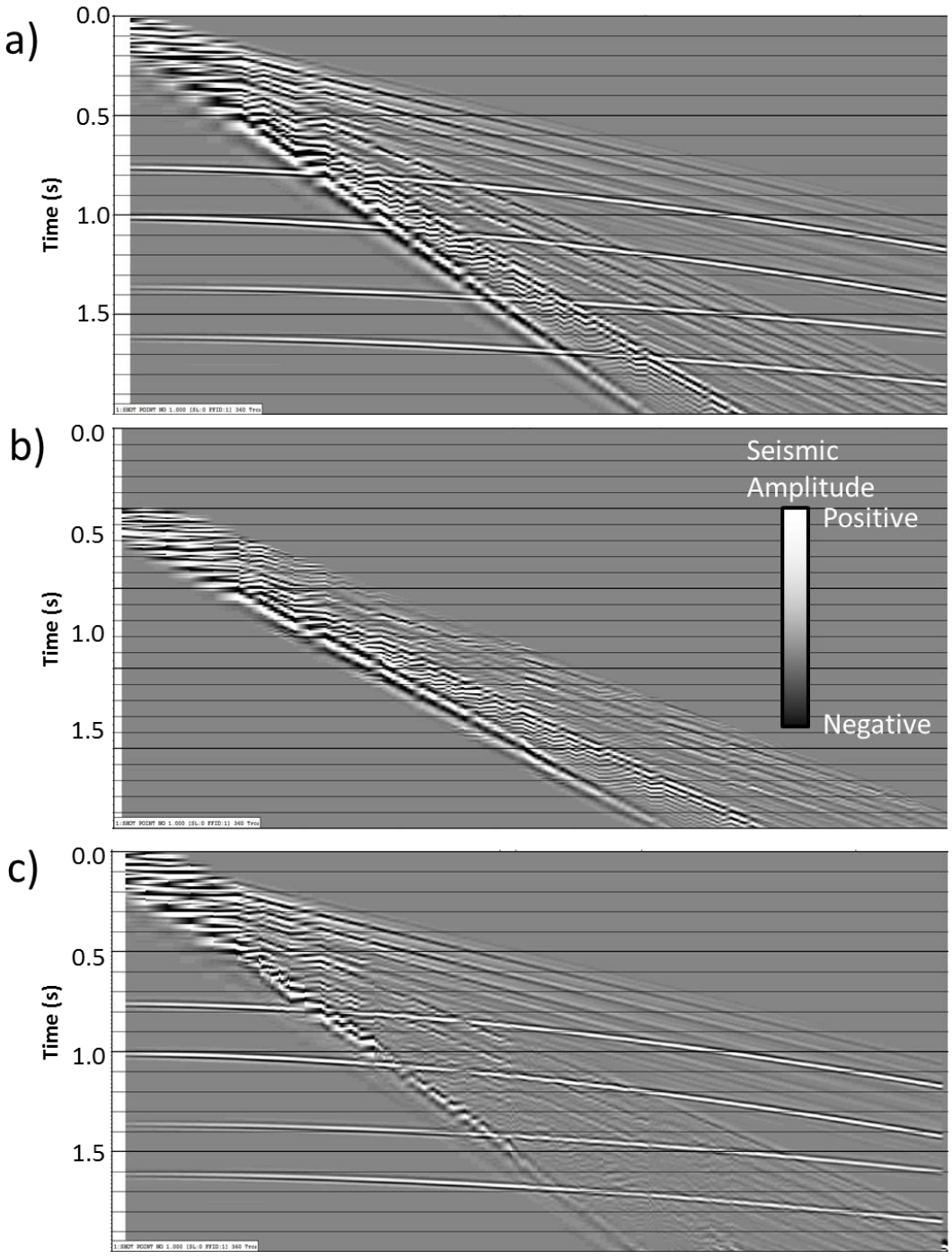

Figure 4.3 Shot vs absolute offset sorted (a) modeled seismic data with four reflectors and groundroll with a large bandwidth (0-50Hz). b) F-K modeled groundroll to be removed from the modeled seismic data (a). (c) Result of subtracting F-K modeled groundroll (b) from modeled seismic (a). Notice large amounts and high amplitude groundroll is removed, but residual remains.

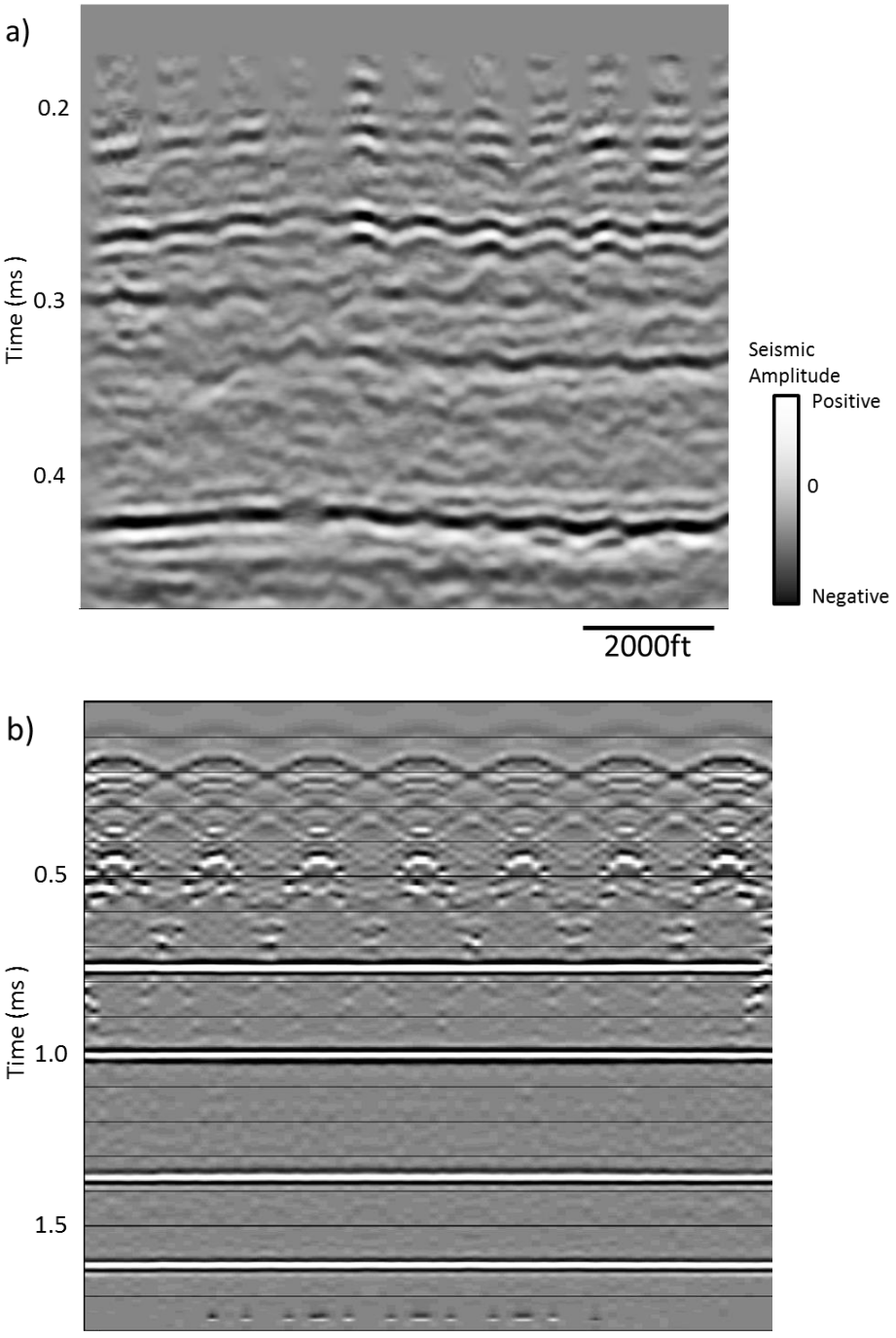

Figure 4.4 (a) Inline through the synthetic seismic data. (green horizon is displayed in Figure 6a) (b) Inline of real seismic data (yellow horizon is displayed in Figure 4.6b) . Notice the undulation anomalies caused by inadequately removed groundroll in Figure 4.6a and similar undulation features can be seen in Figure 4.6b most likely caused by groundroll.

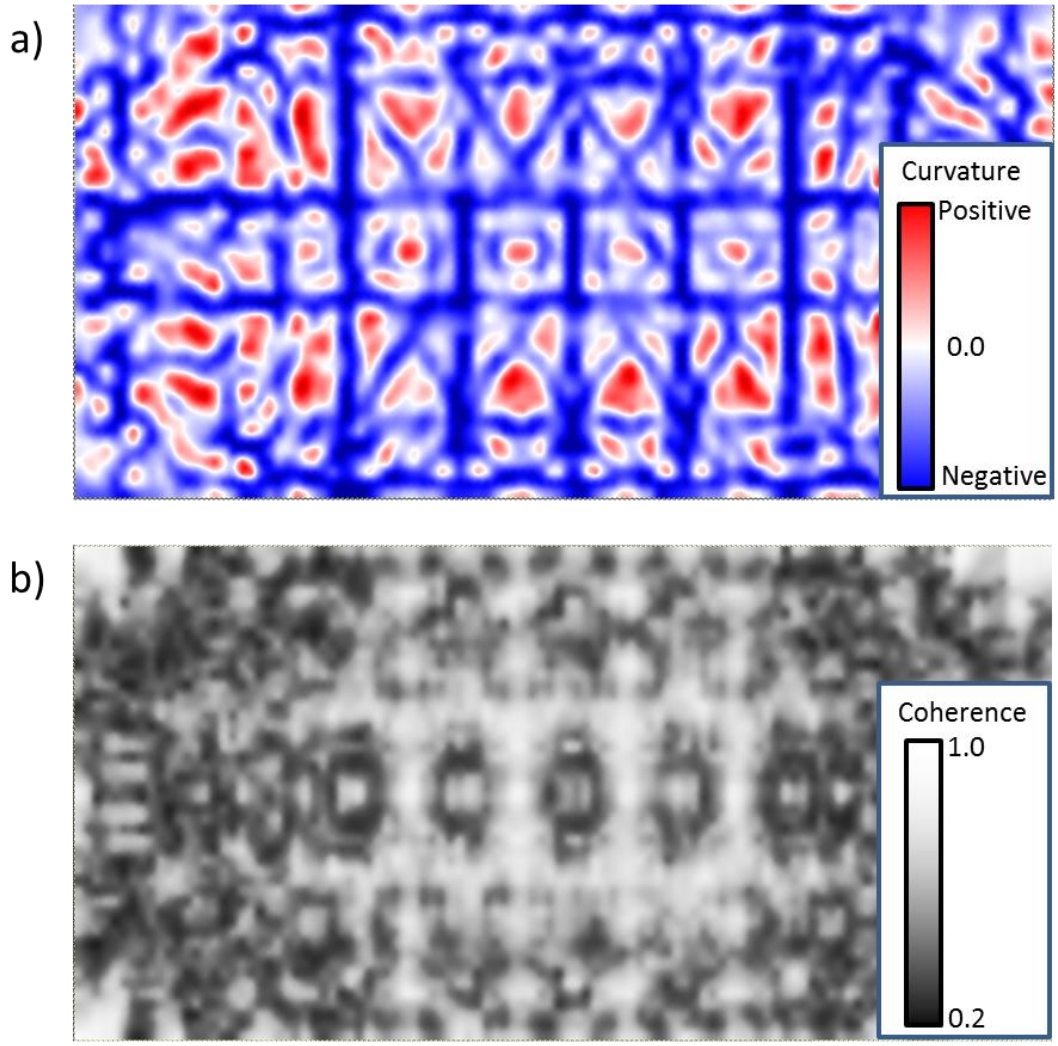

Figure 4.5 (a) Time slice at t=1.320s through most negative curvature of the synthetic seismic data. Notice the undulation anomalies caused by inadequately removed groundroll. (b) Coherence at t=1.320s of the synthetic seismic data. Similar undulation features can be seen causing lateral discontinuity in the reflectors.

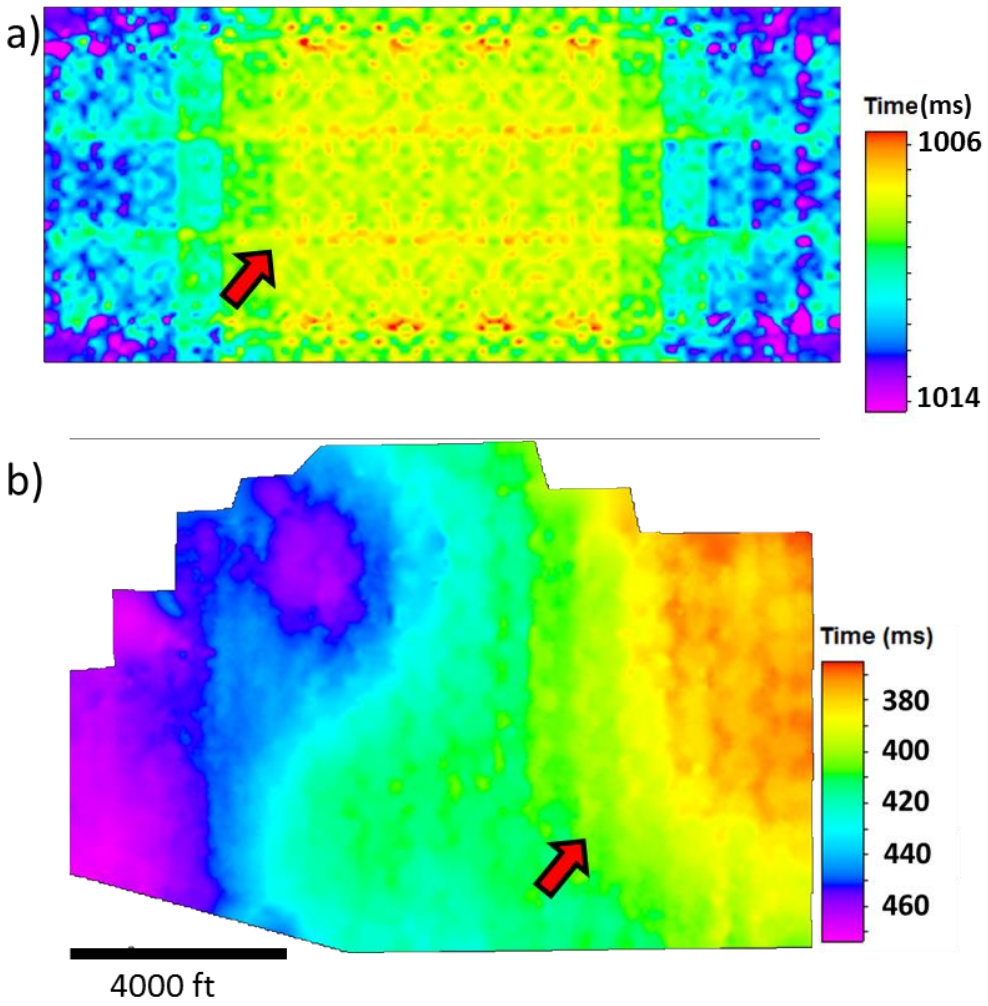

Figure 4.6 Horizons tracked through (a) synthetic data, displayed on Figure 4.4a as green horizon. (b) real seismic data, displayed on Figure 4.4a as yellow horizon. The linear striations (red arrows) are due to residual groundroll overprinting P-wave reflections.

REFERENCES

Cahoj, M. P. and K.J. Marfurt, 2015, Reprocessing 3D seismic data for prestack attribute interpretation, Fort Worth Basin, Jean, TX: To be submitted as M.S. Thesis to the University of Oklahoma.

Cahoj, M. P., S. Verma, B. Hutchinson, J. Qi and K.J. Marfurt , 2015, Pitfalls in seismic processing: part 2 velocity analysis sourced acquisition footprint, Submitted for 85th Annual International Meeting, SEG, Expanded Abstracts.

Chopra, S., G. Larsen, 2000, Acquisition footprint – its detection and removal: CSEG Recorder 25, 16-20.

Cvetkovic M., N. Pralica, S. Falconer, K. J. Marfurt, and S. C. Pérez, 2008, Comparison of some algorithms for acquisition footprint suppression and their effect on attribute analysis, 78th Annual International Meeting, SEG, Expanded Abstracts, 2637-2641.

Hill S., M. Shultz, and J. Brewer, 1999, Acquisition footprint and fold-of-stack plots: The Leading Edge, 18, 686-695.

Marfurt K. J., R. M. Scheet, J. A. Sharp, and M. G. Harper, 1998, Suppression of the acquisition footprint for seismic sequence attribute mapping: Geophysics, 63, 1024-1035.

Marfurt, K. J., and T. M. Alves, 2015, Pitfalls and limitations in seismic attribute interpretation of tectonic features: Interpretation, 3, SB5-SB15.

Verma, S., S. Guo, and K. J. Marfurt, 2014, Prestack suppression of high frequency ground roll using a 3D multiwindow KL filter: Application to a legacy Mississippi Lime survey, 84th Annual International Meeting, SEG, Expanded Abstracts, 4274-4278.

CHAPTER 5 : SEISMIC DATA CONDITIONING

HIGHLY ALIASED GROUNDROLL SUPPRESSION USING A 3D MULTIWINDOW KL FILTER: APPLICATION TO A LEGACY MISSISSIPPI LIME SURVEY

[1]Sumit Verma, [2]Shiguang Guo, [1]Thang Ha, and [1]Kurt J. Marfurt,

[1]The University of Oklahoma, ConocoPhillips School of Geology and Geophysics.

[2]Schlumberger, Houston, Texas, USA.

This paper is submitted to SEG journal Geophysics and is under 3rd revision.

ABSTRACT

While modern recording capacity facilitates dense seismic acquisition, many, if not most, legacy 3D surveys are spatially aliased with respect to groundroll. Irregular topography and weathering zones give rise to groundroll that has piecewise, rather than continuous linear moveout. Dispersion often results in shingled events whose phase velocity cuts across the groundroll noise cone. We present a workflow for the suppression of highly aliased broadband groundroll where modern f-k_x-k_y filters failed. Our workflow begins with windowing and low-pass filtering the data, 3D patch by 3D patch. We then apply linear moveout corrections using the average phase velocity of the groundroll. We compute residual moveout components along the shot and channel axes to account for changes in velocity, thickness, and weathering zone topography about each sample. Using a Kuwahara algorithm, we choose the most coherent window within which we apply a structure-oriented Karhunen–Loève filter to model the coherent noise. Finally,

we remove the linear moveout correction and subtract the modeled groundroll from the original data. We validate our workflow using a synthetic gathers having the same geometry as our field data we then apply our workflow to a merged legacy data volume consisting of four 3D surveys acquired in the 1990's and evaluate its efficacy using modern seismic attribute to map faults and flexures.

INTRODUCTION

Several techniques have been developed for coherent noise suppression in the last 30 years. Groundroll on 2D seismic shot gathers and receiver gathers acquired over flat topography often appears as low frequency noise exhibiting nearly linear moveout. Embree et al. (1963), Treitel et al. (1967) and Kirchheimer et al. (1985) used *f-k* fan filters to remove unaliased groundroll on 2D gathers. However, if the data are coarsely sampled (most legacy land surveys) the groundroll will be aliased in the k_x domain (Foti et al., 2002), such that the aliased component of groundroll may overlap the signal components of the spectrum. Radon, τ-p, and radial transforms have also been applied to groundroll suppression (Russell et al., 1990; Brysk and Mc Cowan, 1986, Henley, 2003). Turner (1990) showed the appearance of spatial aliasing in the τ-p domain. Trad et al. (2003) achieved reduced aliasing using a sparse Radon transform. Although recent developments in "high resolution" Radon transform algorithms have made improvements, irregular moveout of groundroll on rough topography limits their effectiveness even for 2D data.

Liu (1999) modeled groundroll on common shot gathers using the Karhunen-Loève (KL) transform. Liu first picked groundroll alignment functions on each 2D shot gather to flatten the groundroll. He then formed a covariance matrix about the flattened groundroll and computed its eigenvectors and eigenvalues. He reconstructed the coherent groundroll using the strongest eigenvalue eigenvector pairs, and removed the moveout correction. Finally, he subtracted the modeled groundroll from the original data to obtain a filtered result. Done (1999) improved the workflow by defining different window sizes while forming the covariance matrix. Montagne and Vasconcelos (2006) added an alignment function to find the correct velocity to flatten the groundroll. In general, groundroll is dispersive which makes flattening a human intensive process. Figueiredo et al. (2009) partially addressed this issue by muting the top and base of the groundroll zone prior to flattening and application of the KL transform, thereby minimizing any negative impacts on signal outside the noise cone. In a related problem regarding high amplitude tube waves masking upcoming P- and S-waves of interest on a VSP, Mulder et al. (2002) used an adaptation of structure-oriented filtering. Their version filtered within coherent windows and avoided filtering in incoherent windows where the moveout of the tube wave changes due to abrupt vertical changes in velocity. All these methods were applied to 2D data.

In general, simple 2D *f-k* and linear Radon filters do not work well on 3D data, where the travel time from a shot location (x_s, y_s) to a receiver location (x_g, y_g) is given by a hyperbola

$$t = [(x_g - x_s)^2 + (y_g - y_s)^2]^{1/2} \ /V_{gr} \qquad (1)$$

where, V_{gr} is groundroll velocity. f - k filters and Radon filters can be extended to 3D seismic geometries. Gaiser (1995) sorted the 3D gathers by offset, and accounted for unequal trace spacing by computing an $f - x$ domain fan-filter using a least squares approach. Galibert et al. (2002) applied a true f-k_x-k_y filter to 3D seismic data to filter coherent noise. Neither of these methods work if the coherent noise is aliased. Liu and Marfurt (2004) found similar limitations using 3D τ-p-q Radon transform in suppressing coherent noise. Short window, coherence-driven filters often work better in the presence of discontinuous changes in moveout due to variations in topography, thickness and velocity of weathering zone. Using commercial software, D 'Agosto et al. (2003) sorted their 3D data by offset, flattened using an average groundroll phase velocity, and then estimated the coherence and local residual moveout of the groundroll by cross-correlating adjacent trace pairs. For those samples where the coherence exceeded a processor-determined threshold, the groundroll was estimated using the cross-correlation coefficient and subtracted.

We begin our paper with a description of the exploration objectives, data acquired and failure of conventional processing techniques (in piecewise continuous dispersive groundroll removal). We then addressed this problem by adapting a well-established edge preserving structure oriented filter (e.g. Marfurt, 2006) to enhance piecewise continuous dispersive groundroll, acquisition patch by acquisition patch. We apply this workflow to a legacy low fold merged survey contaminated by high amplitude, broadband, dispersive groundroll. We validate the efficacy of our algorithm by computing geometric attributes sensitive to noise and geologic discontinuities. We conclude with a summary of the value and limitations of this workflow.

EXPLORATION OBJECTIVES AND DATA DESCRIPTION

Our study area lies between the Midland Basin (Permian Basin) and Fort Worth Basin, Texas. In this area, there is no Barnett Shale, such that the Mississippi Lime lies directly above the Ellenburger Limestone at a depth of 6000-8000 ft (1825-2450 m). The target in our study area is shallow, at approximately t = 1.2 s., the surface infrastructure is in place, and many small operators already hold acreage from shallower or deeper production. Advancements in horizontal drilling, acidation, hydraulic fracturing, and efficient disposal of large volumes of water make these reservoirs economic. In contrast to some shale resource plays, the Mississippi Lime is highly heterogeneous laterally. The major rock types are tripolitic chert, fractured tight chert, and tight limestone. The tripolitic and fractured chert have good porosity and good production in northern Oklahoma and southern Kansas.

Four seismic surveys were shot in the early 1990's, three of which had EW receiver lines and one with NS receiver lines (Figure 5.1a). The merged surveys cover an area of 80 mi^2 (207 km^2). Initially, we followed the conventional land processing workflow for Mississippian play after Dowdell (2013) and Aisenberg (2013) including iterative static and velocity analysis, and prestack time migration. Unfortunately, the resulting images were still contaminated by acquisition footprint (Figure 5.1b and c). The seismic data are very low fold (average fold ~15) (Figure 5.1a). Examination of the migrated gathers (not shown) reveals strong groundroll aliasing. On the original shot gathers, the groundroll appears as high amplitude, aliased, coherent events that persist up

to 50 Hz (Figure 5.3a and b). Modern 5D interpolation can often suppress footprint (Chopra and Marfurt, 2013). Using such a 5D interpolation workflow, reflectors are flattened through careful velocity picking and statics corrections prior to interpolation. Diffractors are only partially flattened such that edges in 5D interpolated volumes are somewhat smeared, but footprint free. Groundroll is not flattened and is incorrectly interpolated producing the inferior image seen in Figure 5.2.

The four surveys were acquired using vibrator sweeps of 14-90 Hz and 12-85 Hz. The presence of groundroll up to 50 Hz (Figure 5.3b) precludes the use of a simple low-cut filter. The aliasing which prevents accurate 5D interpolation also prevents the use of modern f-k_x-k_y filtering.

In this paper we build on the coherent noise modeling concepts developed by Mulder et al. (2002), d'Agosto et al. (2003), Liu (1999), and Done (1999) as well as modern 3D edge preserving structure oriented filtering (Marfurt, 2006) and apply them to the 3D data volume, patch by patch. We recognize that the groundroll (1) is high amplitude, (2) is band limited (f< 50 Hz), (3) exhibits outgoing low group and phase velocity with few backscattered events, and (4) is piecewise coherent. We are also fortunate that our data were acquired in patches (Figure 5.4), facilitating the implementation of a 3D dip filter across channel number and shot number dimensions.

METHOD

Figure 5.5 summarizes our workflow. The seismic data includes geological reflections of all frequency ranges (12-85 Hz). Our first step is to apply a low pass filter (Figure 5.6a), $f < 50$ Hz (10-15-45-55 Hz) that removes the signal in the higher frequency range ($50 < f < 85$ Hz). The second step is to window the groundroll contaminated zone based on an average group velocity of 1000 m/s (Figure 5.6b). In this manner, subsequent filters will not impact reflection events outside the groundroll window. In the third step (Figure 5.6c), we apply a linear move out (LMO) correction using groundroll phase velocity v = 1500 m/s (5000 ft/s), thereby approximately flattening the shingled groundroll events and misaligning the higher apparent velocity geological reflections of interest. At this point, we have created a patch of data (Figure 5.4) that is amenable to 3D edge preserving structure-oriented filtering (Marfurt, 2006).

We compute the residual inline (Figure 5.7a) and crossline components of linear moveout as well as coherence (Figure 5.7b) within each and every 3 channel by 3 shot by 0.020 s analysis window. Each sample forms part of 9 spatial by 21 vertical (or 189) windows. The most coherent Kuwahara (1976) window (i.e. the one that best represents moderately dipping coherent groundroll) is used for subsequent analysis (Figure 5.8). If the window is sufficiently coherent ($c > 0.3$) we apply a Karhunen–Loève (KL) filter to model the strongest event (the moveout-corrected groundroll) at the current sample of interest. If the window is incoherent ($c < 0.2$), only misaligned signal (or random noise) exists, and no filter is applied. We blend the modeled noise and signal for value of $0.2 < c < 0.3$.

We apply inverse linear moveout after the KL filter (Figure 5.7) to obatin the modeled groundroll (Figure 5.9a). Finally we subtract the modeled groundroll from the original data. A major advantage of KL filtering is that the scale of the seismic amplitude does not change. A simple subtraction therefore is effective and sufficient (Figure 5.9b). In this workflow, the most important parameters are the high cut frequency, linear moveout velocity, window size, and the threshold values of coherence. We obtain the high cut frequency by simply applying bandpass filters to the gather to determine at which frequency band the groundroll is sufficiently low in amplitude. Since we know our data are dispersive and will need to search for residual linear moveout we only need an approximate phase velocity of groundroll. The size of vertical analysis window used in the KL filter should be smaller than the dominant groundroll period to avoid vertical mixing of events. If the widow is too large, vertical samples that correspond to different groundroll phase velocities will be smeared, reducing the amount of noise that can be modeled. When using a nine-trace (three shots into three channels) window, we find that the first two eigenvectors (rather than simply the first eigenvector) better estimate the groundroll. Coherence is computed as the ratio of the energy represented by the first two eigenvectors to that of the original data. After linear moveout using the groundroll group velocity, reflection events are in general strongly overcorrected and aliased such that this appears as low coherence zones in the flattened data volume. By co-rendering coherence plotted against a polychromatic color bar with seismic amplitude data plotted as a gray scale one can easily choose a cut off value of coherence below which there is no significant groundroll present.

Validation with a Synthetic patch

We generated prestack synthetic data to validate our groundroll suppression workflow. First we created a model with very shallow layers and velocity increasing with depth, in order to generate dispersive groundroll. We then created a second model with deeper layers to generate reflections. We combined the results of the two models to generate the final synthetic. We then generated a synthetic 3D patch using geometry representative of our real seismic data (Figure 5.10a). We implemented the groundroll suppression workflow described in this paper to remove the dispersive groundroll. Figure 10b shows that most of the dispersive groundroll was removed while the reflectors were preserved. It is important to notice that the groundroll at near offsets appears to be an incoherent event and could not be removed by this technique.

APPLICATION

Comparing the shot gathers before (Figure 5.3a) and after groundroll suppression (Figure 5.9b) shows that we remove the highly aliased groundroll and preserve the reflection events of interest. When sorted to CMP super gathers, the filtered data provides significantly improved velocity spectra.

Calculating coherence attribute after groundroll suppression (Figure 5.11b), we observe that the footprint is minimized and geological structures are enhanced. After migration, we applied two passes of prestack structure oriented filter and one pass of post-stack structure oriented filter (Marfurt, 2006; Höcker and Fehmers, 2002) to remove more random noise from the data (Figure 5.12).

In order to verify the applicability of the method, we applied the groundroll suppression method to a second data set. These legacy data were acquired in 1990 over the Central Basin Platform, Texas, USA, and is representative of the much of the data used to drill horizontal wells in this important shale oil resource play. Figure 5.13 indicates that this method successfully eliminates the aliased groundroll.

CONCLUSIONS

We have adopted concepts of edge preserving structure oriented filtering commonly used to improve the continuity of reflectors in 3D migrated data volumes to modeling groundroll in LMO corrected acquisition patches. Through shot and channel 3D residual moveout search, within overlapping windows we are able to model piecewise continuous, dispersive noise trains.

We show by application to two data volumes that our workflow provides excellent results when applied to aliased groundroll suppression where f-k_x-k_y techniques fail. The explicit search for sample-by-sample phase velocities allows the filter to adapt to dispersive groundroll wave trains. The short, overlapping 3D window implementation allows the filter to model piecewise continuous groundroll events that are broken by irregular topography and discontinuities in the weathering zone. The suppression of groundroll provides more accurate velocity analysis and preconditions the data for subsequent 5D interpolation. Coherence slices show that random noise is suppressed while edges are preserved. Our surveys are dominated by radially-traveling groundroll, allowing us to approximate the moveout using a user defined velocity and the source-receiver offset. If backscattered groundroll were a problem (Strobbia et. al, 2014), a more

computationally intensive search about a 3D moveout cone rather than within the source-receiver sagittal plane would be required.

ACKNOWLEDGEMENTS

We acknowledge Clear Fork Inc. for data support. ProMAX (by Haliburton) and VISTA (by Schlumberger) software were used for seismic data processing. Bo Zhang, Mark Aisenberg and Marcus Cahoj provided valuable insight in seismic processing. Finally, thanks to the industry sponsors of the AASPI Consortium for their financial support.

FIGURES AND TABLES

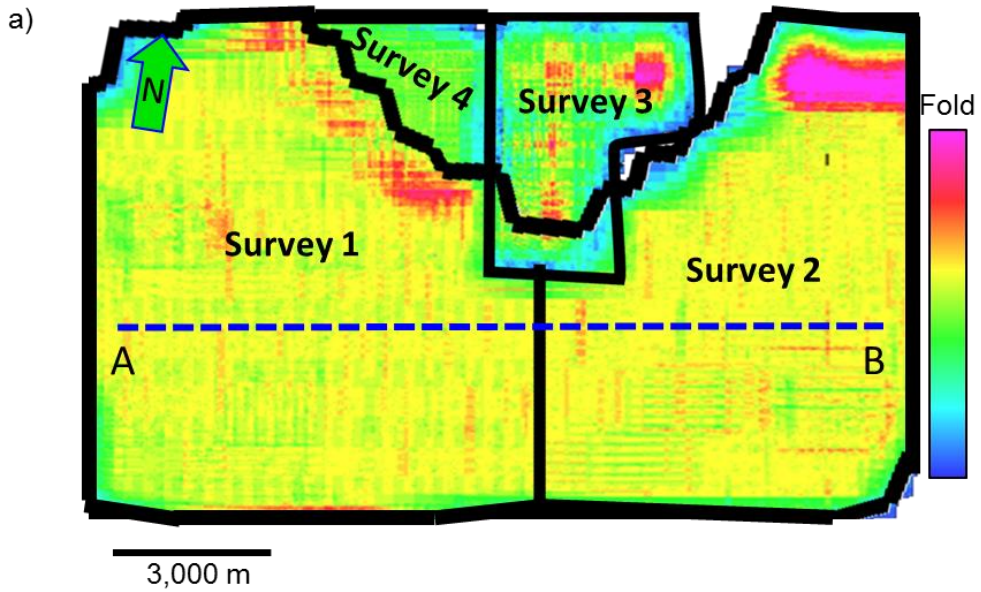

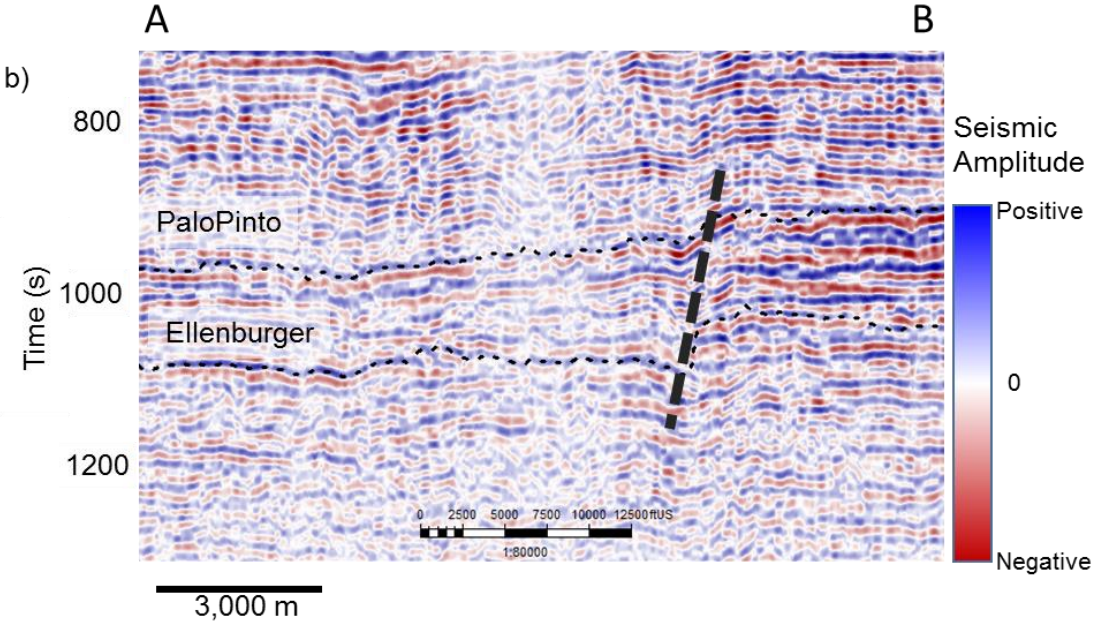

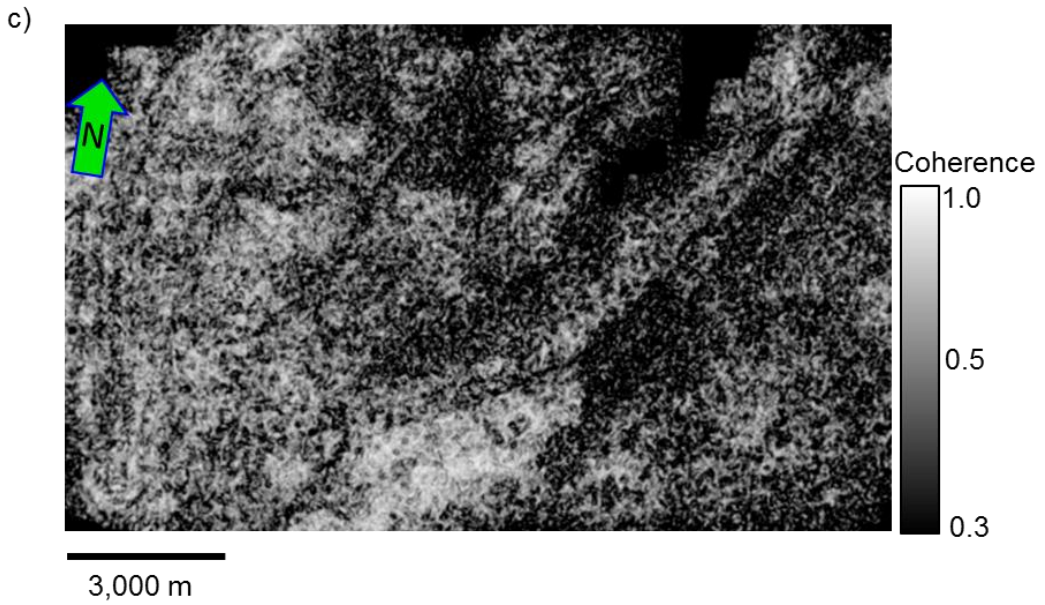

Figure 5.1 (a) Fold Map of the four merged surveys. Before reprocessing (b) vertical section of seismic amplitude (c) time slice at *t* =1.1 sec at the level of Mississippian chert for coherence. Note the strong EW and NS footprint in both images (indicated by yellow arrow).

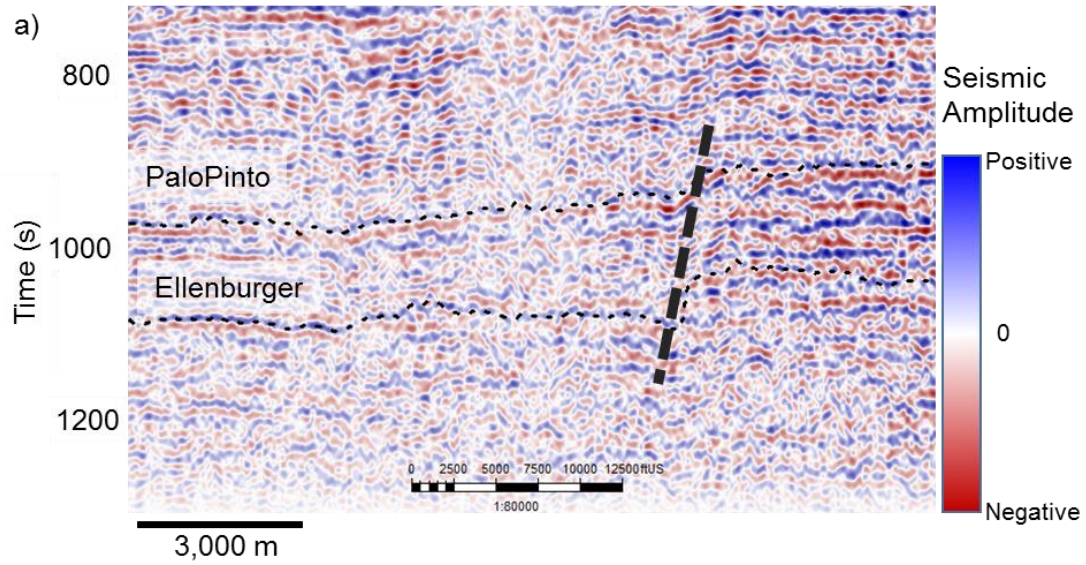

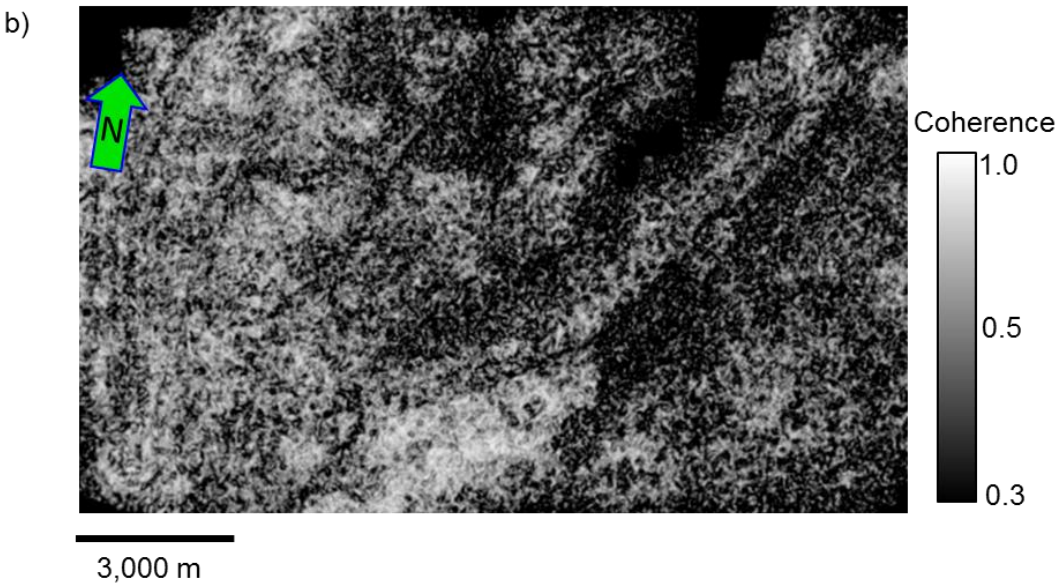

Figure 5.2. After 5D interpolation before eliminating coherent noise (a) vertical section of seismic amplitude (b) time slice at t =1.1 sec at the level of Mississippian chert for coherence. Notice footprint seen in Figure 5.1c appears to be interpolated.

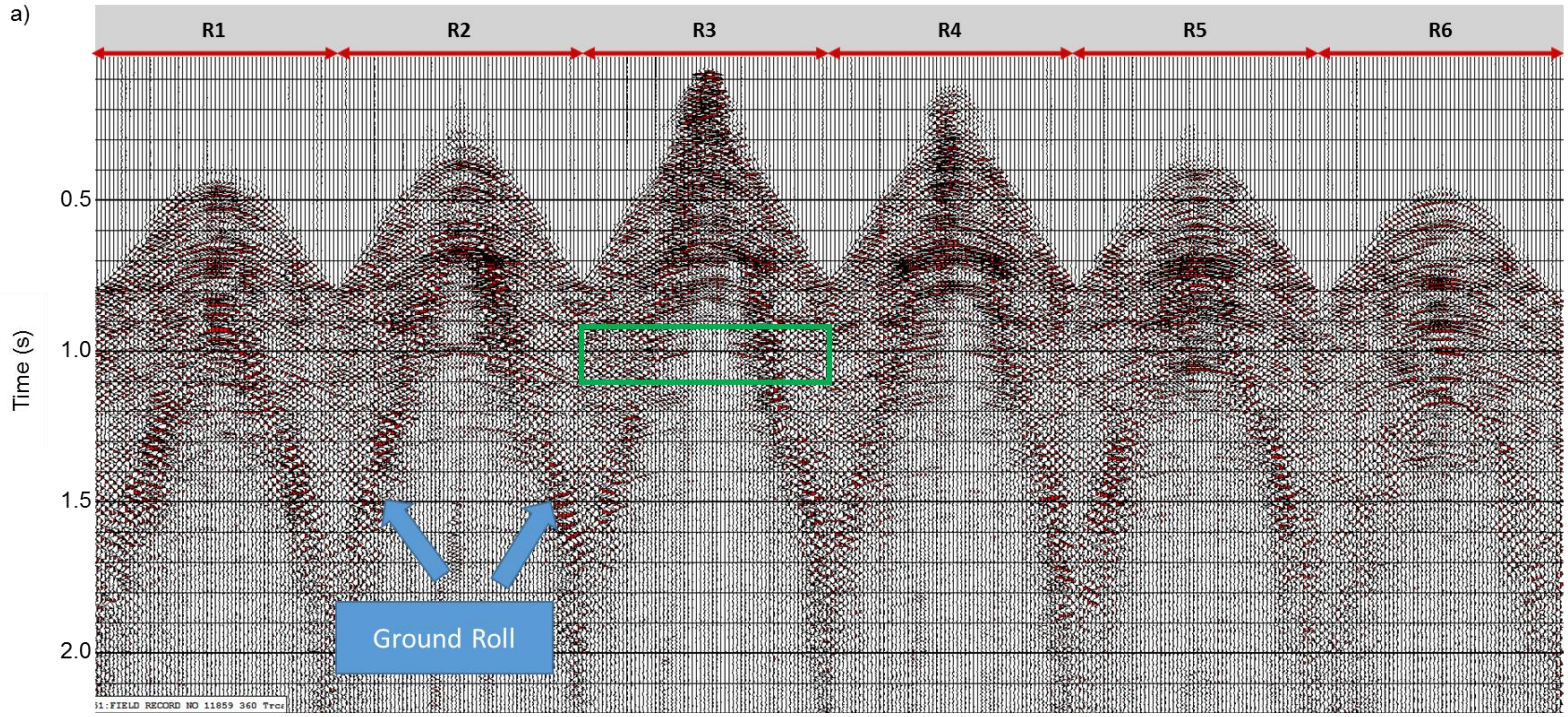

Figure 5.3. (a) A representative shot gather (sorted by shot vs channel) before ground roll suppression. Figure 4 shows the geometry of receiver lines R1-R6 for this shot. (b) Bandpass filtered 40 Hz <f < 50 Hz image shows ground roll having high frequency components masking the target zone (indicated by the green rectangle).

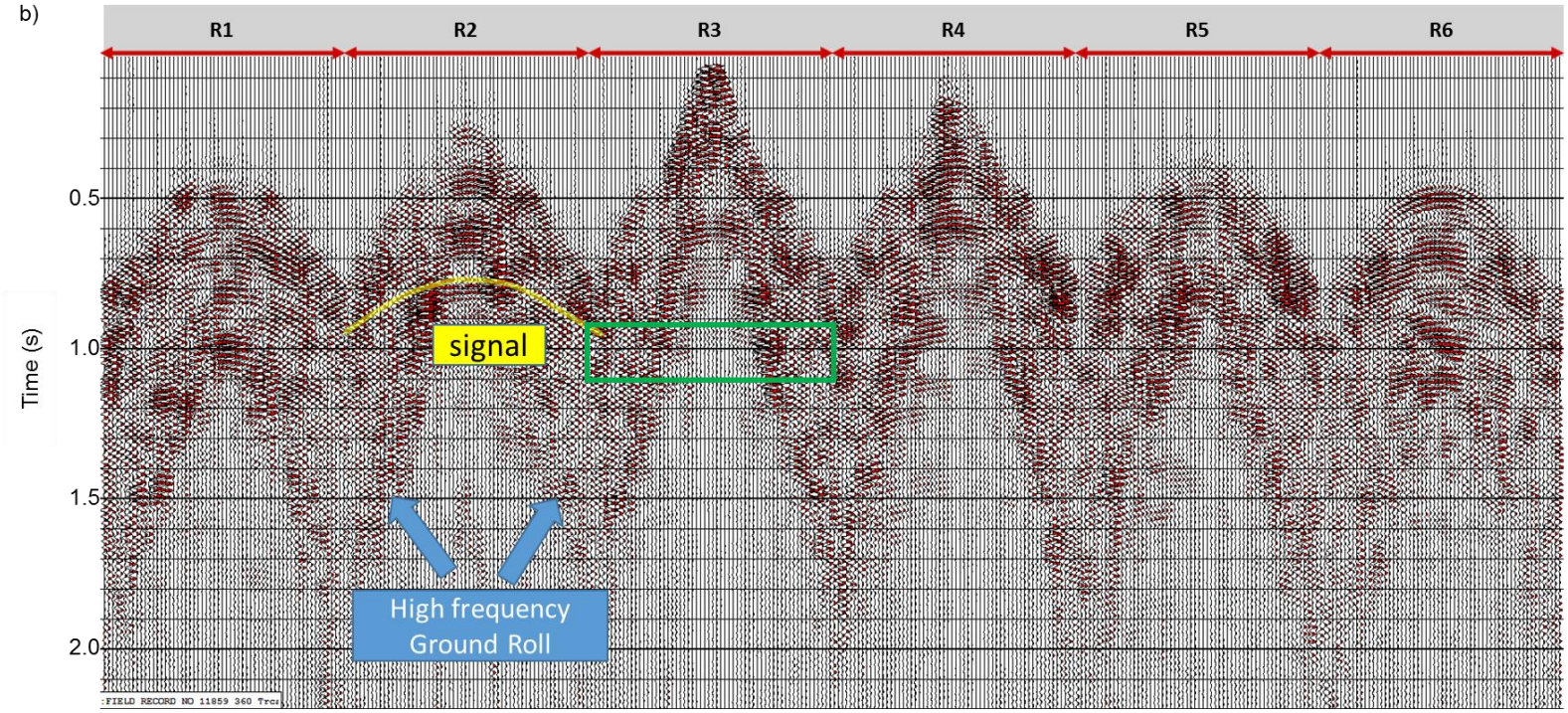

Figure 5.3 (a) A representative shot gather (sorted by shot vs channel) before ground roll suppression. Figure 4 shows the geometry of receiver lines R1-R6 for this shot. (b) Bandpass filtered 40 Hz <f < 50 Hz image shows ground roll having high frequency components masking the target zone (indicated by the green rectangle).

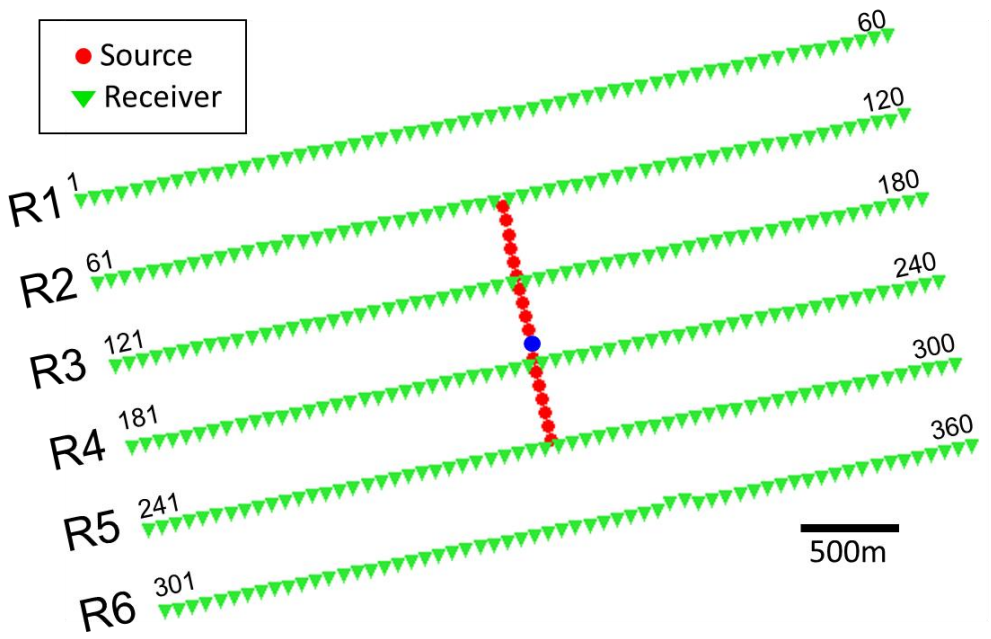

Figure 5.4. A representative receiver patch. The common shot gather associated with source location indicated by blue dot is shown in Figure 5.3. These 18 sources into 360 channels forms an 18x360 trace 3D seismic volume. If we flatten the noise in this volume using linear moveout, we can use multiwindow structure oriented filters to model it.

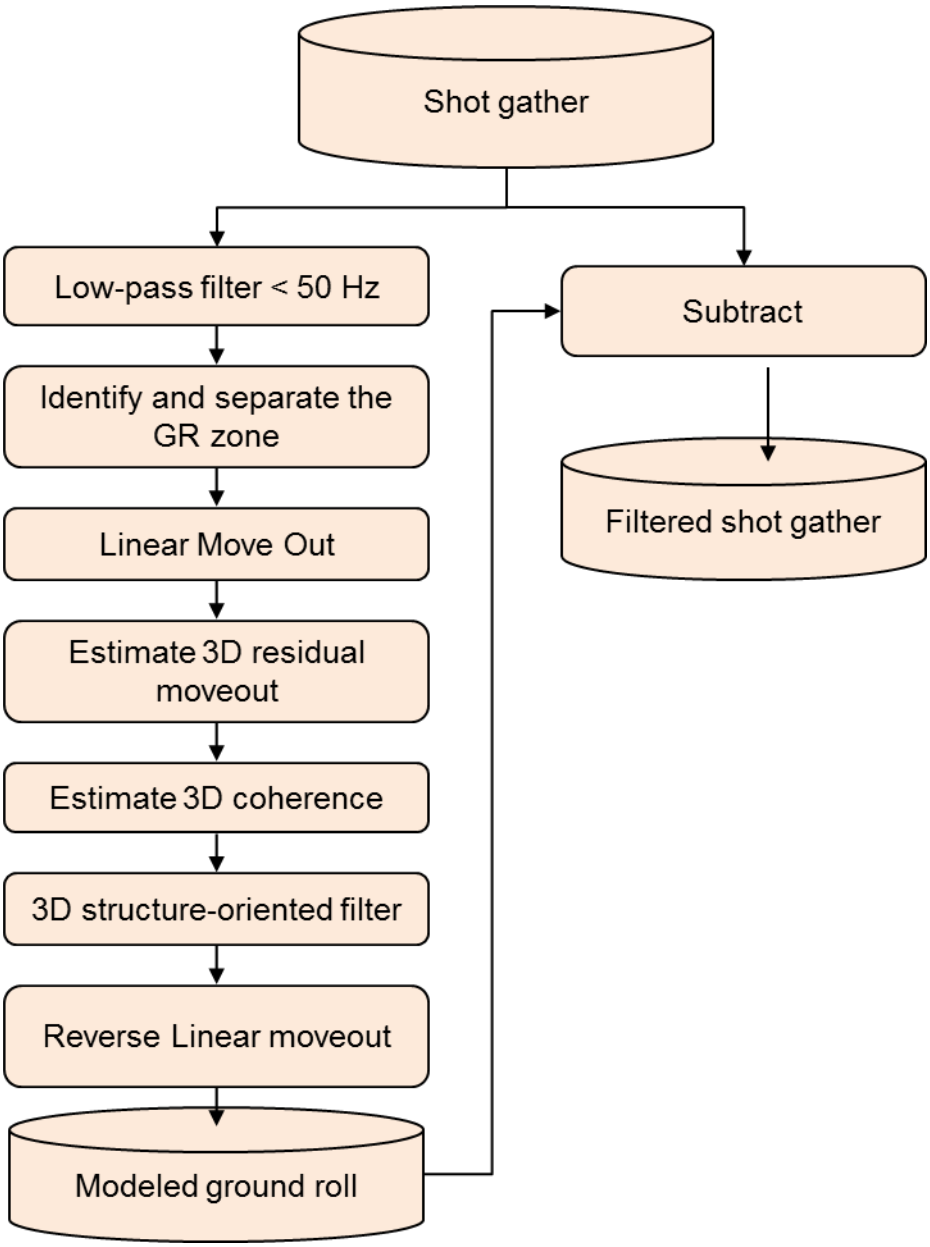

Figure 5.5. The groundroll suppression workflow presented in this paper.

a)

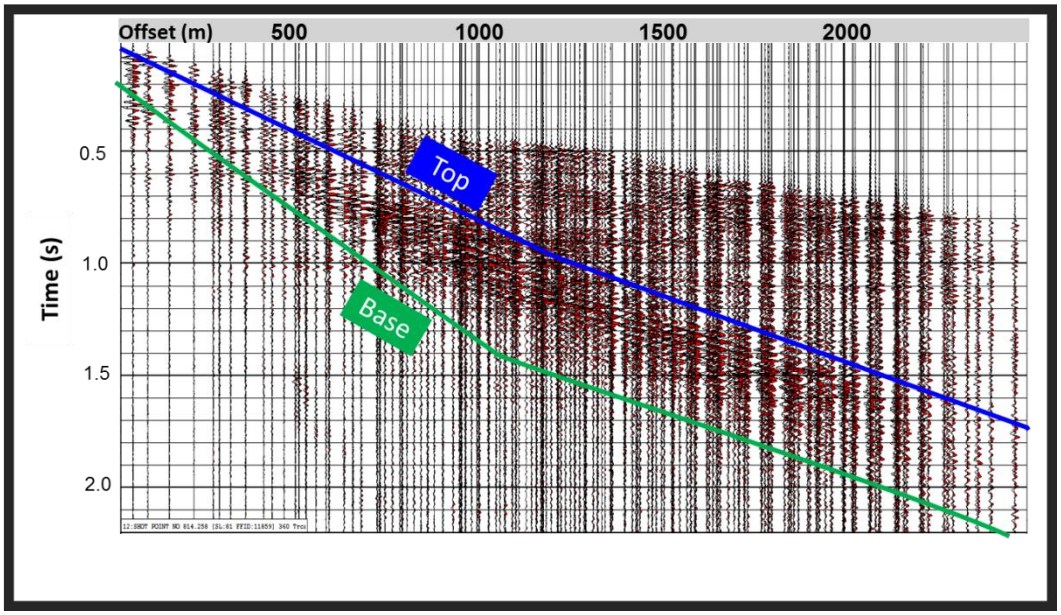
Offset (m)
500
1000
1500
2000
Time (s)
0.5
1.0
1.5
2.0
Top
Base

b)

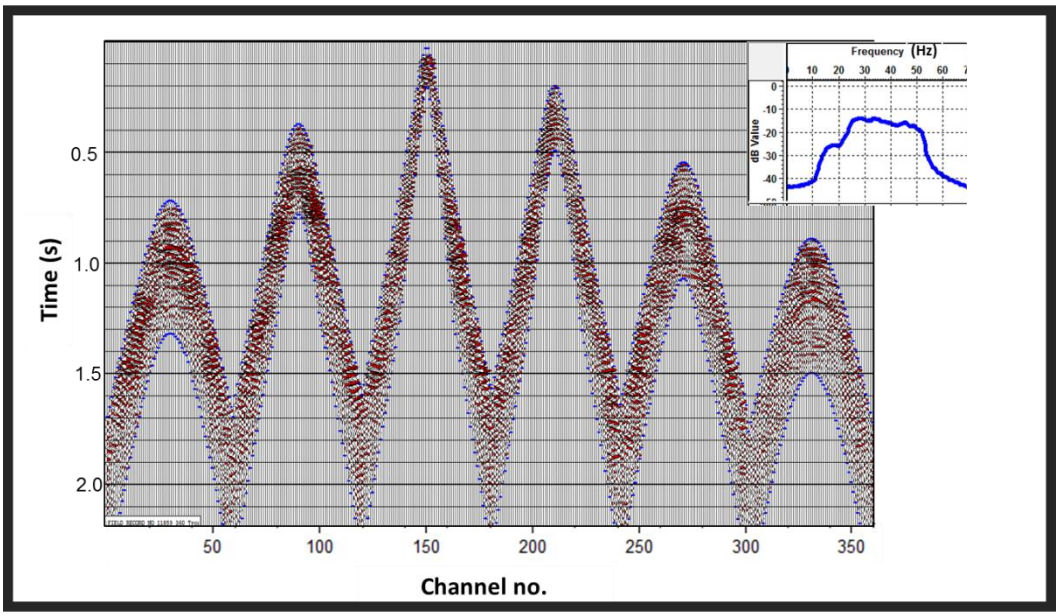
Frequency (Hz)
10
20
30
40
50
60
dB Value
0
-10
-20
-30
-40
Time (s)
0.5
1.0
1.5
2.0
50
100
150
200
250
300
350
Channel no.

c)

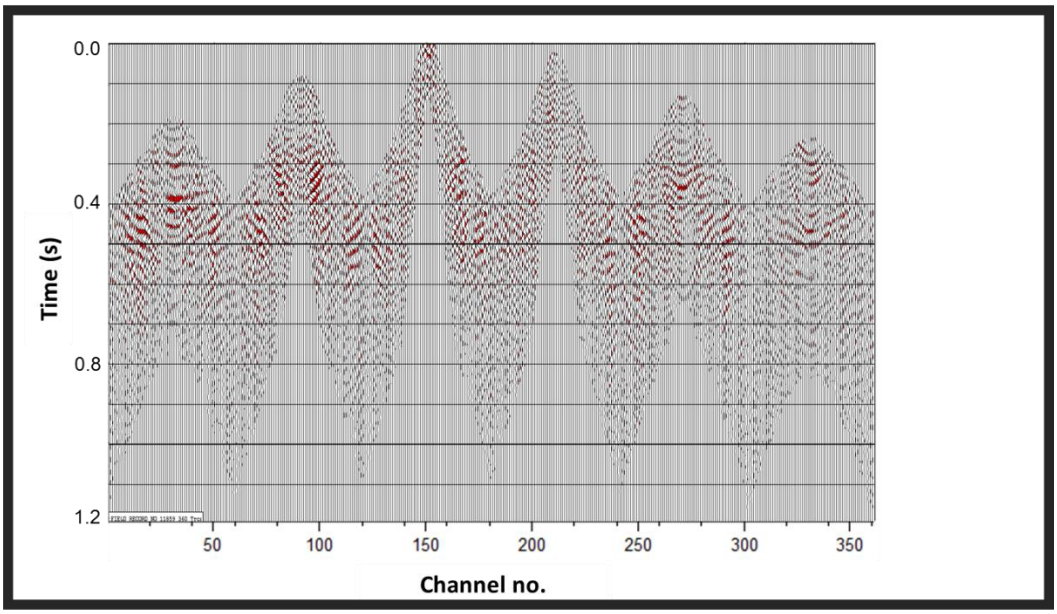

Figure 5.6. (a) Common shot gather sorted by absolute offset x after a high cut filter removing reflections with f >50 Hz, strong ground roll window indicated by top and base mutes parallel to the group velocity of approximately 1000 m/s. (b) Windowed data shown sorted by common shot vs channel number. (c) The same gather after linear moveout using a phase velocity of v=1524m/s (5000 ft/s). Note the ground roll events are relatively flat while the underlying signal is steeply dipping.

a)

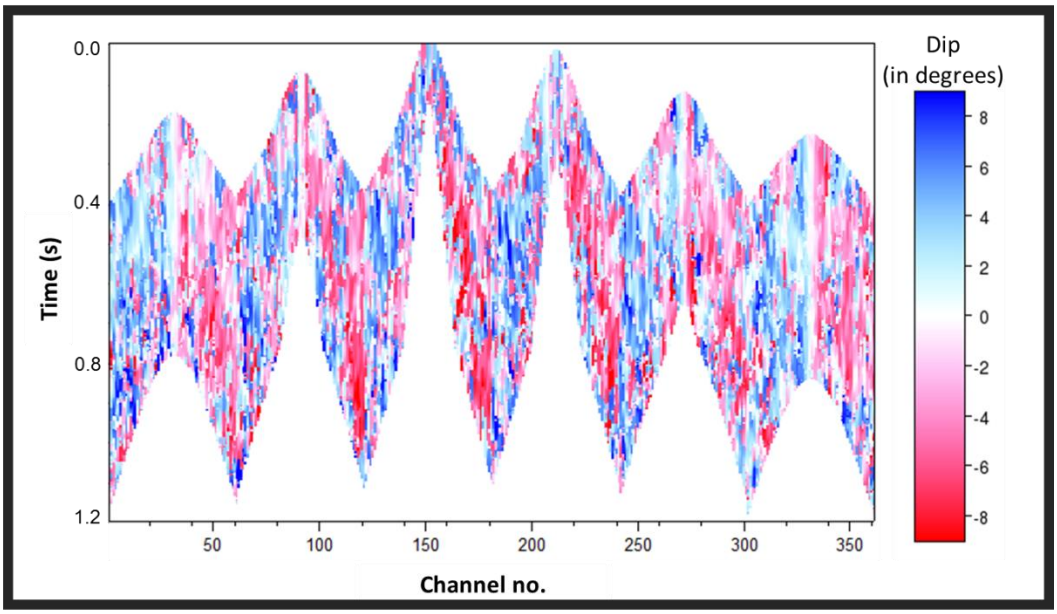

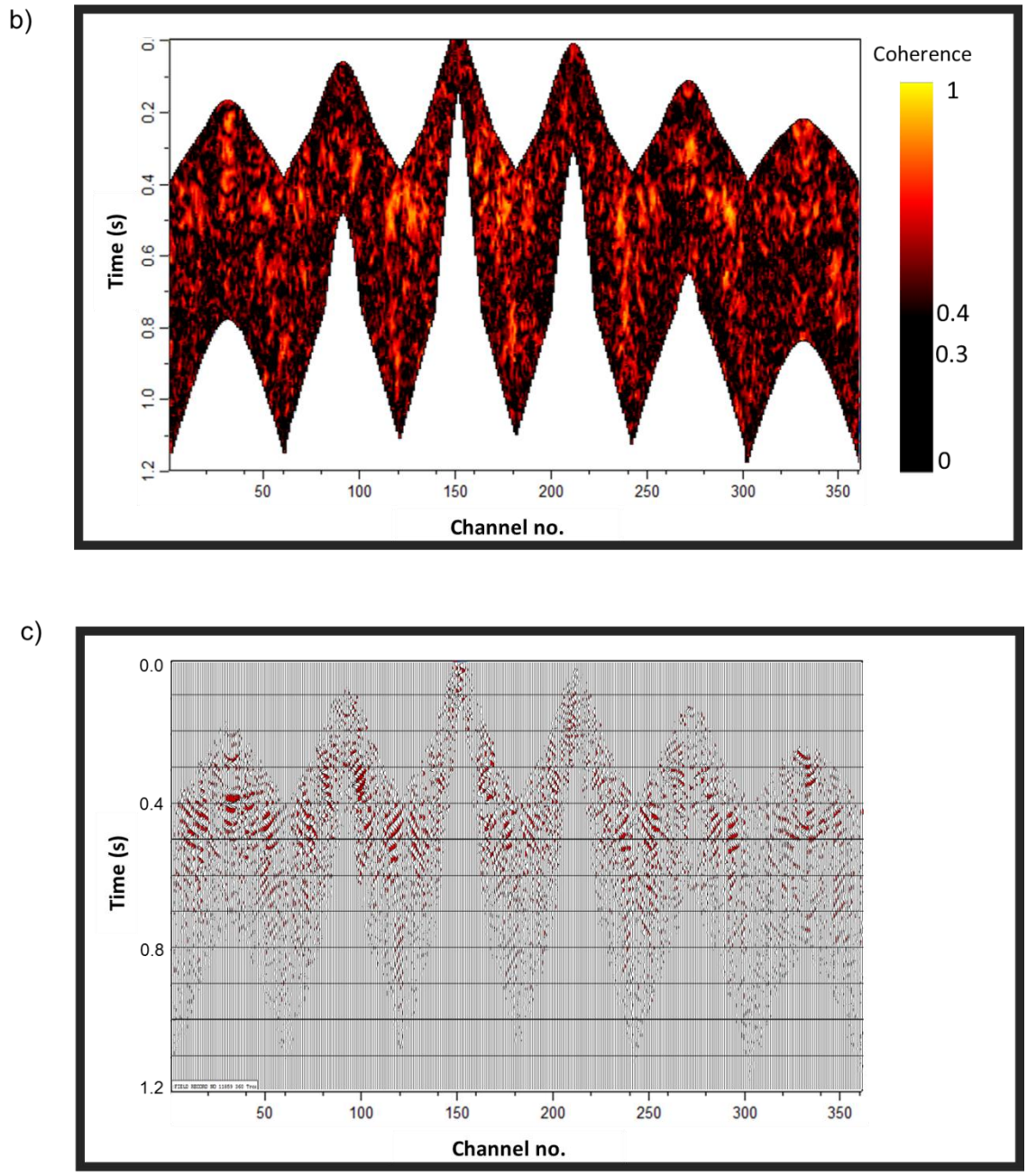

Figure 5.7. (a) Local residual linear moveout (dip) in Inline direction, where increasing channel numbers are "in-line" and increasing shot numbers are "cross-line" in reference to the 18x360 trace patch geometry. Crossline dips are computed but not shown. (b) Coherence computed on the windowed, flattened patch, high coherence indicates coherent ground roll. (c) Modeled ground roll using a Karhunen-Loeve filter within those windows exhibiting a coherence, $c > 0.3$.

Process	Run Time per 2 processors per patch(= 6480 traces)		Survey parameters	
Residual dip search	135 sec		No. of Shots per patch	18
Coherence	120 sec		No. of Samples per trace	1000
K-L Filter	105 sec		Total no. of receivers for each shot	360

Table 5.1. Computation cost for the processes.

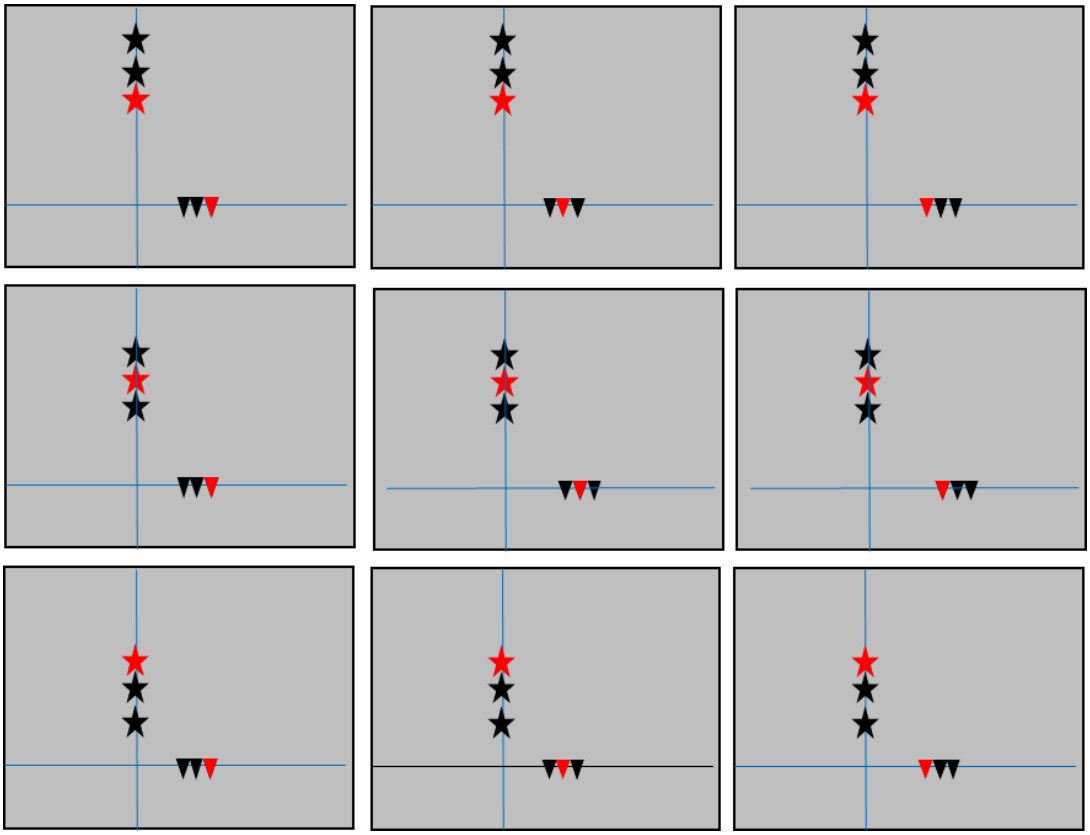

Figure 5.8. A simplified cartoon showing a suite of nine overlapping 3 shot by 3 receiver Kuwahara (1976) windows used to filter the ground roll. The red star and triangle indicate the target trace to be filtered such as the blue shot point into a channel on receiver line R5 in Figure 4. First we compute the coherence along local 3D dip for each of the nine windows. The window with the highest coherence value best represents the coherent ground roll. Within this window, we then apply a 9-trace Karhunen Loeve filter along dip to model the desired ground roll for the red source-receiver pair. In actual implementation, we also allow our windows to vary vertically over ±10 samples, such that we search 21x9 =189 windows, all of which include the target time sample at the target shot-receiver trace.

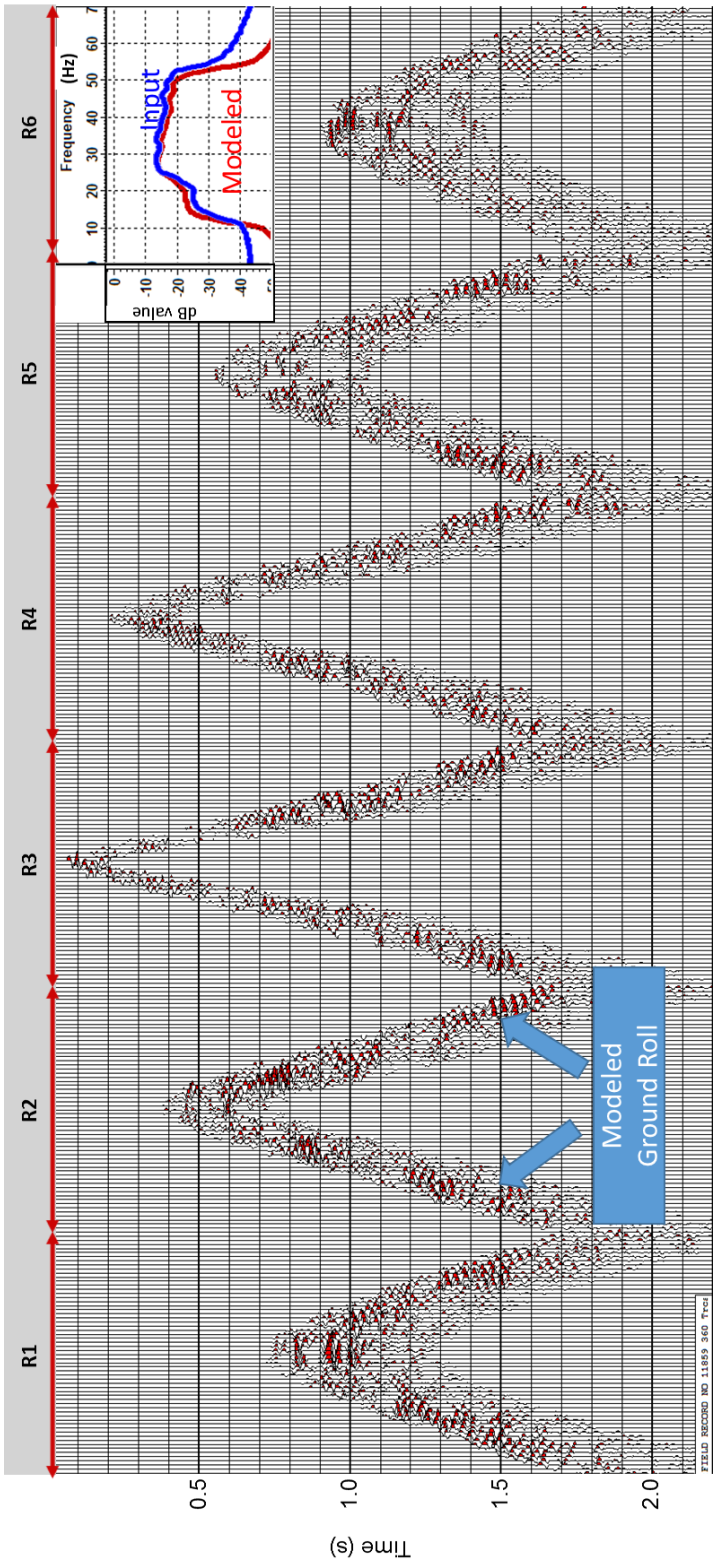
R1
R2
R3
R4
R5
R6
Modeled
Ground Roll
Input
Modeled
Frequency (Hz)
db value
Time (s)
0.5
1.0
1.5
2.0

b)

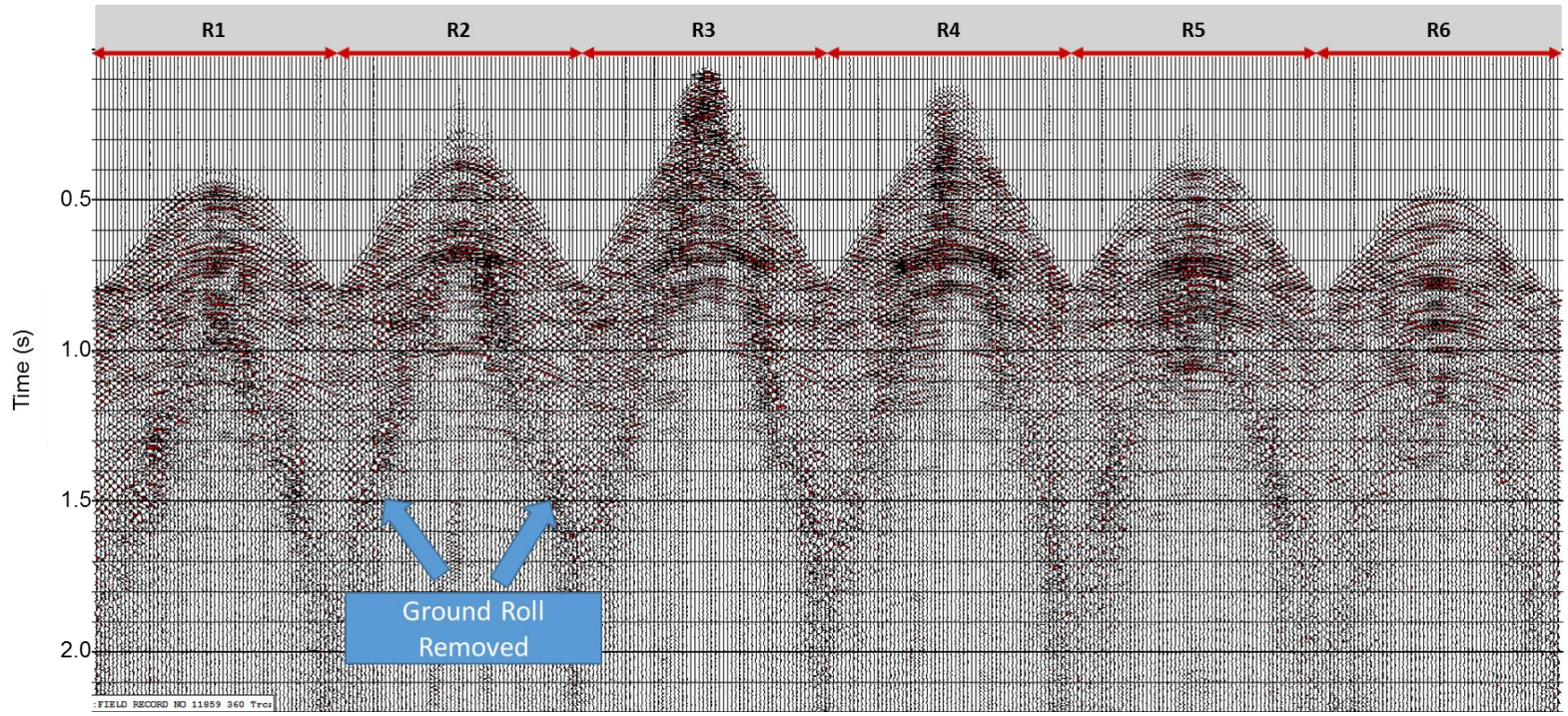

c)

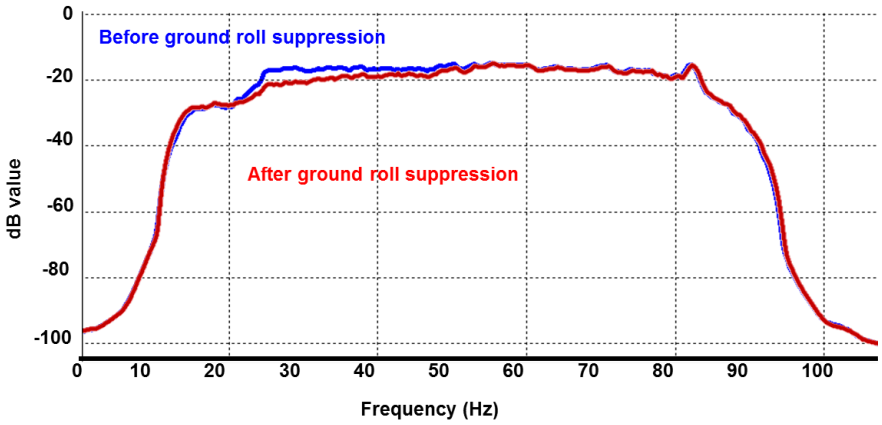

Figure 5.9 (a) Modeled ground roll, after reverse linear move on the gather shown in Figure 5.7c. Notice that the modeled ground roll has dominant frequency range of 25-40 Hz. (b) The same shot gather (sorted by shot vs channel) after ground roll suppression, obtained by subtracting modeled ground roll (Figure 5.9a) from the original gather (Figure 5.3a). (c) Amplitude spectrum of seismic shot gather before (in blue) and after (in red) ground roll suppression.

a)

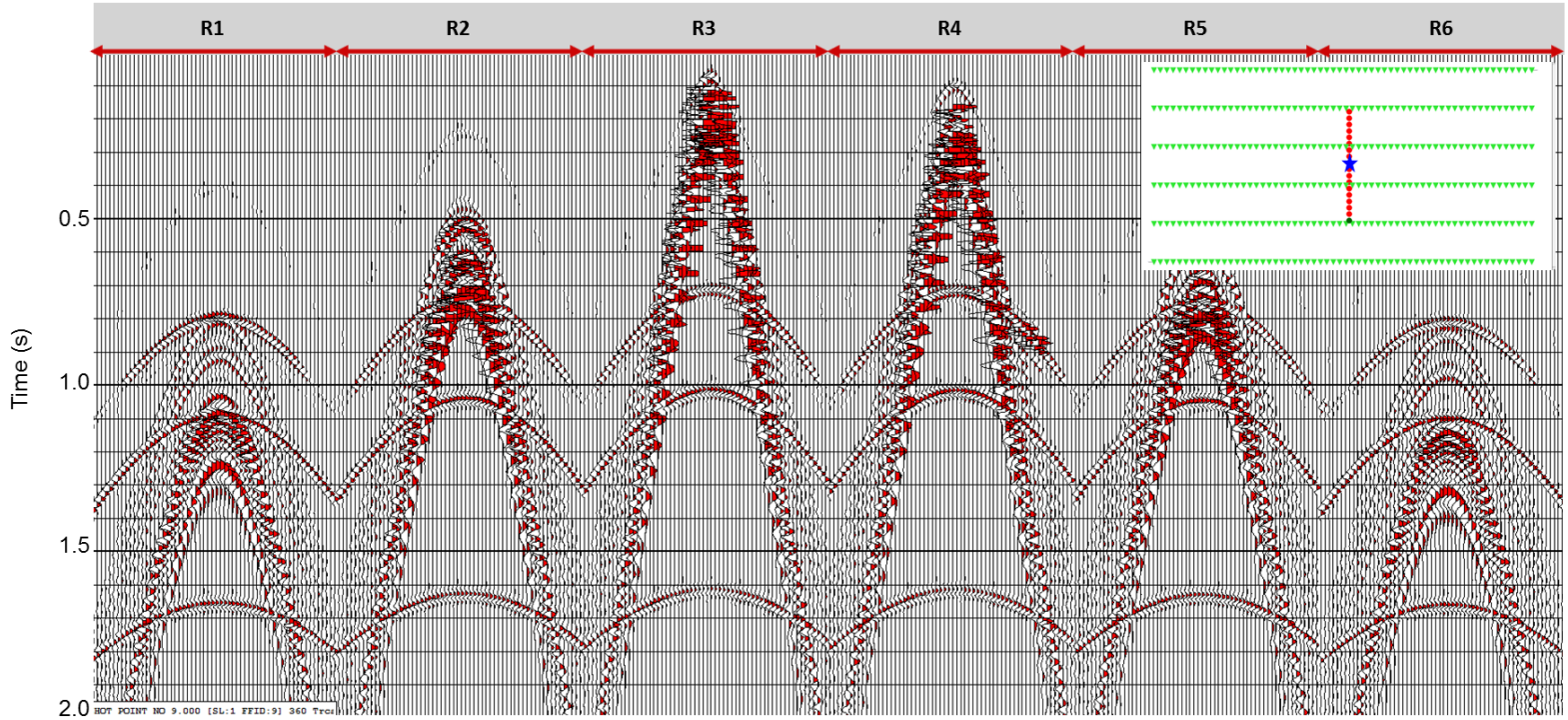

Figure 5.10. Synthetic prestack gather data generated with 18 sources and 360 channels, the acquisition patch is shown in the upper right corner of the figures. Shot vs channel gather for blue source (a) before ground roll suppression (b) after ground roll suppression (c) removed coherent noise.

b)

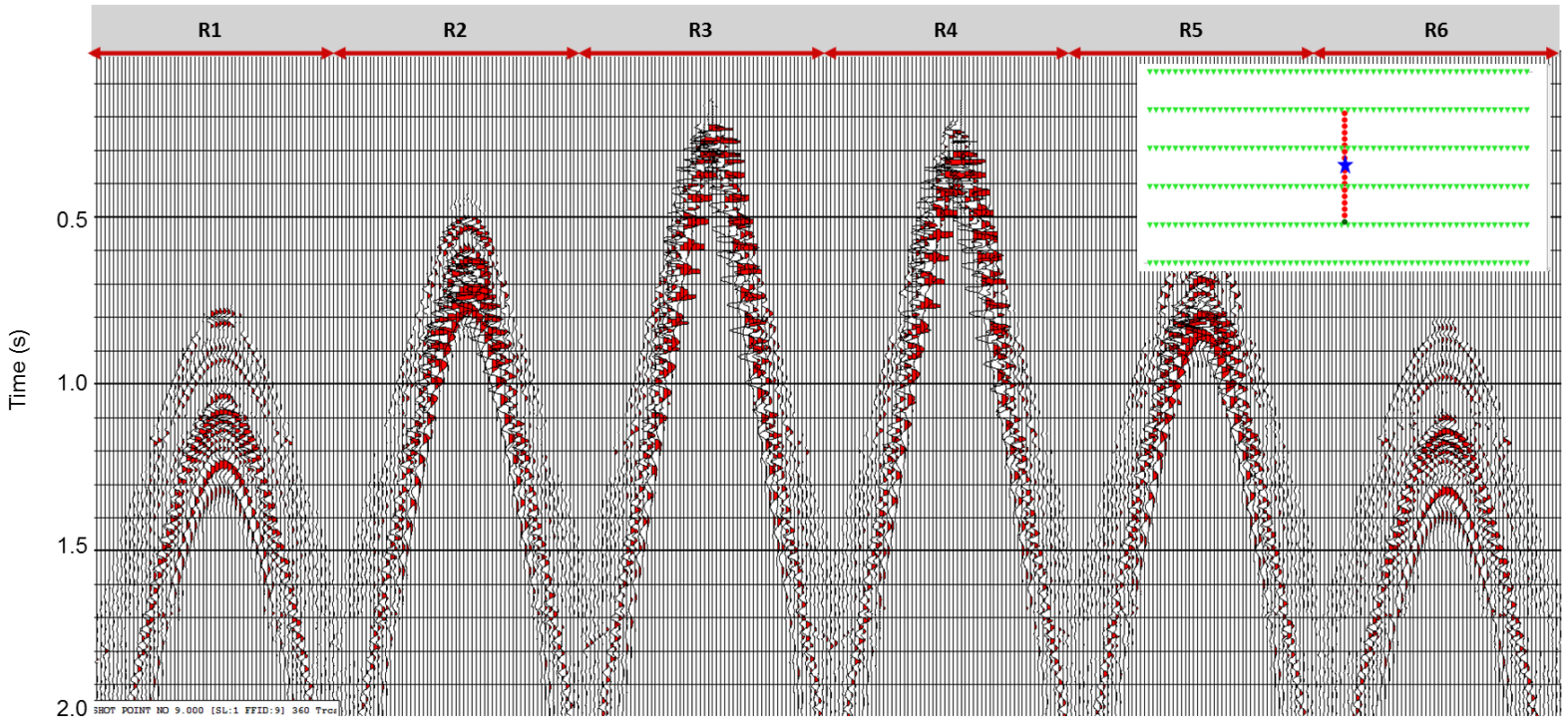

Figure 5.10. Synthetic prestack gather data generated with 18 sources and 360 channels, the acquisition patch is shown in the upper right corner of the figures. Shot vs channel gather for blue source (a) before ground roll suppression (b) after ground roll suppression (c) removed coherent noise.

c)

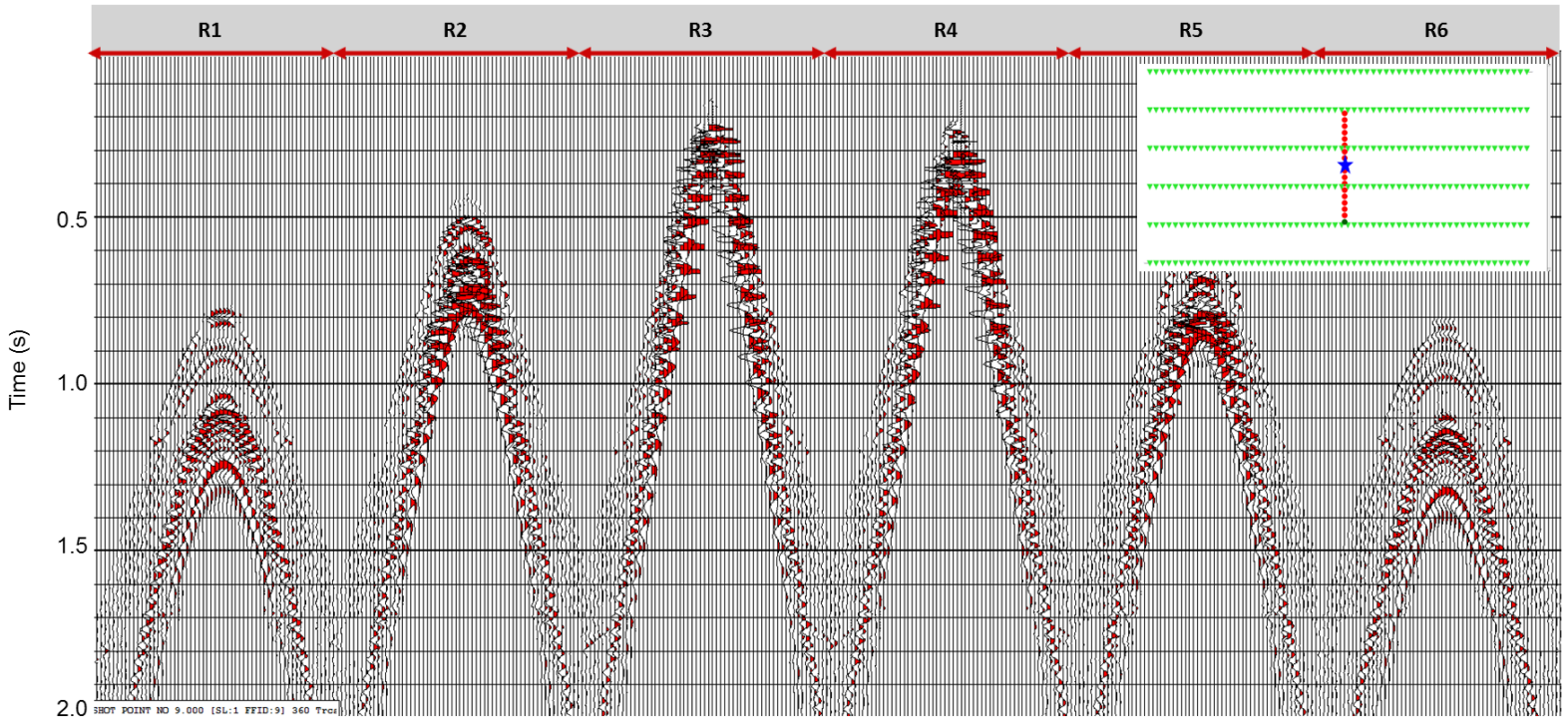

Figure 5.10. Synthetic prestack gather data generated with 18 sources and 360 channels, the acquisition patch is shown in the upper right corner of the figures. Shot vs channel gather for blue source (a) before ground roll suppression (b) after ground roll suppression (c) removed coherent noise.

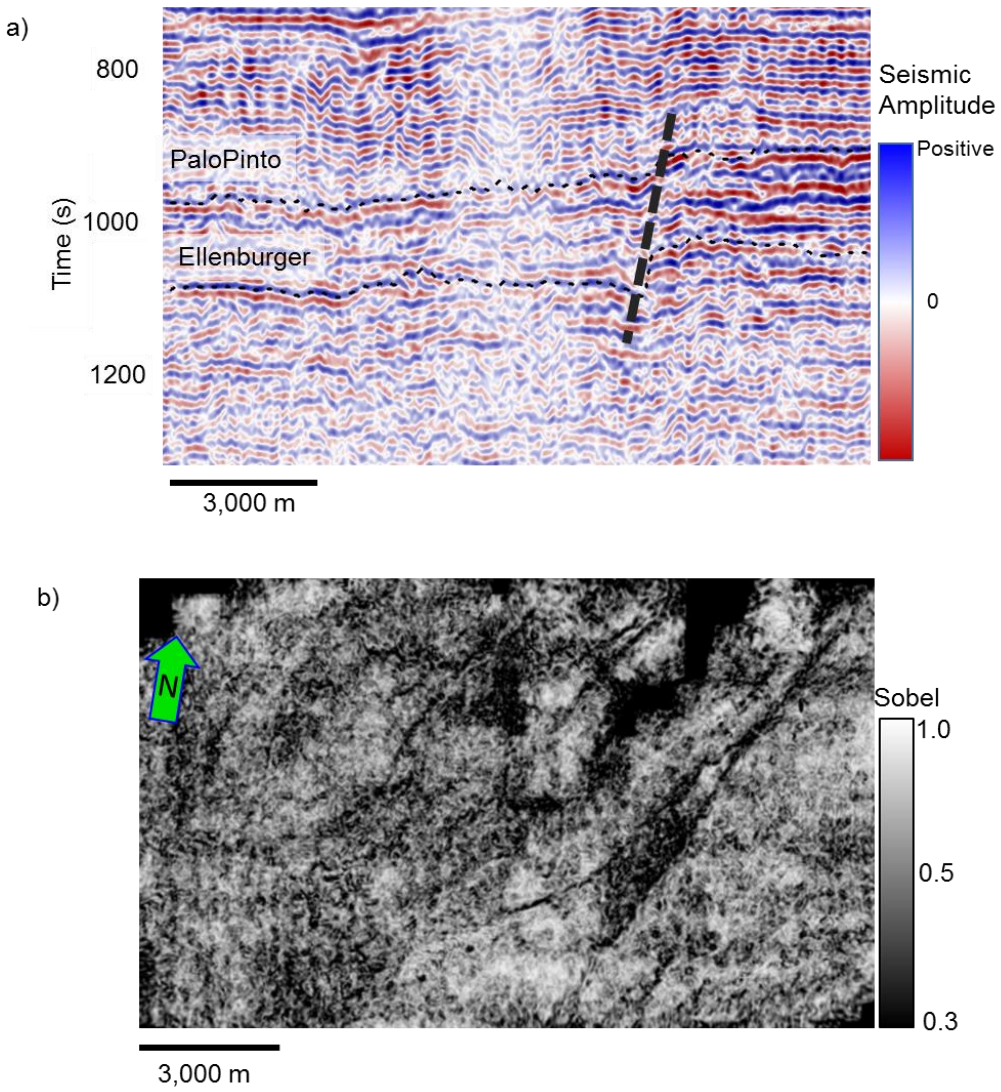

Figure 5.11. After ground roll suppression (a) vertical section of seismic amplitude (b) time slice at t =1.1 sec at the level of Mississippian chert for coherence. Compare this figure with the Figure 1, to see improvements after ground roll suppression.

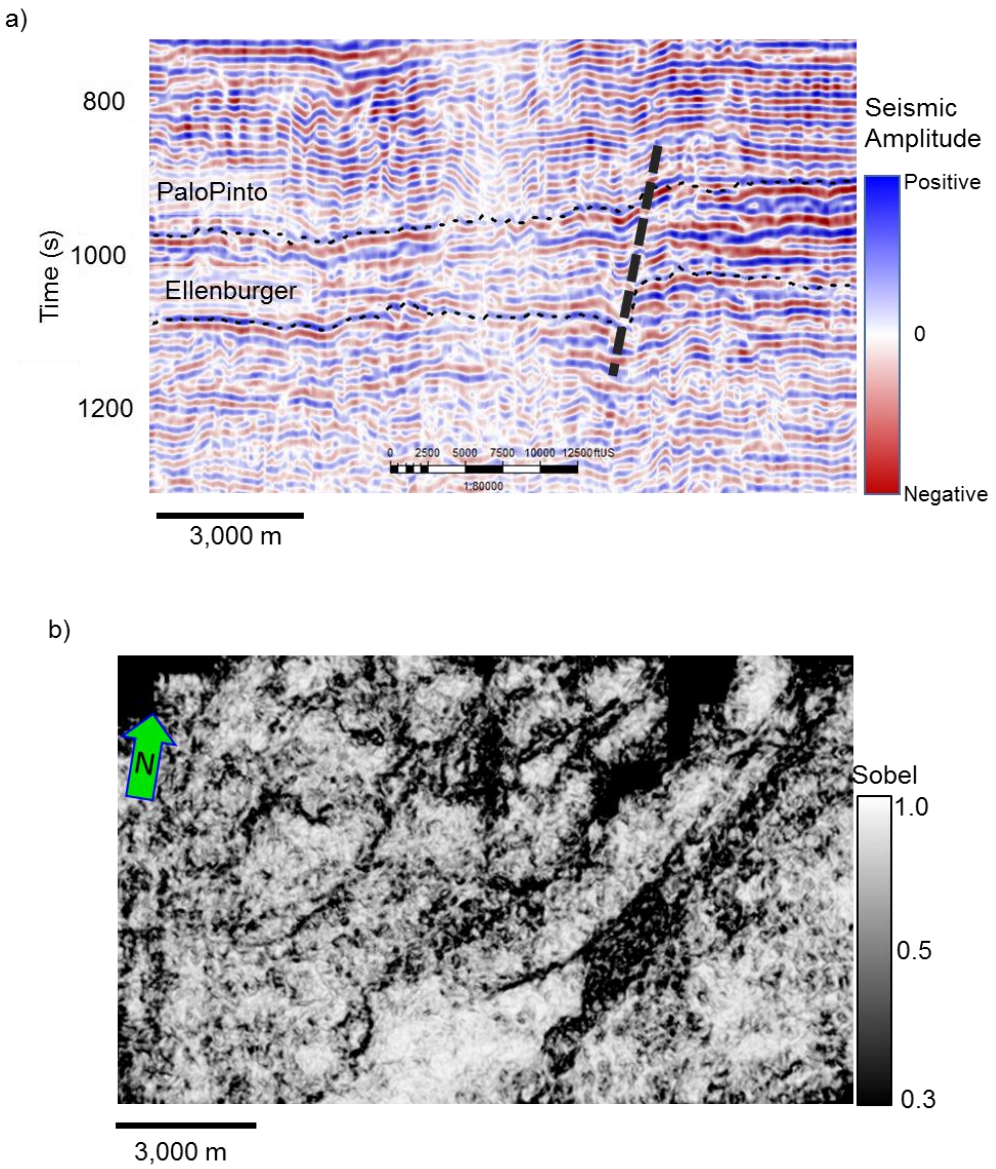

Figure 5.12. After ground roll suppression as well as prestack seismic data conditioning (a) vertical section of seismic amplitude (b) time slice at t =1.1 sec at the level of Mississippian chert for coherence. Compare this figure with the Figure 5.1, to see improvements after ground roll suppression.

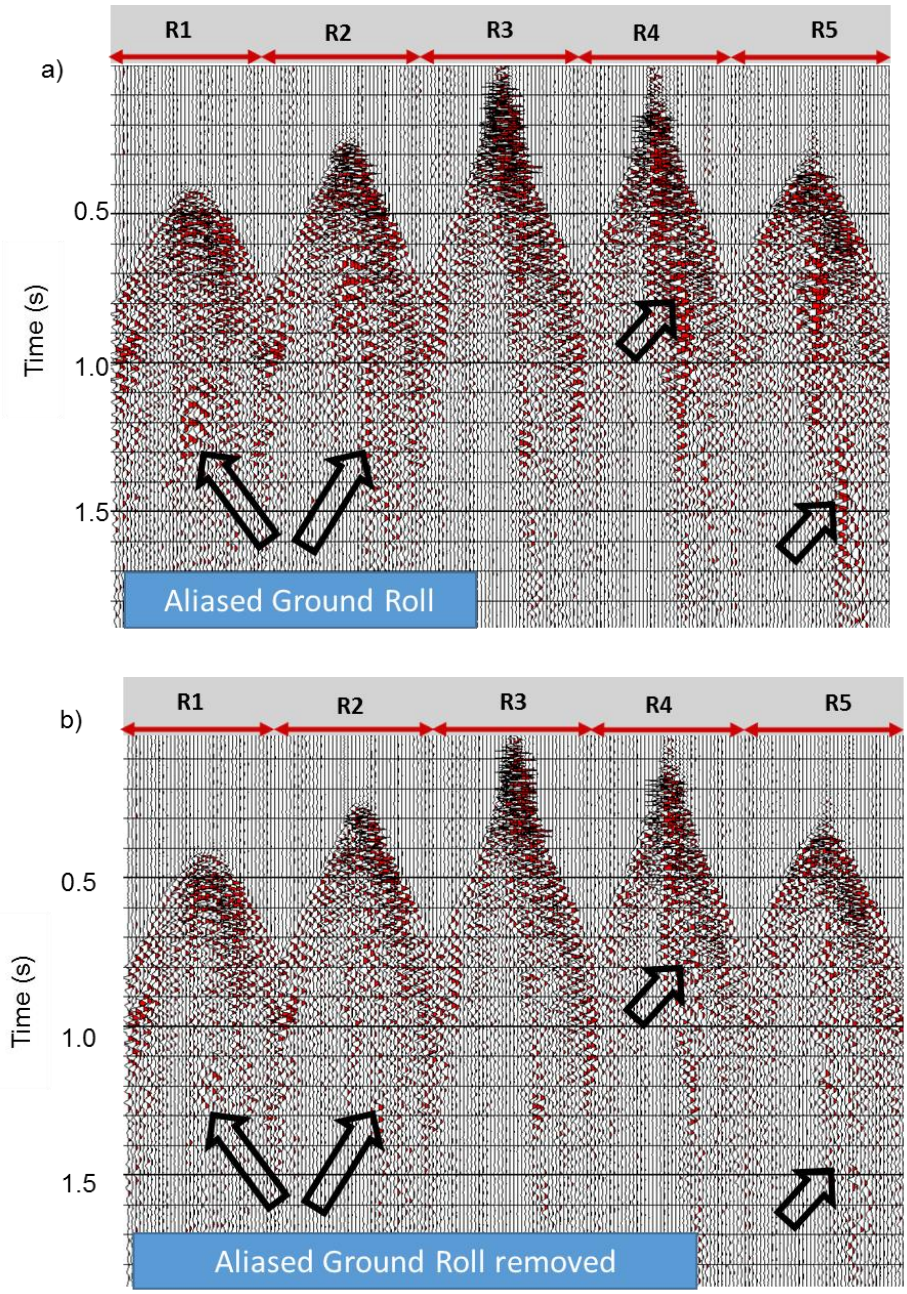

Figure 5.13. A different seismic data set, (a) before ground roll suppression, (b) after ground roll suppression. Notice, the elimination of aliased ground roll and preservation of signal after ground roll removal.

REFERENCES

Aisenberg, M., 2013, The value of reprocessing legacy data: A case study of Bois D'Arc, A Mississippi play in north eastern Oklahoma: MS Thesis , University of Oklahoma.

Brysk, H., and D. McCowan, 1986, A slant-stack procedure for point-source data: Geophysics, **51**, 1370–1386

Chopra, S. and K. J. Marfurt, 2013, Preconditioning seismic data with 5D interpolation for computing geometric attributes: The Leading Edge, **32**, 1456-1460.

D'Agosto, C., K. J. Marfurt, and J. Steven, 2003, Modeling and removal of groundroll from horizontal component of C-waves: 73rd Annual International Meeting, SEG Expanded Abstracts, 1981-1983.

Henley, D. C., 2003, Coherent noise attenuation in the radial trace domain: Geophysics, **68**, 1408-1416.

Done, W. J., 1999, Removal of interference patterns in seismic gathers, in R. L. Kirlin and W. J. Done, eds., Covariance analysis for seismic signal process: SEG, 185–225

Dowdell, Benjamin L., 2013, Prestack seismic analysis of a Mississippi lime resource play in the Midcontinent, U.S.A: MS Thesis, University of Oklahoma.

Embree, P., J. Burg, and M. Backus, 1963, Wide-band velocity filtering – the pie-slice process: Geophysics, **28**, 948–974.

Figueiredo, P., L. Lucena, and G. Araújo, 2009, Filter KL/SVD for groundroll noise attenuation: 11th International Congress of the Brazilian Geophysical Society & EXPOGEF, Salvador, and Bahia, Brazil, Expanded Abstract, 1637-1640.

Foti, S., L. Sambuelli, L. Socco, and C. Strobbia, 2002, Spatial Sampling Issues in FK Analysis of Surface Waves, Symposium on the Application of Geophysics to Engineering and Environmental Problems.

Gaiser, J. E., 1995, 3D prestack f-x coherent noise suppression: 65th Annual International Meeting of the SEG, Expanded Abstracts, 1354-1357.

Galibert, P. Y., L. Duval, and R. Dupont, 2002, Practical aspects of 3D coherent noise filtering using (F-Kx-Ky) or wavelet transform filters: 72nd Annual International Meeting, SEG Expanded Abstracts, 2241-2244.

Höcker, C., and G. C. Fehmers, 2002, Fast structural interpretation with structure-oriented filtering: The Leading Edge, **21**, 238–243.

Kirchheimer, F., 1985, On some further aspects of fan filtering: 55th Annual International Meeting, SEG Expanded Abstracts, 635-638.

Kuwahara, M., K. Hachimura, S. Eiho, and M. Kinoshita, 1976, Digital processing of biomedical images: Plenum Press, 187–203.

Liu, J. and K. J. Marfurt, 2004, 3D high resolution Radon transforms applied to groundroll suppression in orthogonal seismic surveys. : 74th Annual International Meeting, SEG Expanded Abstracts, 2144-2147.

Liu, X., 1999, Groundroll suppression using the Karhunen-Loeve transform: Geophysics, **64**, 564–566.

Marfurt, K. J., 2006, Robust estimates of 3D reflector dip and azimuth: Geophysics, **71**, P29–P40.

Montagne, R., and G. Vasconcelos, 2006, Optimized suppression of coherent noise from seismic data using the Karhunen-Loève transform. Physical Review E, **74**, 16213 (1) - 16213(8).

Mulder, W. A., R. -E. Plessix, and G. C. Fehmers, 2002, Another tube wave filter, based on semblance and correlation: 72nd Annual International Meeting, SEG Expanded Abstracts, 2237-2240.

Russell, B., D. Hampson, and J. Chun, 1990, Noise elimination and the Radon transform, Part 2: The Leading Edge, **9**, 31–37.

Strobbia, C., A. Zarkhidze, R. May, and F. Ibrahim, 2014, Model-based attenuation for scattered dispersive waves: Geophysical Prospecting, **62,** 1365-2478.

Trad, D., T. Ulrych, and M. Sacchi, 2003, Latest views of the sparse Radon transform: Geophysics, **68**, 386–399.

Treitel, S., J. Shanks, and C. Frasier, 1967, Some aspects of fan filtering: Geophysics, **32**, 789–800.

Turner, G. 1990, Aliasing in the tau-p transform and the removal of spatially aliased coherent noise: Geophysics, **55**, 1496–1503.

CHAPTER 6 **: ESTIMATION OF TOC AND BRITTLENESS**

This chapter is written as first person for this dissertation. This paper will later be submitted to 'Interpretation' after some modifications with the following authors:

Sumit Verma, Tao Zhao, Deepak Devegowda, and Kurt J. Marfurt,

[1]The University of Oklahoma, ConocoPhillips School of Geology and Geophysics.

This chapter is based on 3 published abstracts and some recent work.

Verma, S., K. J. Marfurt, A Way of TOC Characterization on Barnett and Woodford Shale: AAPG Annual convention, Search and Discovery Article: 80429.

Verma, S. , A. Roy, R. Perez, K. J. Marfurt, 2012, Mapping high frackability and high TOC zones in the Barnett Shale: Supervised Probabilistic Neural Network vs. unsupervised multi-attribute Kohonen SOM: 82nd Annual International Meeting, SEG Expanded Abstracts.

Zhao, T., S. Verma, and D. Devegowda, 2015, TOC estimation in the Barnett Shale from triple combo logs using support vector machine: 85th Annual International Meeting, SEG Expanded Abstracts.

ABSTRACT

The Barnett Shale in the Fort Worth Basin is one of the most important resource plays in USA. TOC and brittleness can help to characterize a resource play. Higher TOC or organic content are generally associated with rocks with higher clay content, which are ductile in nature. Higher quartz content results in increased brittleness. Brittle rocks are easily fractured, with fracture better held open with proppant. Juxtaposition of brittle-ductile rocks provide permeable pathways for hydrocarbon to reach the well bore.

Cost of core acquisition and petro-physical measurements are very high as compared to wireline logging. I estimate TOC from wireline log using Passey's method and attain a correlation of 64% where errors in the base line interpretation can lead to inaccurate estimates. Using non-linear regression with Passey's TOC, normalized stratigraphic height and acquired wireline logs the correlation was increased to 75%. This regression can be applied to un-cored wells but logged wells to estimate TOC and thereby provide ground truth with in the seismic survey.

Core measurements provides accurate measures of both TOC and mineralogy. Brittleness indices are computed based on mineralogy using Wang and Gale's formula. While the correlation of BI with elastic logs ($\lambda\rho$, $\mu\rho$, V_P/V_S, Z_P and Z_S)and wireline logs is good (78%). That with the triple combo logs falls to only 66 % and form less reliable proxies.

I correlate production to volumetric estimate of TOC and brittleness by computing distance weighted averages about assumed perforations in120 horizontal wells. Correlation of blind well test shows 38% was encouraging suggesting that the geologic component of completion provides an important contribution to well success.

INTRODUCTION

TOC and brittleness are the two most important parameters for resource play characterization. In general, resource plays have low permeability and require hydraulic fracturing of the rock to make them produce economically. Rocks which are brittle (have a high brittleness index) can be fractured more easily than to the rocks which are ductile (have a low brittleness index, Wang and Gale, 2009). In general high TOC is associated with higher clay content; these ductile rocks are more difficult to fracture and more rapidly close about proppant. The sweet spot is often laminated brittle-ductile couplets (Slatt, and Abousleiman, 2011). In such situations the well drilled and completed in the brittle rock which (after fracking) provides high permeable pathways into the associated high TOC rock.

TOC can be measured on core data accurately, and can be estimated on wireline logs using different methods (Sondergeld et al., 2010), with Passey's method (Passey et al., 1990) being one of the most popular methods. Passey's method requires interpreter definition of baseline on porosity and resistivity log. Errors in defining the base lines result in inaccurate TOC estimates.

Several well logs can measure the presence of TOC. High gamma ray response can be correlated to high uranium content in organic matter (Fertl and Chilingar, 1988). Organic matter is less dense than to matrix minerals resulting in a low on bulk density log (Schmoker and Hester, 1983). Transit times recorded on P-sonic log may increase in the presence of organic matter (Passey, 1990; Sondergeld et al., 2010). Neutron logs may provide a high response in the presence of organic matter (Sondergeld et al., 2010).

Organic matter being non- conductive, the resistivity logs read high values for high TOC (Passey, 1990).

Jarvie et al. (2007) defined BI (brittleness index) as a measure of brittleness based on mineralogy. The formula suggests that an increase in percentage of quartz (brittle) or decrease in clay (ductile) or carbonate (ductile) % will increase the brittleness. Wang and Gale (2009) modified the formula by adding TOC and dolomite in to the equation, where the increase in dolomite (brittle) increases BI while an increase in TOC (ductile) decrease BI. Rickman et al. (2008) provided a way to estimate average brittleness with elastic properties Young's modulus and Poisson's ratio. Zhang et al. (2014) derived Young's modulus and Poisson's ratio with pre-stack inversion and were able to estimate volume of brittleness with Rickman's equation. Perez and Marfurt (2014) working on Barnett Shale, created template for brittleness with $\lambda\rho$ and $\mu\rho$ based on the core and well log data, and they then used the template to compute a volume of brittleness from $\lambda\rho$ and $\mu\rho$ 3D volumes. Zhang et al. 2015 derived 10 classes of brittleness on the cored well using a support vector machine using elastic logs (Z_P, Z_S, μ/λ, σ) and Wang and Gale's brittleness index. They then apply these classes to the volumetric estimates of Z_P, Z_S, μ/λ and σ to obtain a brittleness volume.

Brittleness varies with mineralogy and response on the wireline logs change for different mineralogy. So, wireline log can provide an indirect measurement of BI. For example quartz is not radioactive and exhibits low gamma ray response whereas clay which has radioactive minerals produces high gamma ray response. Quartz is a heavier mineral compared to clay on a bulk density log. Limestone often exhibits high resistivity

compared to clay. P-wave velocity is higher in limestone, lower in quartz and lowest in clay.

I begin with an overview of the geology of study area. Next, I describe methodology, where first I show how we can estimate TOC and brittleness from core to well log data, and from well log to 3D volume. Then, I discuss the results of my analysis. I conclude by correlating the volumetric estimates of TOC and BI to first 90 days of production.

GEOLOGY OF THE STUDY AREA

The high TOC Mississippian-age Barnett Shale is an unconventional resource play in Fort Worth Basin (FWB), which is in Texas, USA (Figure 6.1). The FWB is a shallow N-S elongated foreland basin formed at a convergent plate boundary during the late Paleozoic (Walper, 1982). The FWB is bordered by the Ouachita thrust belt, the structural Bend arch and the Precambrian Llano uplift.

The FWB basement is comprised of Precambrian granodiorites and metasediments. In the Cambrian, the Wilberns, Riley and Hickory formations were deposited, followed by the Ellenberger and Viola limestone formations during the Ordovician (Montgomery, 2005). In the study area in the NE FWB, the Viola limestone is partially eroded, with the Barnett Shale deposited on the unconformity. The Barnett Shale sequence is characterized by alternating shallow marine limestones and black organic rich shales. In the area of study, the Barnett Shale is separated into Upper and Lower shale units by the intervening Forestburg Limestone, which thins and disappears to the south-west. The Viola in the area of study is not highly karsted and forms an effective fracture barrier.

METHODOLOGY

The methodology consists of two steps (Figure 6.7). First, I correlate TOC and Brittleness Index (BI) to wireline logs to form a proxy from common triple combo log. TOC was measured with Rock Eval pyrolysis at the two core wells, whereas BI was computed with FTIR mineralogy using the Wang and Gale formula. I will then use this correlation to predict TOC and BI at the 37 logged (but un-cored) wells that fall within the 3D seismic survey. Second, I use the well log predictions at the 37 wells as truth and correlate them to a suite of seismic attributes extracted about the wells. This final correlation will provide a volumetric estimate of TOC and BI at each voxel with in the Lower Barnett Shale.

Most of the production in the Barnett Shale comes from the Lower Barnett Shale in the study area. For my study I used data from two cored wells which are outside of the seismic survey area. I applied a depth shift (bulk shift) ±2ft on the core measurements which increased the correlation of well logs to the core data. Both cores completely sample the Lower Barnett Shale, part of the Forestburg, and the Upper Barnett Shale. Well A lies less than 1 mile to the NE while Well B lies approximately 21 miles in the SW, boundary of the seismic survey (Figure 6.2). There are approximately 50 vertical wells in the survey area containing neutron, density and deep resistivity logs. An additional 40 vertical wells lack these log suites and will not be used. Around 13 wells out of 50 do not have complete log in the Lower Barnett Shale. Finally, for analysis I selected 37 wells which have neutron, density, and deep resistivity logs. Out of these 37 wells few wells have completely or partially missing neutron porosity and P-sonic, I used neutral network method to predict missing well logs. Apart from this there are 261

vertical and 120 horizontal wells with first 90 days of production (but no well logs) are present with in the study area.

CORRELATING CORE TO WIRELINE MEASUREMENTS

TOC estimation using Passey's equation

Passey's (1990) method is also called "Delta log R" method, and it requires a resistivity log along with a porosity log e.g. P-sonic, density or neutron log in order to estimate TOC log:

$$\Delta logR = log_{10}(RTD / RTD\_Base) - 2.5 * (RHOB - RHOB\_base) \quad (1)$$

$$TOC = (\Delta logR * 10^{a}), \quad (2)$$

where,

$$a = 0.297 - 0.1688 * LOM, \text{ and} \quad (3)$$

RTD : deep resistivity in any zone (ohm-m)

RTD_Base : deep resistivity baseline in non-source rock (ohm-m)

RHOB: bulk density (g/cm^3)

RHO_Base : bulk density baseline in non-source rock (g/cm^3)

LOM: Level of Maturity.

The RTD baseline is interpreter dependent. For well A I used, *RTD_base*=5 ohm-m, *RHOB_base* =2.58 g/cm^3 (Figure 6.3). LOM is the level of maturity; a higher value of LOM indicates rock is more mature. LOM has been correlated to vitrinite reflectance (R_O) (Figure 6.4), which also indicates maturity of rock. Figure 6.4 suggests that the *LOM* value falls between 10 and 12. I evaluated several *LOM* values between 10-12 and found TOC computed with *LOM*=11.5 provides the best match with core TOC measurements.

I then used the same values of *RTD_base*, *RHOB_base* and *LOM* for all the wells in the survey area.

Figure 6.5 shows that the TOC computed with Passey's method follows the trend of core measured TOC on both Well A and Well B. Figure 6.6 shows that the TOC correlation (between core measurements and TOC computed with Passey's method) on Well A, for which the base line was chosen, is higher than the well B, which is 30 miles away from the Well A. While these correlations are 64% and 55% respectively, I wish to improve them.

Multilinear regression

Multilinear regression is routinely used to estimate missing logs (Holmes et al. 2003). In this work, I wish to estimate the "missing" TOC log from these that were measured. In addition to density, neutron porosity, gamma ray, deep induction (Deep Resistivity) and P-sonic well logs I used two computed logs, Passey's TOC and normalized stratigraphic height; (Figure 6.9). Kale, 2009 analyzed working on the Well A found an increase in porosity with TOC. Hydrocarbons exhibit higher resistivity than saline water clastic rocks which suggests may be deep resistivity may be sensitive to TOC.

Using a baseline from well A, I computed TOC with Passey's method on about 37 wells with in the seismic survey area. Figure 6.8 shows that the Lower Barnett Shale thickness decreases from North-East (A') to South-West (A). Using gamma ray logs Singh (2008) correlated nine para-sequence sets along AA' in the Lower Barnett Shale. This correlation suggests the use of normalized stratigraphic height, Z_n : $Z_n = (Z_{Viola} - Z) /$

(Z_{Viola} - Z_{LBS}) where, *Z* is depth of a log sample and where , Z_{Viola} and Z_{LBS} are tops of the Viola Limestone and the Lower Barnett Shale in that log.

While forming the multilinear regression, I allow the core measured TOC to be correlated to samples in a window around corresponding depth points of the well logs. Such flexibility compensates for the residual depth mismatch between the core and well log. I compute correlations and errors for different combinations of input logs (up to five) and window sizes from ±0 ft to ±4 ft (Figure 6.9). I use average validation correlation as the search criteria for step wise multilinear regression for including the next best well log in to regression (Hampson et al., 2001). Validation correlation is the correlation computed by including all the wells in regression except the well at which correlation is to be computed. Validation correlation is computed on all the wells one by one and then average of such correlations is computed. I found that window of ±1 ft and four input logs provided an average validation correlation of 70% and a training correlation was 76%. Inclusion of 5^{th} log increased validation error, which indicates overtraining.

Given the multilinear regression between logs and core TOC, I can choose which logs to use in nonlinear neural network. Neural network estimation has shown better results for the wells which are in the proximity of the training wells (personal communication with Mr. Satinder Chopra). I therefore use with well A to train the neural network and obtain a training correlation of 80% and the blind well correlation (on well B) of 73% (Figure 6.10). With this confidence I used the trained neural network to estimate the TOC on the 37 un-cored wells inside the seismic survey.

Brittleness estimation using Wang and Gale equation

Brittleness is a measure to quantify the ability of rock to fracture (Wang and Gale, 2009). Brittleness depends on rock strength, texture, effective stress, temperature, lithology, fluid type diagenesis, and TOC. Jarvie et al. (2007) defined the brittleness index (BI) based on mineralogy. Wang and Gale (2009) modified their equation by including TOC and subdividing the carbonates into dolomite and limestone:

$$BI = \frac{Q+Dol}{Q+Dol+Lm+Cl+TOC}, \qquad (4)$$

where , *BI: Brittleness Index,*

Q = Quartz,

Dol=Dolomite,

LM = Limestone,

Cl = Clay and

TOC=Total Organic Carbon.

Figure 6.12 shows the computed BI on the two cored wells. Wang and Gale formula includes TOC in the denominator, which indicates BI is modified by TOC. It appears that increase in TOC would decrease BI significantly. But, in reality TOC does not have such huge effect on BI because the TOC weight % in general is less than 5%,s such that the effect of TOC on brittleness index is not significant.

Correlation to wireline logs

I use the workflow similar to the previous TOC estimation, to estimate BI logs on the wells inside the seismic survey area. In stepwise multilinear regression, the neutron log has the highest correlation with the brittleness index (Table 6.2):

$$BI=0.0477*NPHI^2-0.186*Density^2+2.7X10^{-8}RTD^2+1.74, \quad (5)$$

where,

NPHI: Neutron Porosity (Fraction), and

RTD: Deep Resistivity.

The multilinear training produces a correlation of 66% with ±2ft window length and three input well logs. I use a list of the best attributes obtained by the multilinear regression in the neural network training. I trained the network with well A, and obtained a training correlation of 68% and a blind well (well B) correlation of 63% (Figure 6.15). Given this validation, I used the trained neural network to compute brittleness index on the wells inside the seismic survey area.

VOLUMETRIC ESTIMATION OF TOC AND BRITTLENESS

The area of study is located in in Fort Worth basin, which has approximately 30 mi^2 of 3D seismic data (Figure 6.2) and 37 wells with estimated TOC and Brittleness Index (Figure 6.16). A total of 30 wells with TOC (and BI) logs were chosen for the training part of the analysis. I used a commercial software package which predicts reservoir properties using seismic attributes and well log data. In order to minimize spurious correlations (Kalkomey, 1997) I limited myself to attributes that are directly correlated to either lithology (acoustic impedance, shear impedance, V_P/V_S and Lambda-Rho and Mu-Rho – computed by Perez, 2013) or stratigraphic stacking patterns (spectral magnitude components from 10-90 Hz at 10 Hz intervals, total energy). Similar to well log prediction of TOC, I computed normalized stratigraphic height volume, with equation, T_n : $T_n = (T_{Viola}–T) / (T_{Viola} - T_{LBS})$ where, T is time of seismic sample and, T_{Viola}

and T_{LBS} are tops of the Viola Limestone and the Lower Barnett Shale surface in that seismic trace.

The process can be divided into three steps (Figure 6.17). First, I need to define the attributes used and the vertical zone of influence (defined as a convolutional operator) in which the well logs are correlated to seismic attributes. The best attributes and operator length result in the minimum validation error. Extending the operator length is equivalent to adding attributes at adjacent stratal slices to the stepwise linear regression workflow, increasing the chances for Kalkomey's (1997) false positive correlations. Since our peak frequency is about 50 Hz, I limited the window lengths to be less than ±20 ms.

Volumetric TOC estimation

Using multilinear regression, I found that an operator length of ± 8 ms with 4 attributes provided the maximum correlation (Table 6.3) for TOC estimation. The training correlation was 84% and the average training error was 0.58 % (Figure 6.18).

Given this suite of attributes and operator length, the second step is to relax the linear relationship obtained with multi linear regression to allow a non-linear relationship using a probabilistic neural network using Gaussian weighting functions. PNN training correlation was 87% and the average validation correlation was 75% with the average validation error of 0.54. In the third and final step, the trained network is applied to generate a 3D volume of TOC.

Volumetric Brittleness estimation

Perez (2013) used LambdaRho and MuRho to estimate BI. Rickman et al. (2008) proposed a BI formula based on Young's Modulus and Poisson's Ratio. This motivated me to include Young's Modulus, Poisson's Ratio, LambdaRho and MuRho volume as input volumes. I keep all the input attributes used in TOC estimation. With multilinear regression analysis, I found the best correlation and least validation error with a window of ± 12 ms and five attribute provided (Table 6.4) for BI estimation. I do neural network training with the best attributed indicated by multilinear regression. The training correlation was 67% and the average error was 0.054 (Figure 6.20).

Correlation of TOC and BI to Relative EUR: AASPI proto type Cigar Probe

Hydrocarbon production in the Barnett Shale is a function of both geology and completion. The completion techniques used in this surveys changed with time, but most of the wells were less than one mile long with two to four stages. In this work I assume that production varies linearly with the number of stages and the length of the well with this simplification, I then wish to correlate the first 90 days of production to the volumetric estimate of TOC and BI. Barnett production has been empirically related to length of the well, number of stages, brittleness of the rock, TOC of the rock, layering of the rock (Brittle/Ductile couplets, Slatt and Abousleiman, 2011), natural fractures or zones of weakness (sometimes positively, but in core area of FWB, usually negatively, Trumbo, 2010). Relative production ranges between 0 to 10, 10 being the best production well and 0 being no production for 120 horizontal wells within the seismic survey. I use the trajectory of the horizontal wells, and assume that all the points of the well are

perforated. Microseismic data (Perez, 2013) confirm that production comes only from targeted Lower Barnett Shale (LBS) fracture barriers provided by Forestburg lime (top) and Viola lime at the (base).

Higher TOC indicates higher amount of oil/gas present such that higher TOC can increase the production. Brittle-ductile couplet are important for better production (Slatt and Abousleiman, 2011). Trumbo (2010) found a correlation between the curvature and micro-seismic events; most of the micro-seismic events occur in the negative curvature or bowl shaped features (Figure 6.22). In this survey the ridges are fractured but cemented, forming fracture barriers.

Underlying physics suggests that, fluid flow from a voxel of high TOC to the well perforation location decays as $1/R^2$, where R is the Euclidean distance from any point to the well. Similarly, hydraulic pressure, P, from a perforation location to a voxel of brittle rock decays as $1/R^2$; pressure defines the deviatoric stresses, σ_1-P, σ_3-P. For this reason, I integrate the Green function's response at each element along the well to each voxel weighting attributes TOC, BI, k_1 by $1/R^2$.

In order to correlate the production data of horizontal wells with BI and TOC, I used internal AASPI program "cigar probe" (Figure 6.23). In cigar-probe an average value of the attribute is computed around the well bore path; a sphere of influence with radius R is constructed at each point of on the well path, and then theses spheres are integrated which ultimately gives a $1/R^2$ weighted average property. The output of the cigar probe is one value for per well, with an assumption that the each point on the well bore path in the horizontal section is contributing equally. This is similar to the availability of relative EUR values. I choose a radius of 1,000 ft influence to compute the

BI and TOC. For this analysis I used 120 horizontal wells which were completely inside the survey area.

Limitations of TOC and BI correlation with Production using cigar probe

Rocks fracture nonlinearly (when the deviatoric stress exceeds that defined by Mohr's circle) and natural fractures in brittle rock occur only after a given threshold (Staples, 2011). For this reason, simple weighted averages are not appropriate, but rather some weighted average of that volume of rock that exceeds a critical brittleness, or a specific percentile of a given rock property (weighted medians and weighted percentiles).

RESULTS

TOC computed on the well logs with Passey's equation on well A has a 64% correlation; using the same base lines and LOM values the well B has a lower correlation (55%). The maturity map of Barnett Shale (Figure 6.4a) shale indicates that the rock maturity changes at with different parts of the Fort Worth basin. One should find LOM values, based on the core vitrinite reflectance. Non-linear regression increases the training correlation to 80% and validation correlation to 73%. The use of Passey's derived TOC as well as normalized stratigraphic height provides significant improvement in the correlation.

I use Wang and Gale's (2007) formula to estimate brittleness index (BI). Similar to TOC from core to well log, I use non-linear regression to estimate BI logs on the wells. BI computed with mineralogy, and estimated BI with the multilinear regression had a

correlation of 66%, and with neural network estimated BI with 68% of training correlation. The blind well correlation on well B was 63% for the neural network.

I followed my previous work in which I estimated gamma ray volume (Verma et al. 2012), for computing TOC and BI volumes in Lower Barnett Shale. The multlinear regression analysis suggests that Lambda-Rho has the highest contribution in the regression relation. Use of neural network increases the correlation to 87 % from 84%. I also compared the results on the wells, which were not a part of regression analysis and observed a blind well correlation of 70% (Figure 6.19).

Neural network analysis for the BI has 67% correlation and validation correlation 43%, which is lower than the TOC correlation. This could be because the seismic impedances as well as well log properties are only indirectly related to mineralogy. The estimated BI volume shows a good correlation with the training wells and a decreased, but acceptable correlation to the blind wells (Figure 6.21).

BI estimation with the Wang and Gale formula suggests that BI would decrease with an increase in TOC. Examining cross-plots on well A (Figure 6.13), I observe a decrease in BI with an increase in TOC in deeper part of Lower Barnett Shale. We may conclude that BI is decreasing because of TOC %, but as we know that TOC % is significantly small around 2-6%, so TOC cannot change BI significantly. For a complete picture one should observe cross-plot of clay with TOC. Clay content increases with an increase in TOC, actual numbers of clay % change is very high compared to TOC % change. BI values will change significantly with variation in clay %.

Crossplot between the TOC and production as well as BI and prodcution shows poor correlation (Figure 6.24). I have used weighted $1/R^2$ mean in order to computed

average property. A future research is suggested to using medians and weighted percentiles may provide improved correlation. Prediction of production (relative EUR) with TOC and BI using neural network training shows, a correlation of 38% correlation on validation wells. This correlation can be improved by use of other attributes (such as curvature) known to plan an influence on completion.

DISSCUSSION AND CONCLUSIONS

For the Barnett Shale of the Fort Worth Basin in the study area, nonlinear regression prediction of TOC provides a better estimate of TOC compared to the estimate obtained using Passey's method on the well log. BI estimated on the well logs with non-linear regression has a good correlation with the core computed BI. Core measured TOC observed the highest correlation with Passey's TOC as a single well log, indicating that Passey's method can be used when there is no core available in the study area given a reasonable value of level of maturity and baseline. Inclusion of normalized stratigraphic height in the non-linear regression increases the TOC correlation significantly.

The Wang and Gale brittleness equation indicates an inverse relationship between BI and TOC, which also matches our observation in the lower part of the deeper part of Lower Barnett Shale. Since the TOC % is very small compared to total rock volume, it does make a change a significant change in BI. In general TOC occurs with clay minerals. The change in clay % can be considerably large number and it can cause a significant decrease in BI.Estimated TOC and Brittleness shows a good correlation with the blind well. Estimated BI and TOC volumes can be used to find the brittle ductile couplets as a sweet spot for drilling.

FIGURES AND TABLES

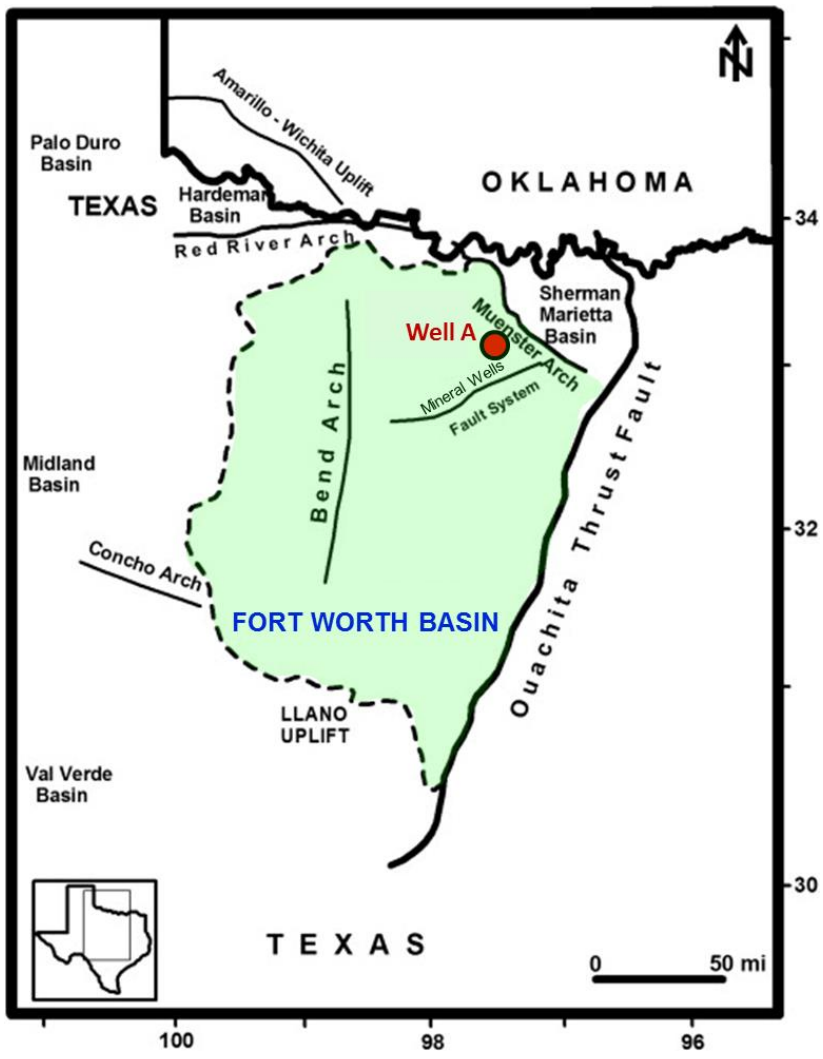

Figure 6.1. Areal extent of the Mississippian Barnett Shale, Fort Worth Basin, Texas (Aydemir, 2011). The red circle indicates the approximate location of cored well A, used in this study.

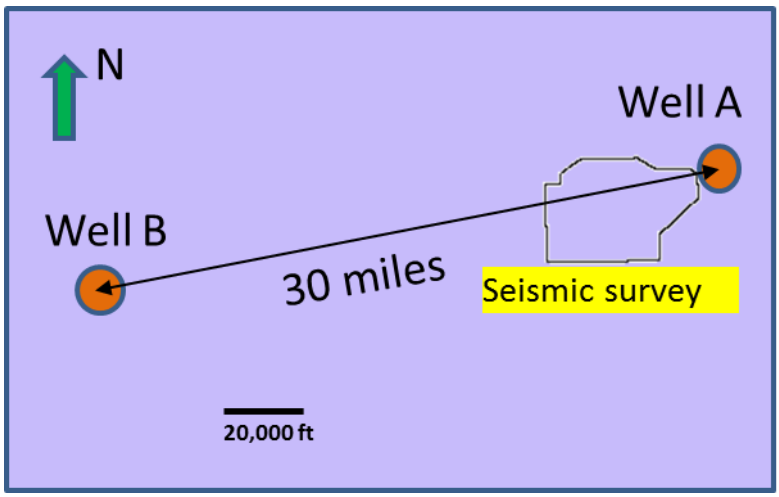

Figure 6.2. Location of cored wells A and B with respect to the seismic survey.

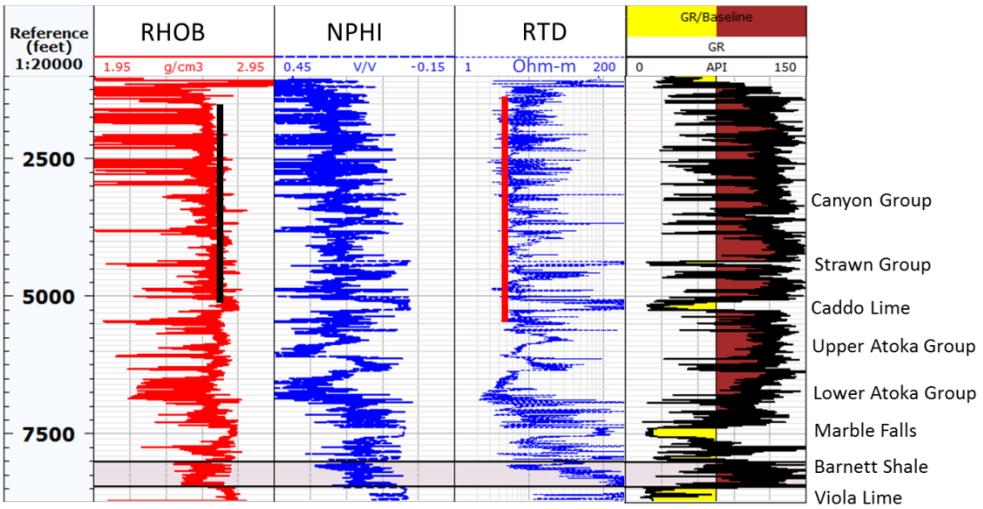

Figure 6.3. Interpretation of baseline for Density and ILD on Well A. The ideal baseline would be a shale/silt stone with zero total organic carbon. Black solid straight line on bulk density (RHOB) curve indicates RHOB_base and red solid straight line on ILD (deep resistivity) curve indicates RTD_Base.

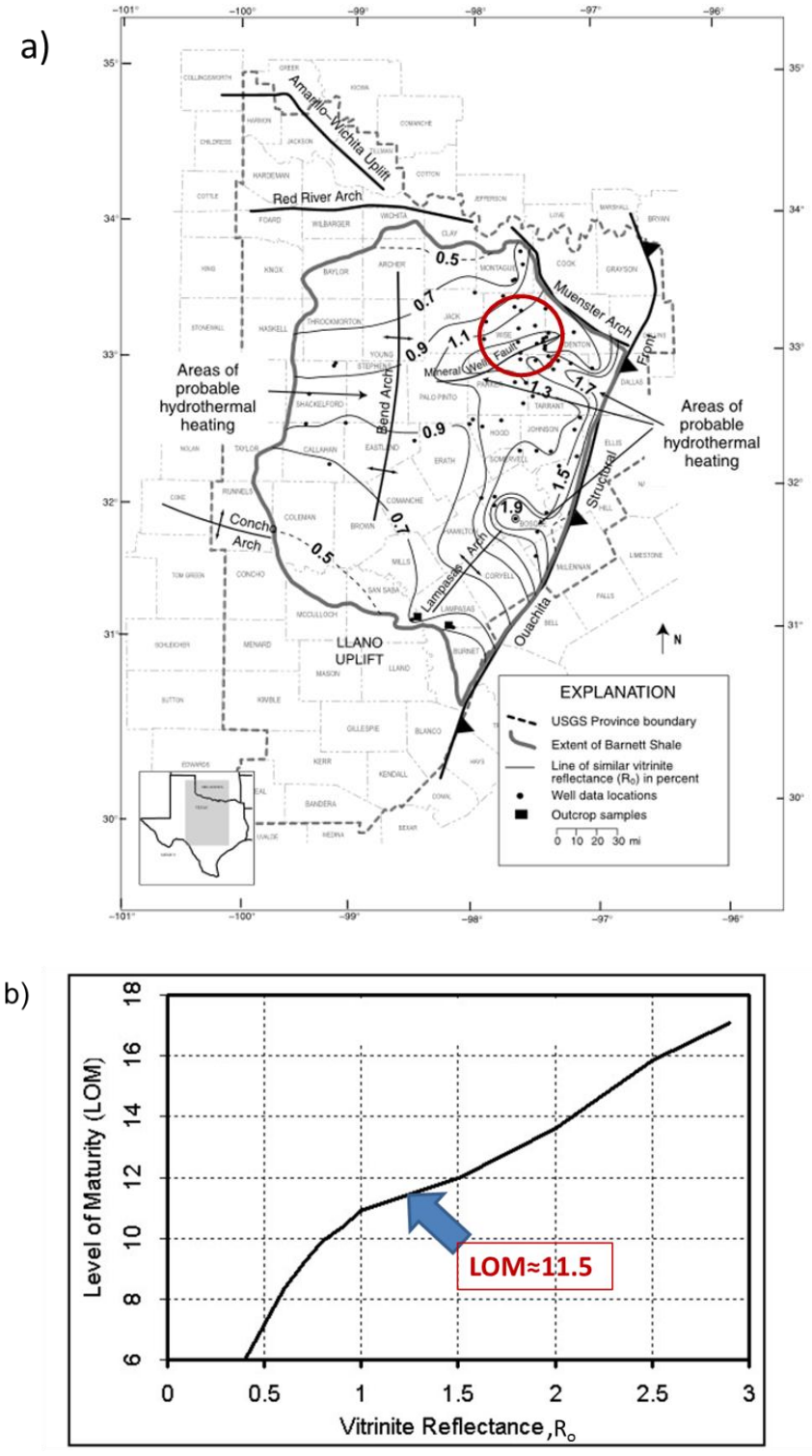

Figure 6.4. (a) Mean vitrinite reflectance (R_o) map of Barnette Shale (Pollastro, 2007). Red circle indicates the approximate location of study area. (b) Vitrinite reflectance (R_o) vs Level of Maturity (based on Crain's Petrophysical Handbook, 2015).

a)

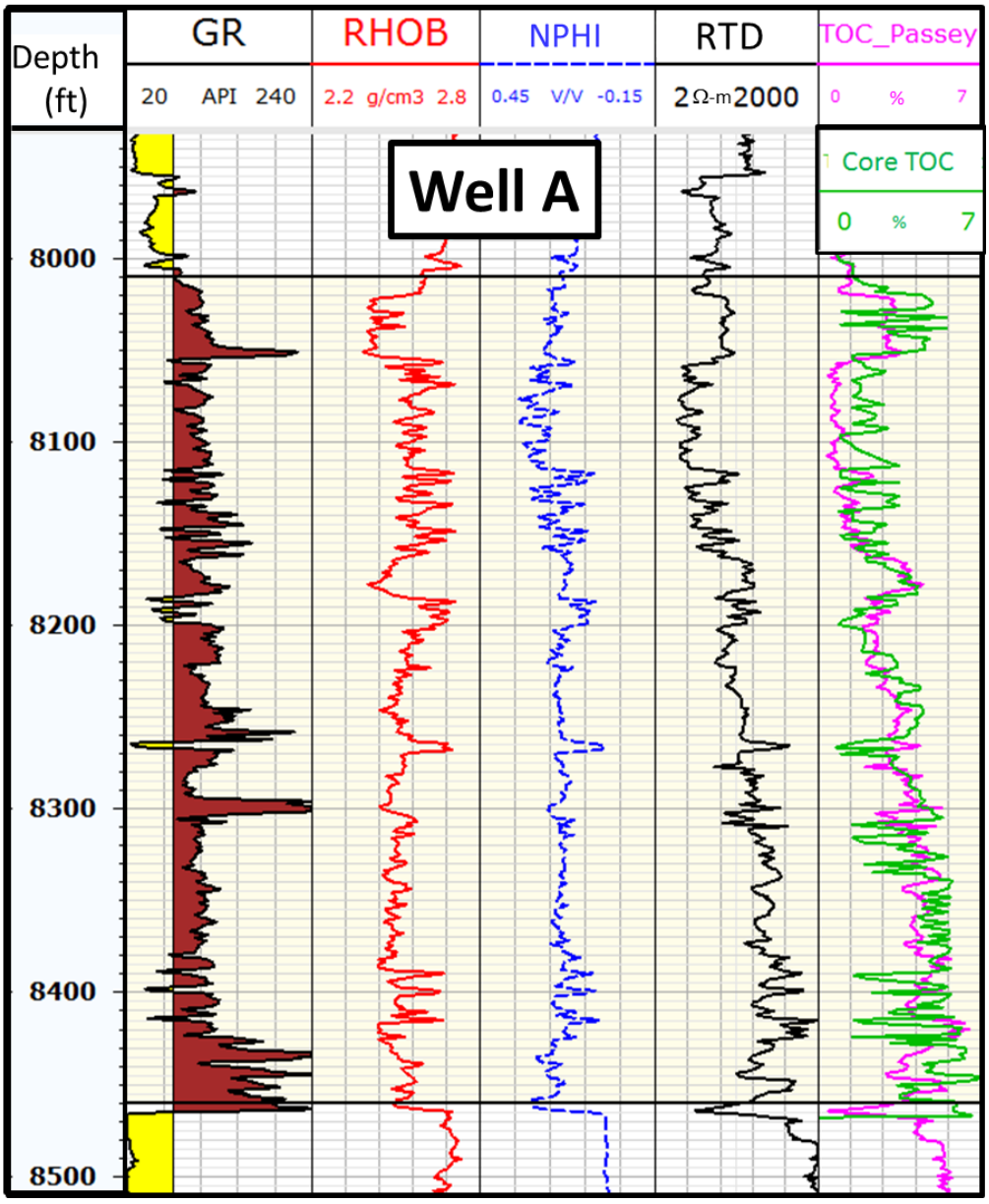
Depth (ft)
GR
20 API 240
RHOB
2.2 g/cm3 2.8
NPHI
0.45 V/V -0.15
RTD
2 Ω-m 2000
TOC_Passey
0 % 7
Core TOC
0 % 7
Well A
8000
8100
8200
8300
8400
8500

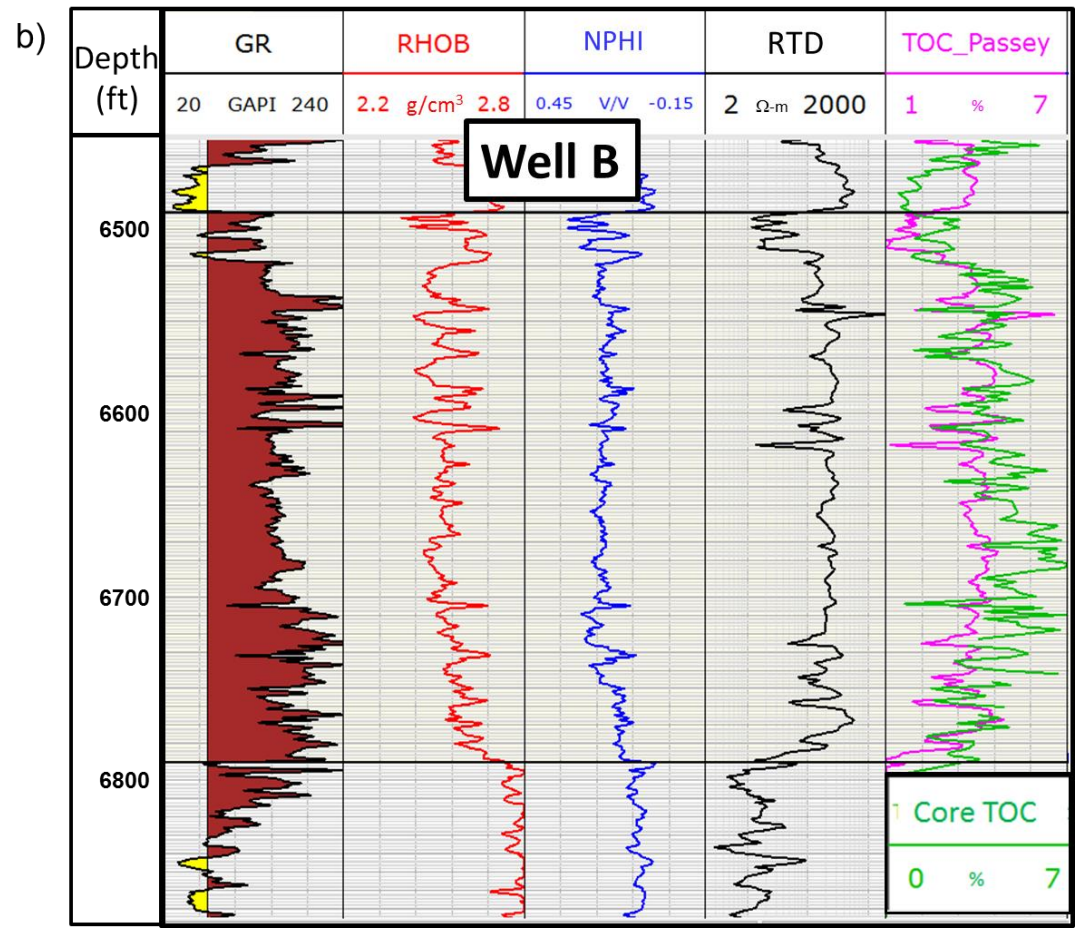

Figure 6.5. Gamma ray(GR), bulk density(RHOB), neutron porosity (NPHI), deep resistivity (RTD) and core TOC (in green) and TOC computed with Passey's (1990) method (TOC_Passey, in pink) on (a) well A (on which we define the baseline), and (b) well B.

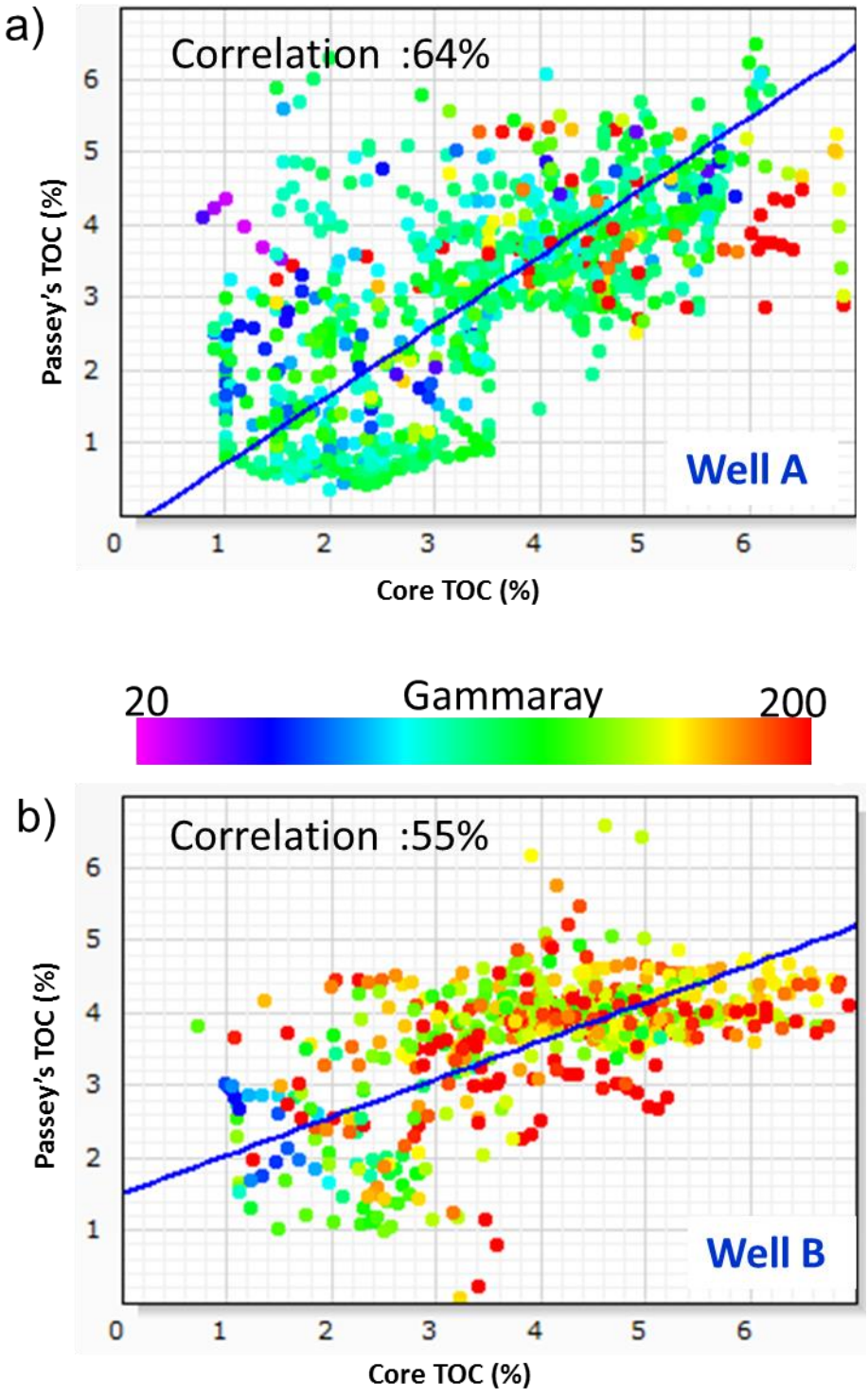

Figure 6.6. Crossplot between core measured TOC and ROC computed with Passeys's method (a) well A on which I define the baseline, and (b) other cored well B.

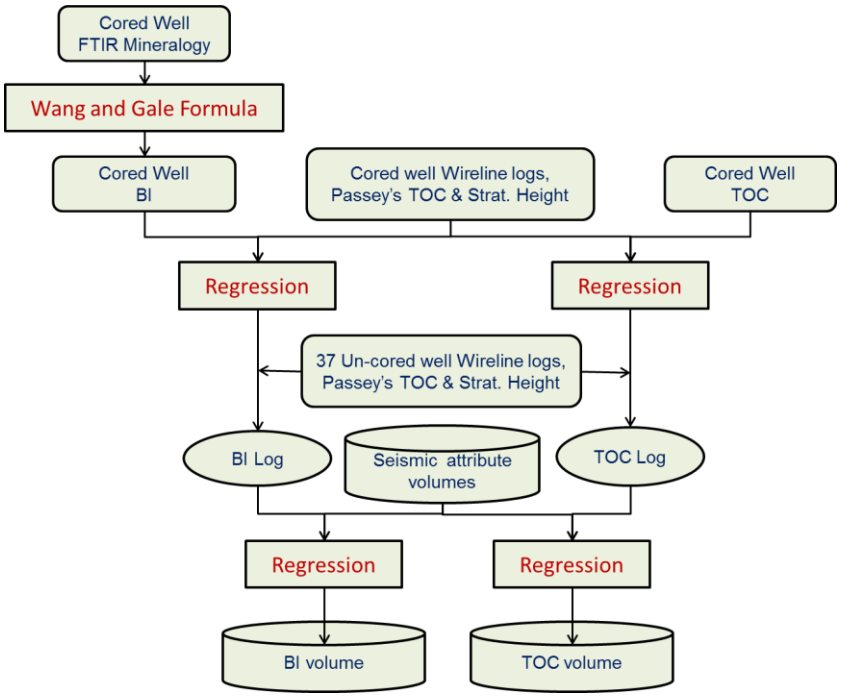

Figure 6.7. Work flow for creation of BI and TOC volumes.

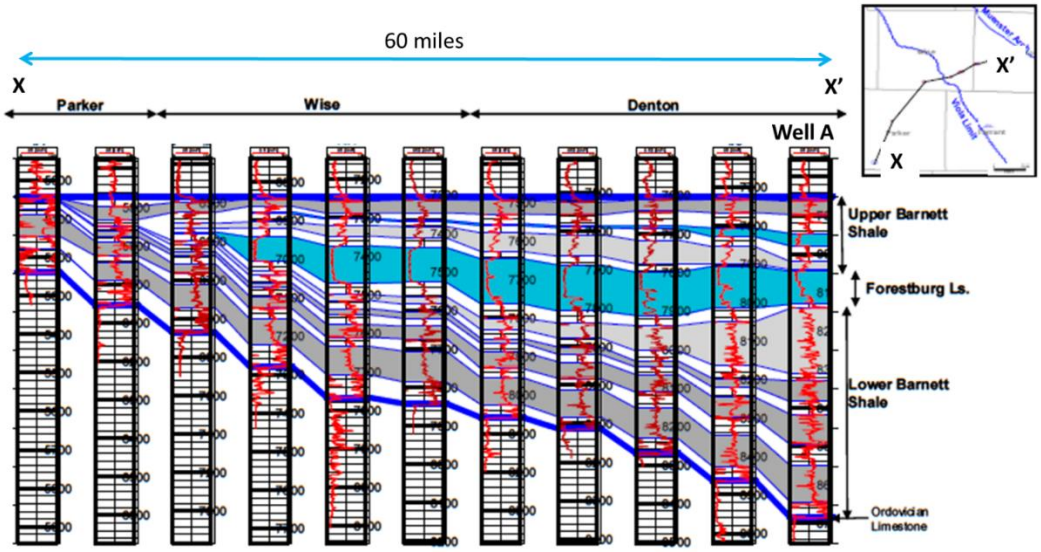

Figure 6.8. Cross section AA' showing subsurface stratigraphic correlation using gamma ray log (Singh, 2008).

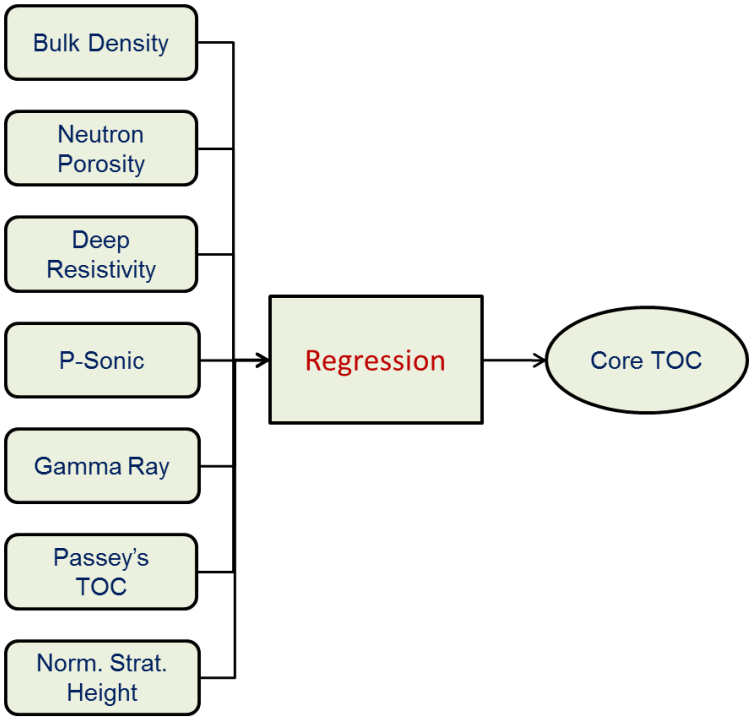

Figure 6.9. Multilinear regression and input and output.

With +/- 1ft weighted window

Well Log	Training Error	Valid Error	Correlation %
Passey's TOC	1.09	1.12	60
Neutron Porosity	0.96	0.97	70
Deep Induction	0.94	0.96	74
Normalized Height	0.92	0.95	76
Density	0.91	0.95	76
Gamma Ray	0.91	0.95	77
P-Sonic	0.91	0.95	77

Table 6.1 TOC estimated with window of ±1ft has least validation error and highest correlation with 4 well logs.

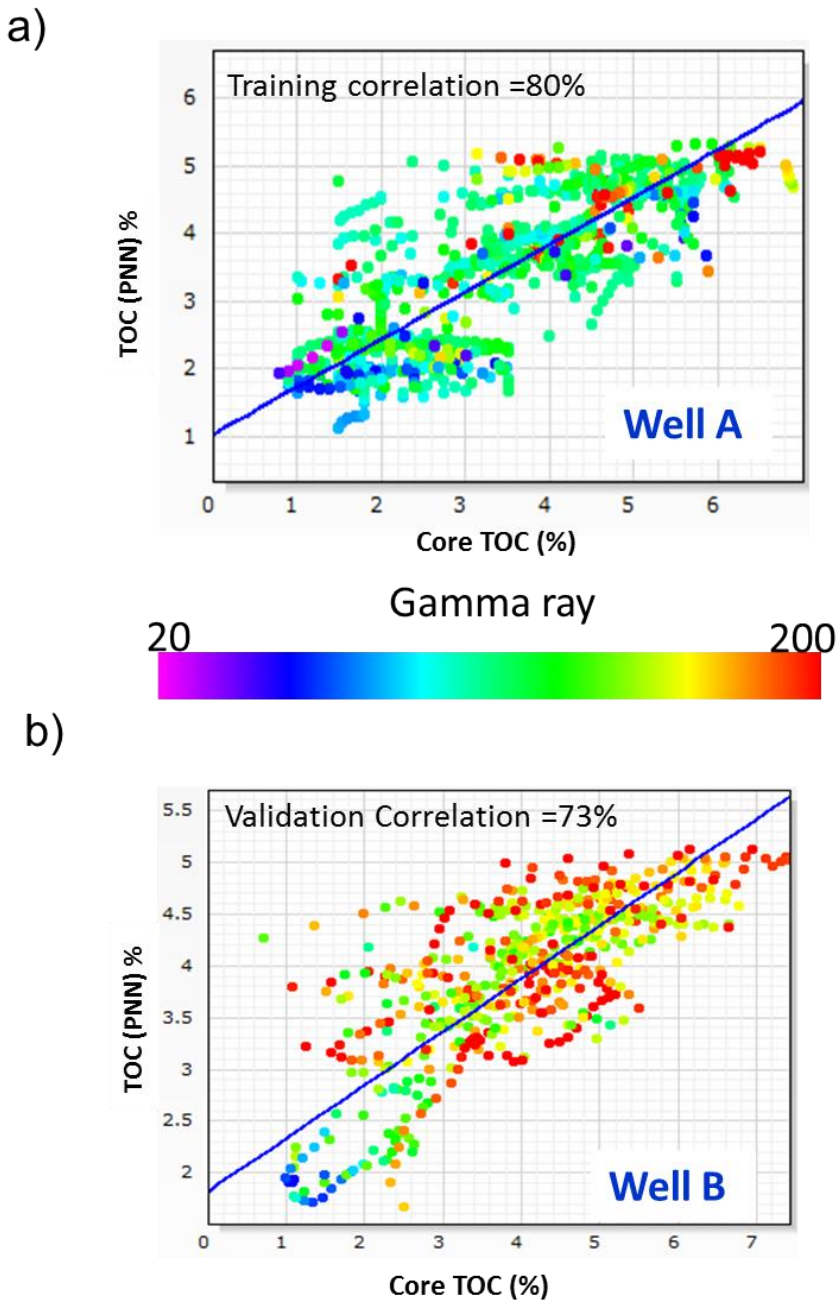

Figure 6.10. Cross plot between core measured TOC and neural network estimated TOC, (a) well A which was used to train the neural network, and (b) other cored well B.

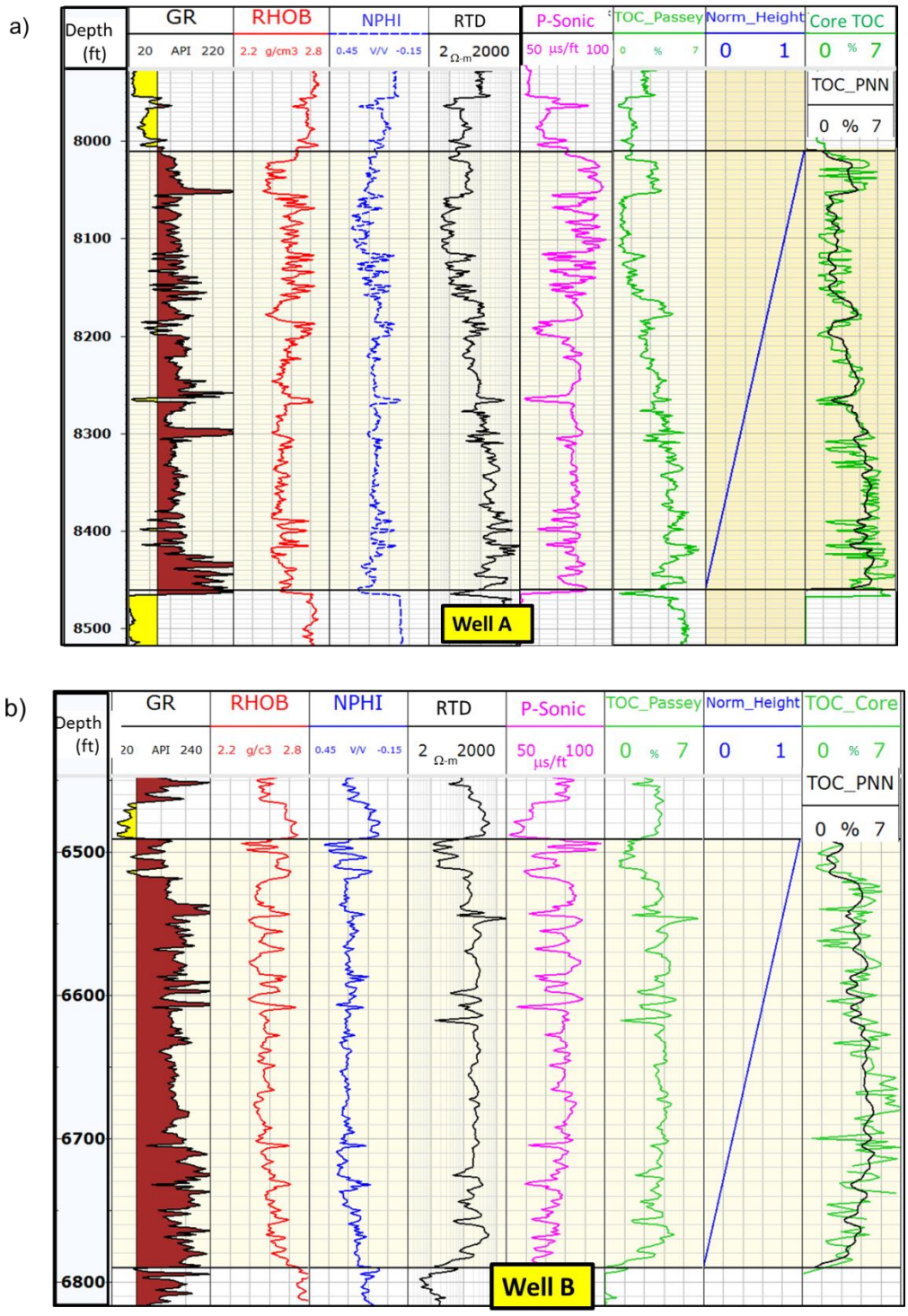

Figure 6.11. Gamma ray (GR), bulk density(RHOB), neutron porosity(NPHI), deep resistivity(RTD), P-Sonic, TOC estimated with Passey's method (TOC_Passey), normalized stratigraphic height, core measured TOC (in green) and neural network estimated TOC (TOC_PNN, in black) at (a) training well A, and (b) validation well B.

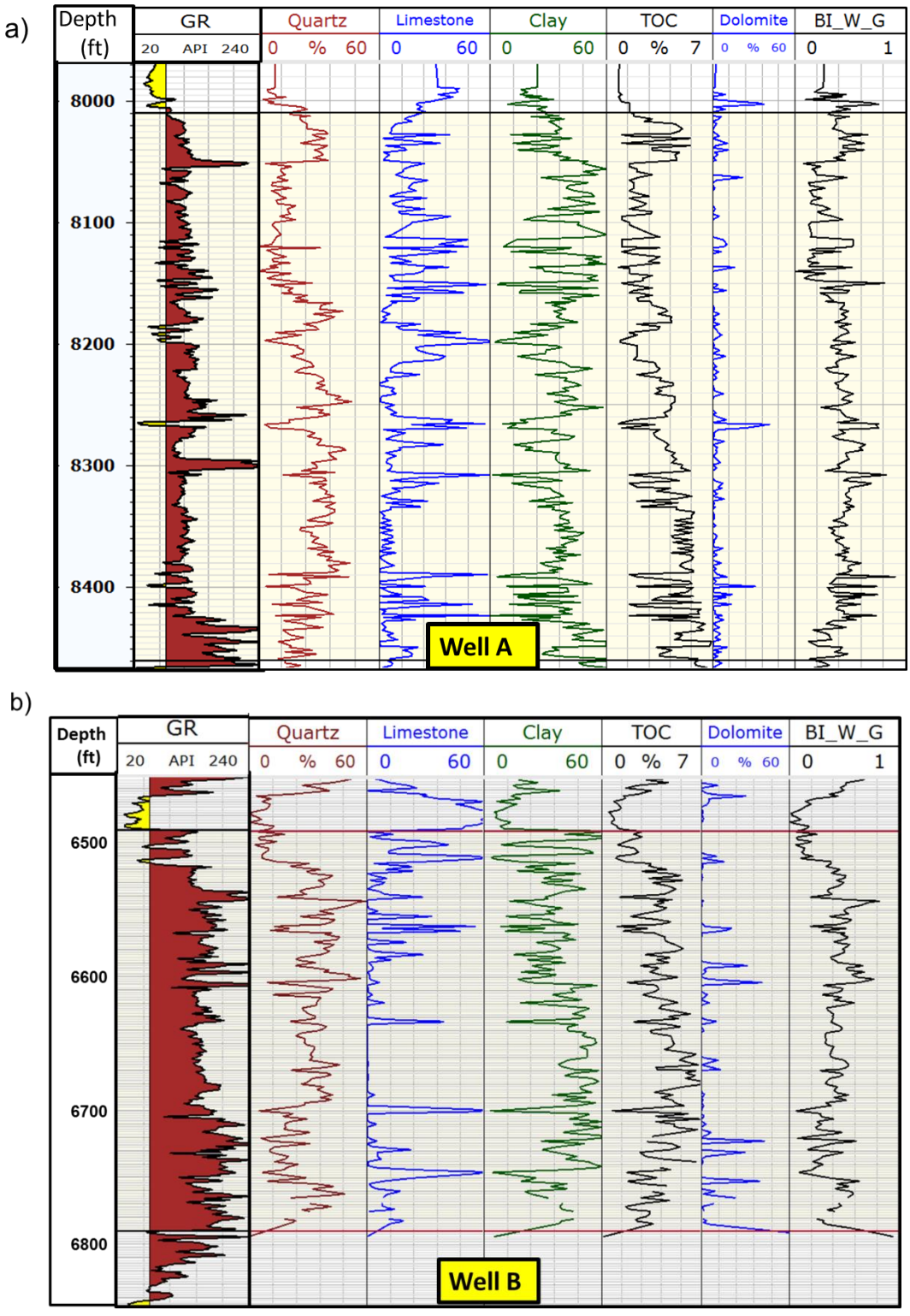

Figure 6.12. Gamma ray well log and core measured mineralogy, quartz, total limestone, total clay, dolomite along with core measured TOC and brittleness index computed with Wang and Gale (2009) formula, on cored wells (a) well A, and (b) well B.

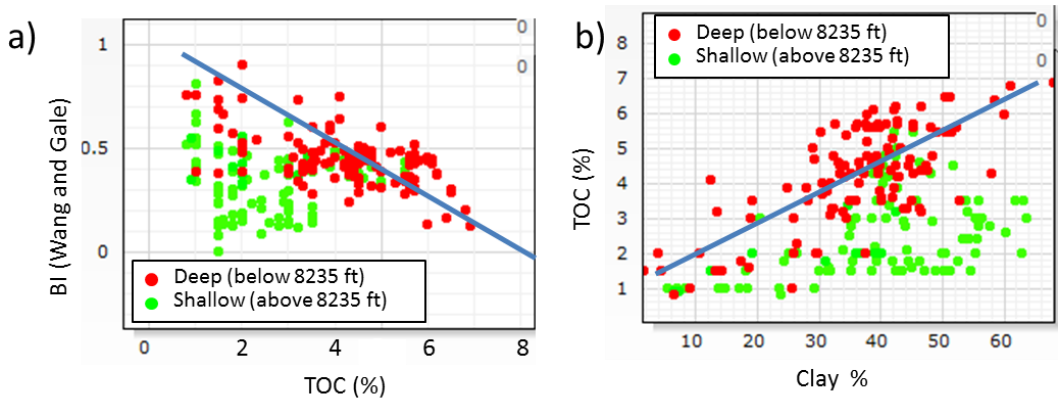

Figure 6.13. Cross plot of cored well A in lower Barnett Shale; (a) Core measured TOC vs Wang and Gale BI with FTIR mineralogy, (b) FTIR measured total clay % vs core measured TOC. BI and TOC has an inverse trend in deeper part of Lower Barnett Shale, as well as TOC increases with clay.

With +/- 2ft weighted window

Well Log	Training Error	Valid. Error	Correlation %
Neutron Porosity	0.110	0.120	46
Density	0.094	0.105	64
Induction Deep	0.092	0.101	66
Normalized Height	0.092	0.105	67
P-sonic	0.092	0.108	67
ANN TOC	0.091	0.109	68

Table 6.2. BI estimated with window of ±2ft has least validation error and highest correlation with 4 well logs.

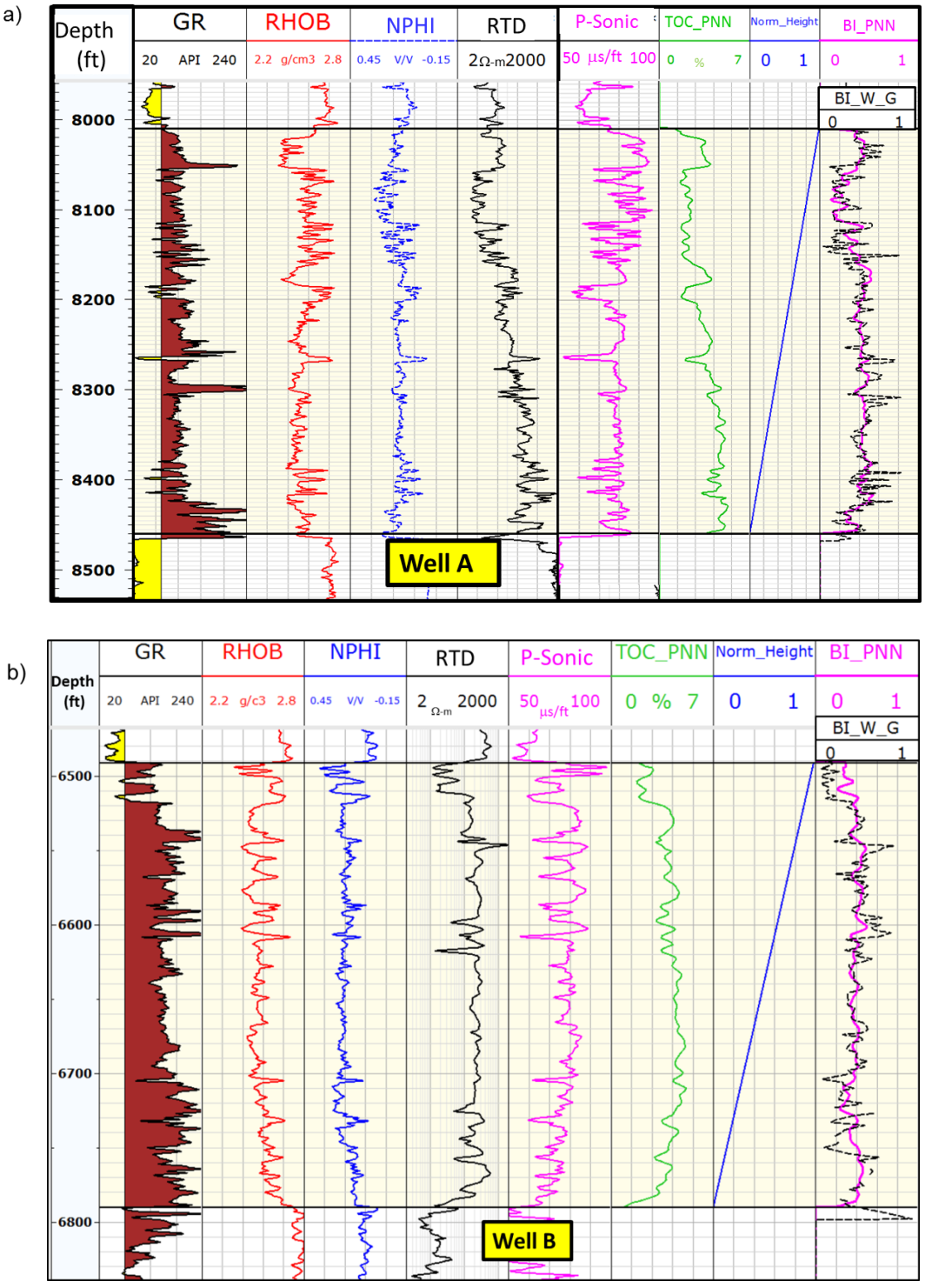

Figure 6.14. Gamma ray (GR), bulk density, neutron porosity (NPHI), deep resistivity (RTD), P-Sonic, neural network estimated TOC (TOC_PNN), normalized stratigraphic height, Wang and Gale computed BI (BI_W_G, in black) and neural network estimated BI (BI_PNN, in pink) at (a) training well A, and (b) validation well B.

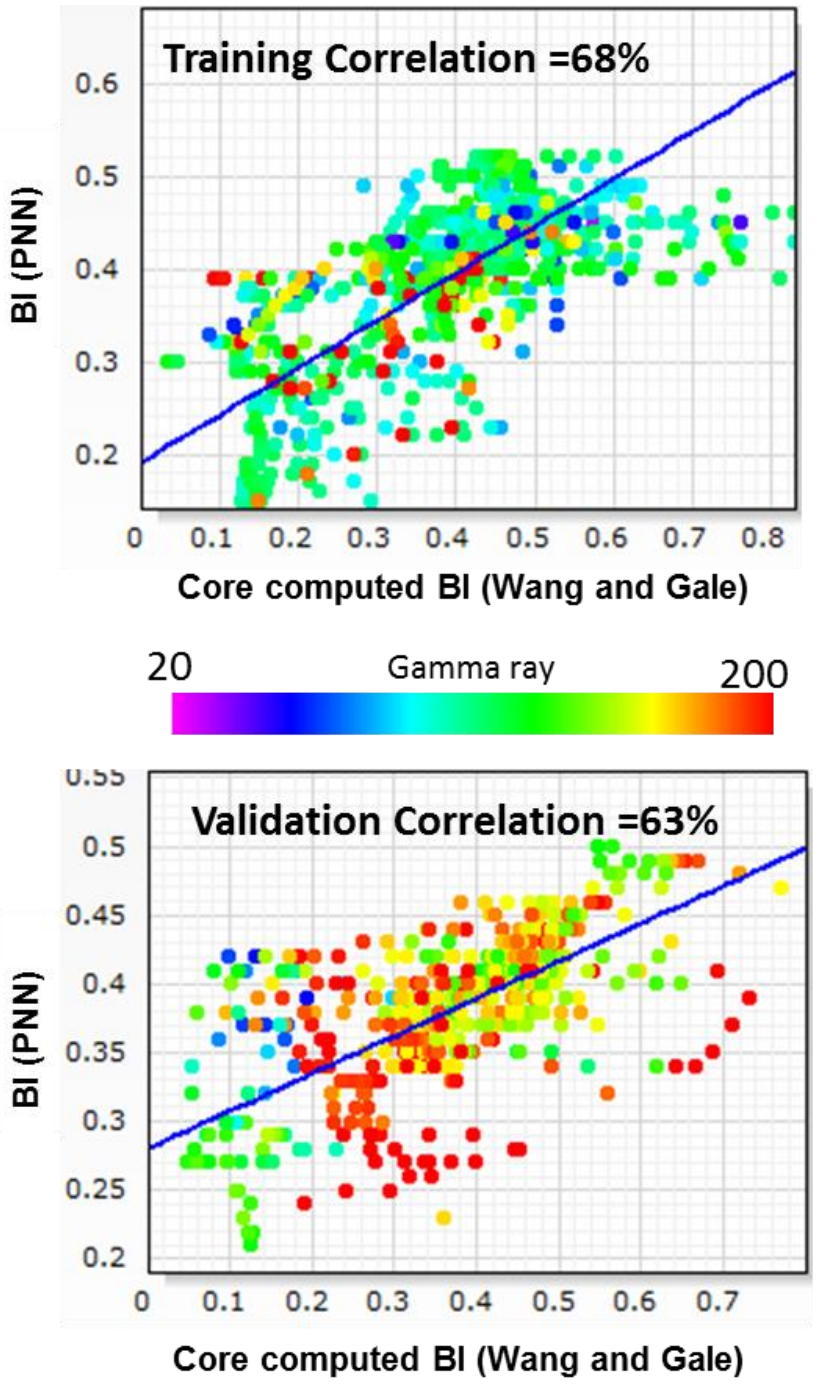

Figure 6.15 Cross plot between core computed BI and neural network estimated BI, (a) well A which was used to train the neural network, and (b) other cored well B.

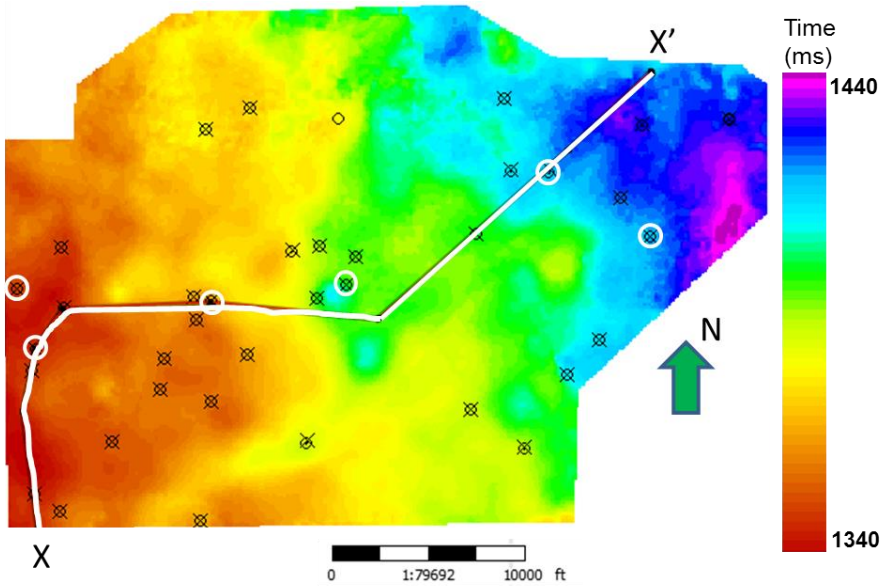

Figure 6.16. Map of top of Lower Barnett Shale surface. For neural network analysis, the circled wells were kept as blind wells and non-circled wells were used as the training wells.

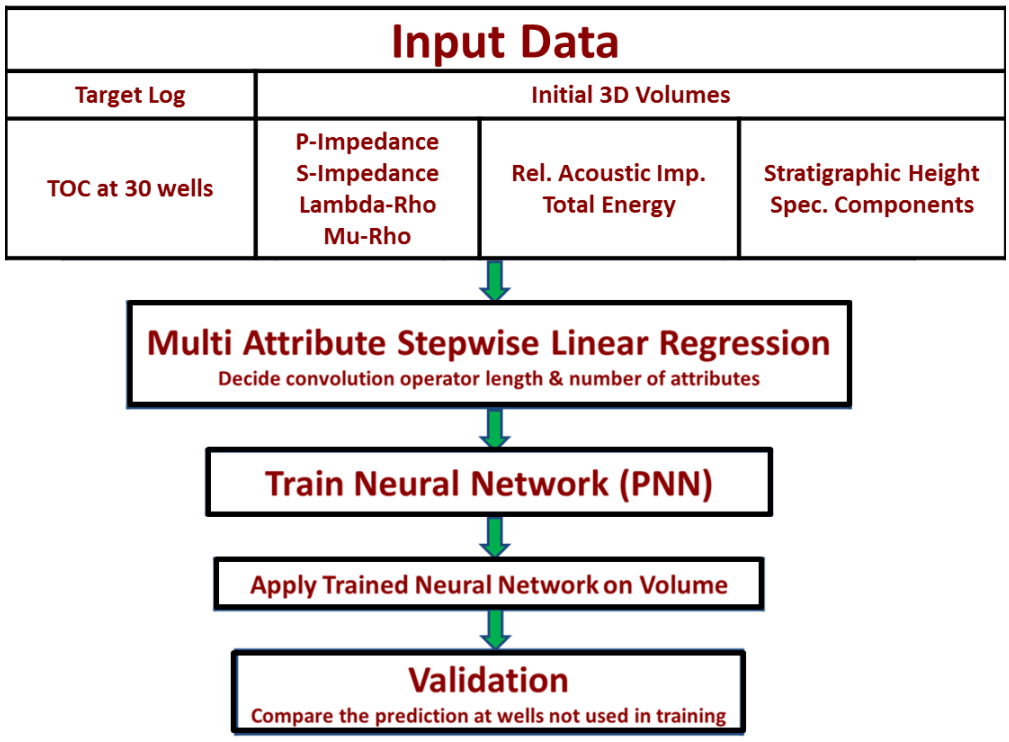

Figure 6.17. Probabalistic Neural Network work flow used to predict the TOC volume from seismic attributes.

Attribute	Training Error	Validation Error	Correlation
LambdaRho	0.89	0.91	50
Stratigraphic Height	0.64	0.66	77
Relative Acoustic Imp.	0.60	0.62	80
S-Impedance	0.58	0.61	84
P-Impedance	0.58	0.61	84
MuRho	0.62	0.61	85
Spectral_Mag_50Hz	0.62	0.61	84

Table 6.3. Validation and Training error using a window of ±8ms for volumetric TOC estimation.

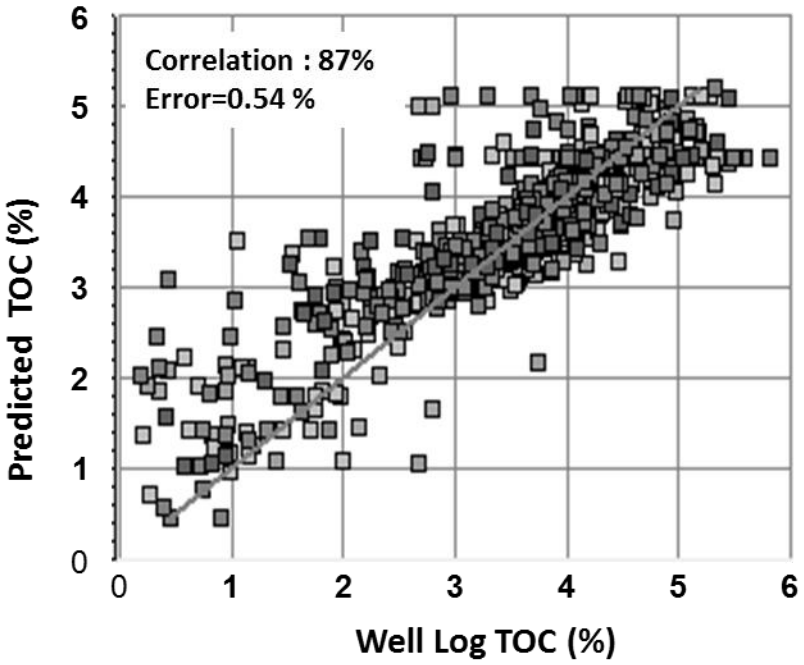

Figure 6.18. Cross-plot between predicted TOC using a neural network and TOC well log with 30 wells used in neural network training.

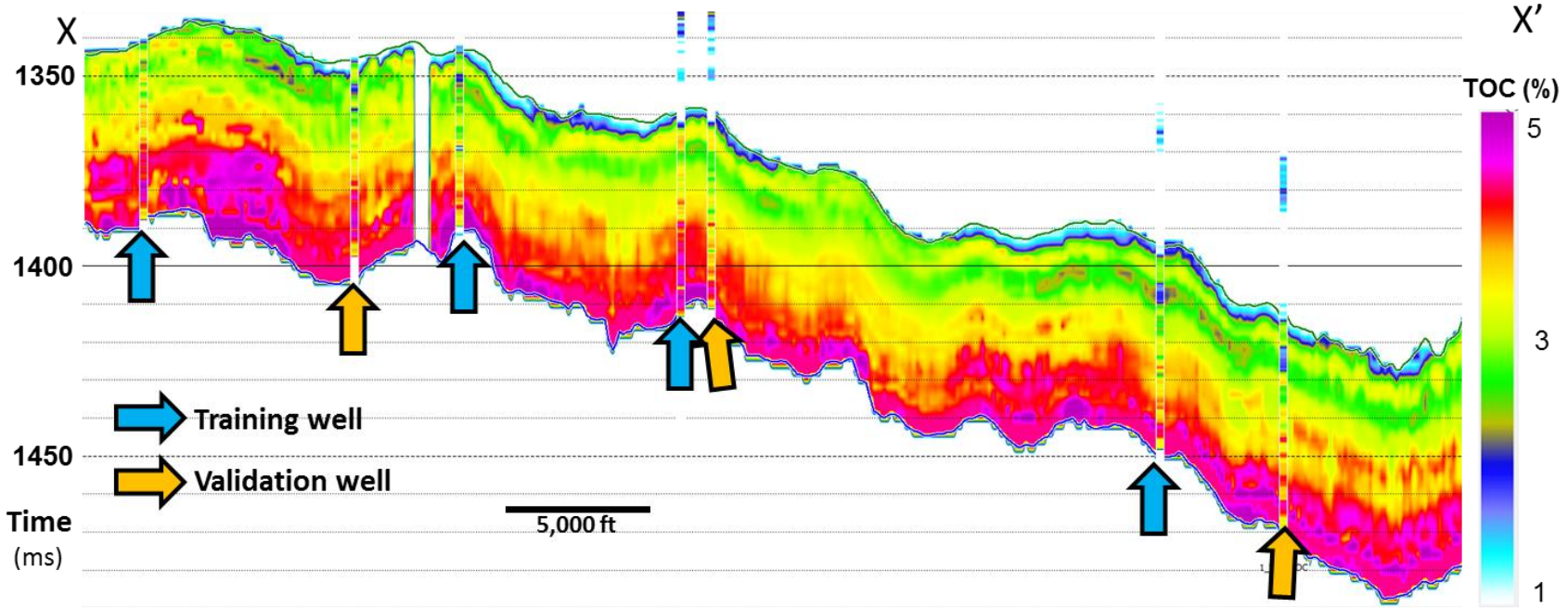

Figure 6.19. Vertical slice along the line XX' through estimated TOC volume (location shown in Figure 6.16). Notice the estimated TOC volume shows a good match at the blind wells (70 % correlation).

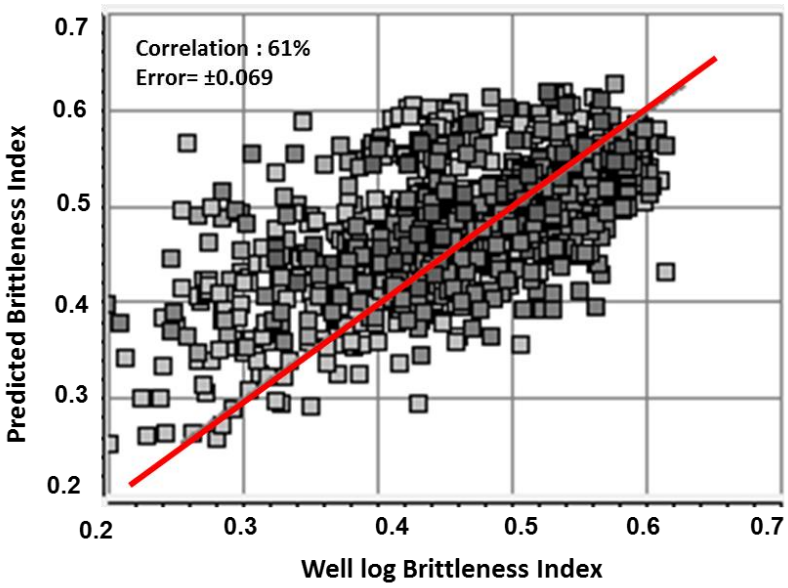

Figure 6.20. Cross-plot between predicted BI using a neural network and BI well log with 30 wells used in neural network training.

Attribute	Training Error	Validation Error	Correlation
LambdaRho	0.064	0.066	44
Stratigraphic Height	0.062	0.065	49
MuRho	0.061	0.065	51
Relative Acoustic Imp.	0.060	0.064	55
Young's Modulus	0.059	0.065	56
SMF_20	0.059	0.066	57

Table 6.4 Validation and Training error using a window of ±12 ms for volumetric BI estimation.

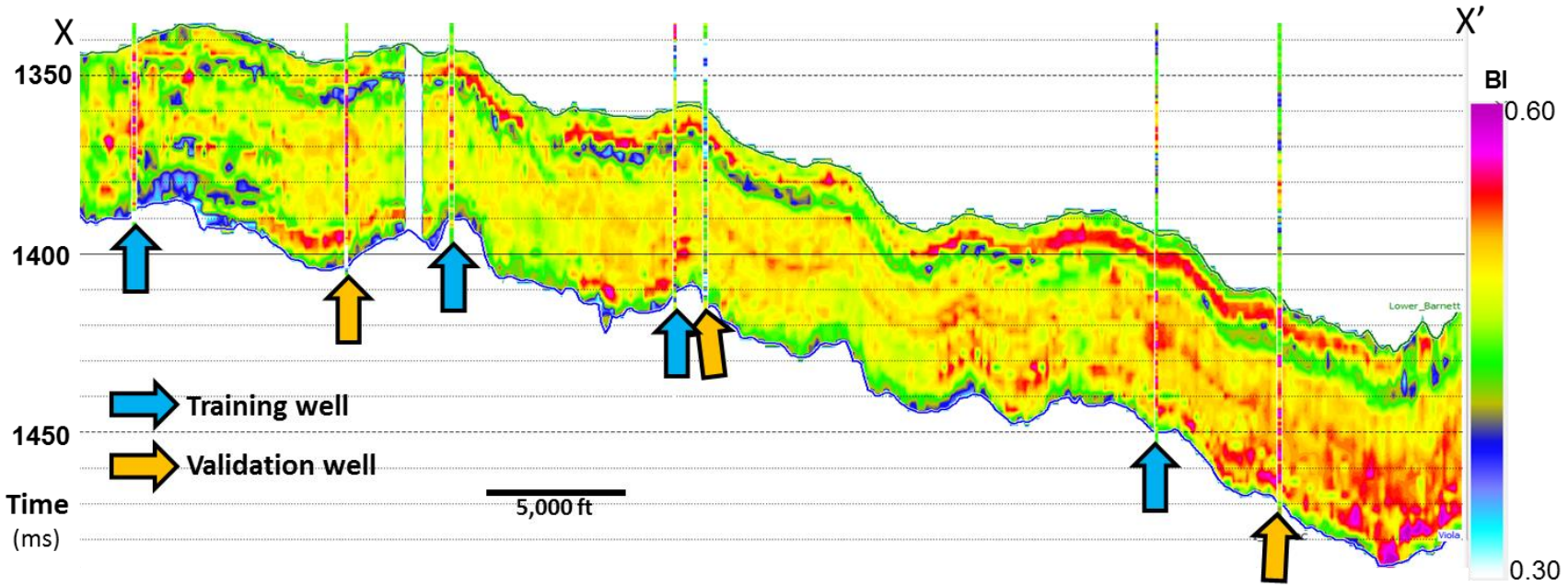

Figure 6.21 Vertical slice along line XX' through estimated BI volume (location shown in Figure 6.16. Notice the estimated BI volume shows a fair match at the blind wells (50% correlation).

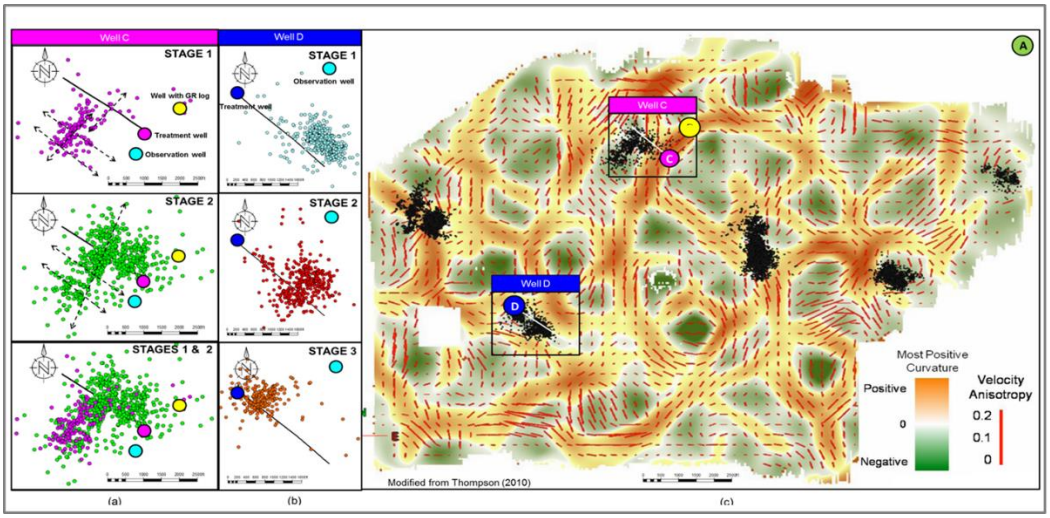

Figure 6.22. Map view of microseismic event locations corresponding to (a) Well C and (b) Well D the orientation of the fracture lineaments formed by the microseismic events align with the current maximum horizontal stress direction in the Fort Worth Basin (NE-SW). (c) Horizon slice along the top Viola Limestone through the most positive curvature seismic attribute volume. The majority of the microseismic event locations fall into the areas with negative curvature values (bowl shapes). Red vectors indicate velocity anisotropy where the length of the vector is proportional of the degree of anisotropy while the direction indicates the azimuth of maximum anisotropy.The seismic data were acquired after 400 wells stimulated, such that the velocity anisotropy represents the post-frack stress regime. (Modified from Perez, 2013 and Thompson, 2010). The maximum distance of a posted event from a well is 1000 ft, which will be used for as R_{max} in Figure 6.23.

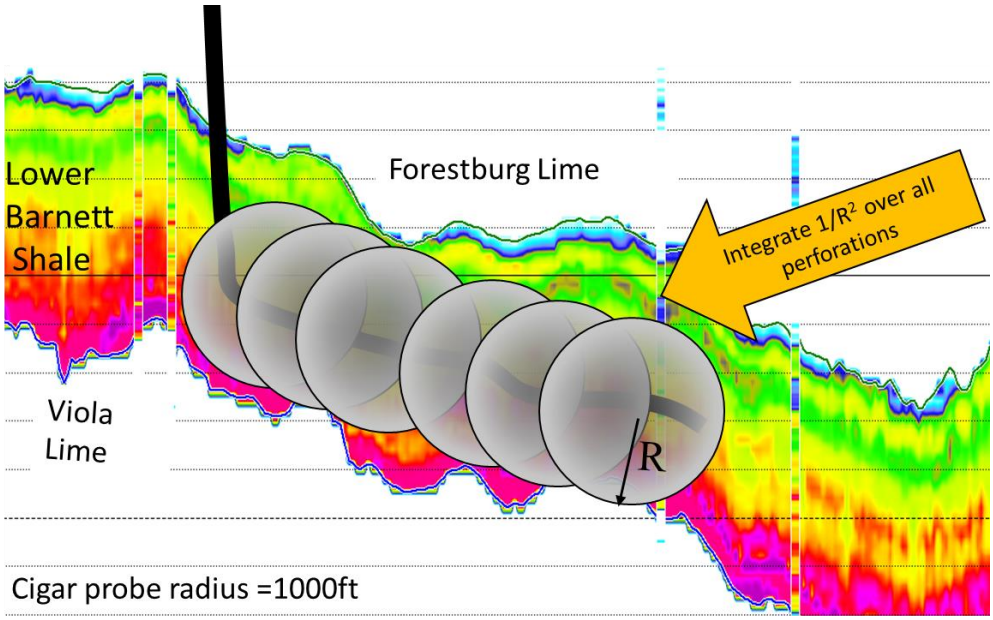

Figure 6.23. Illustration of the cigar probe workflow, horizontal well is drilled in the Lower Barnett Shale. The flow (production) to each perforation can be approximated by the impulse response of Green's function $1/R^2$. I assume all the sections are perforated and each point on the well is producing equally. Integration of all the points to along the well bore path to get the weighted average property can be correlated to the production.

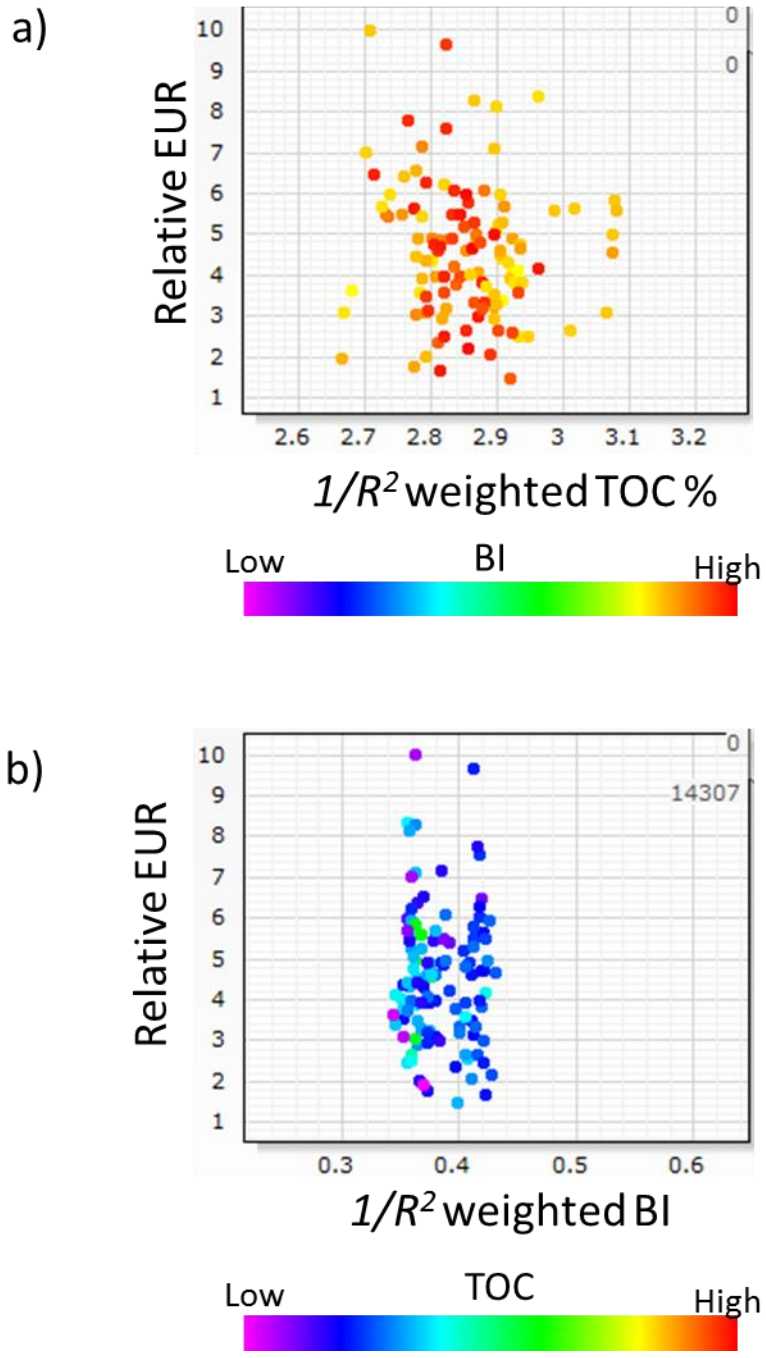

Figure 6.24 Crossplot between, relative EUR, and (a) TOC, and (b) BI. There is almost no-correlation between production and TOC or BI.

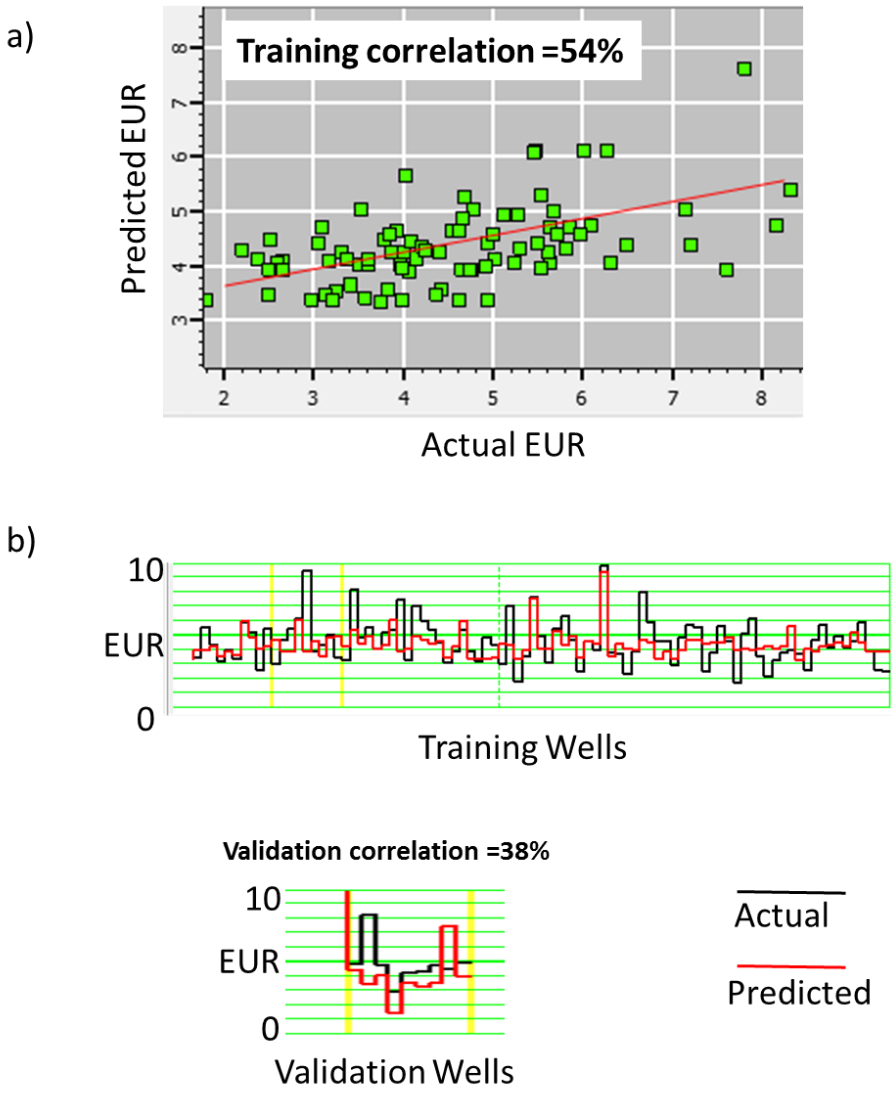

Figure 6.25. Neural network training with relative EUR as target property and TOC and BI as input. Training was done on 100 wells. (a) Cross plot between actual relative EUR and predicted EUR on training wells. (b) Plot of actual vs predicted for training wells and validations wells. Notice the training correlation is 54% and validation correlation is 38%.

REFERENCES

Aguilar M., S. Verma, 2014, TOC and fracture characterization of the Barnett Shale with predicted gamma ray and density porosity volumes: 82nd Annual International Meeting, SEG Expanded Abstracts. , 2662-2666.

Aktepe, S., K. J. Marfurt, and R. Perez, 2008, Attribute expression of basement faulting—Time versus depth migration: The Leading Edge, **27**, 360-367.

Aydemir, A., 2011, Comparison of Mississippian Barnett Shale, Northern-Central Texas, USA and Silurian Dadas Formation in Southeast Turkey: Journal of Petroleum Science and Engineering, **80**, 81 - 93.

Crain's Petro-physical Handbook, 2015, https://spec2000.net/11-vshtoc.htm, accessed on 3 July 2015.

Fernandez, A., 2013, 3D Seismic Attribute expression of the Ellenburger group Karst-Collapse features and their effects on the production of the Barnett Shale, Fort Worth Basin, Texas :MS Thesis, The University of Oklahoma.

Gupta, N., 2012, Integrated characterization of the Woodford Shale in West-Central Oklahoma: Ph.D. Dissertation, University of Oklahoma.

Hampson, D. P., J. S. Schuelke, and J. A. Quirein, 2001, Use of multi-attribute transforms to predict log properties from seismic data: Geophysics, **66**, no. 1, 220-236.

Holmes, M., D. Holmes, and A. Holmes, 2003, Generating missing logs -techniques and pitfalls extended abstract): AAPG Annual Meeting, Salt Lake City, Utah Search and Discovery Article #40107 (2003), Web accessed 15 October 2012. http://www.searchanddiscovery.com/documents/2003/holmes/images/holmes.pdf

Johnson, G., Miller, P., Advanced imaging and inversion for unconventional resource plays, First Break, 31 No.7, 41-50

Kale, S., 2009, Petro-physical characterization of Barnett Shale play: M.S. Thesis, the University of Oklahoma.

Kalkomey, C. T., 1999, Potential risks when using seismic attributes as predictors of reservoir properties: The leading Edge, **16**, 247-251.

Montgomery, S. L., D. M. Jarvie, K. A. Bowker, and R. M. Pollastro, 2005, Mississippian Barnett Shale, Fort Worth basin, north-central Texas: Gas-shale play with multi–trillion cubic foot potential: AAPG Bulletin, **89**, no. 2, 155–175.

Passey, Q.R., S. Creaney, J.B. Kulla, F.J. Moretti, and J.D. Stroud, 1990, A practical model for organic richness from porosity and resistivity logs: AAPG Bulletin, **74**, p. 1777-1794.

Paxton, S. T., A. M. Cruse, and A. M. Krystynaik, 2006, Detailed Fingerprints of Global Sea-level Change Revealed in Upper Devonian /Mississippian Woodford Shale of South-Central Oklahoma: AAPG Annual Convention.

Perez, R., 2013, Brittleness estimation from seismic measurements in unconventional reservoirs: Application to the Barnett Shale: Ph.D. Dissertation, University of Oklahoma.

Perez, R., K. J. Marfurt, 2014, Mineralogy-based brittleness prediction from surface seismic data: Application to the Barnett Shale: Interpretation, **2**, T255-T271.

Pollastro, R. M., 2007, Geologic framework of the Mississippian Barnett Shale, Barnett – Paleozoic total petroleum system, Bend arch-Fort Worth Basin, Texas: AAPG Bulletin, **91**, 405–436.

Singh, P., 2008, Lithofacies and Sequence Stratigraphic Framework of the Barnett Shale, Ph.D. Dissertation, University of Oklahoma.

Slatt, R. M. and Y. Abousleiman, 2011, Multi-scale, brittle-ductile couplets in unconventional gas shales: Merging sequence stratigraphy and geomechanics: AAPG Search and Discovery Article #90124.

Sondergeld, C. H., K. E. Newsham, T. E. Comisky, M. C. Rice and C. S. Rai, 2010, Petrophysical Considerations in Evaluating and Producing Shale Gas Resources : Expanded Abstract SPE-131768-MS.

Verma, S. , A. Roy, R. Perez, K. J. Marfurt, 2012, Mapping high frackability and high TOC zones in the Barnett Shale: Supervised Probabilistic Neural Network vs. unsupervised multi-attribute Kohonen SOM: 82nd Annual International Meeting, SEG Expanded Abstracts, 1-5.

Verma, S., K. J. Marfurt, A Way of TOC Characterization on Barnett and Woodford Shale: AAPG Annual convention, Search and Discovery Article: 80429.

Walper, J. L., 1982, Plate tectonic evolution of the Fort Worth Basin, in C. A. Martin, ed., Petroleum geology of the Fort Worth Basin and Bend arch area: Dallas Geological Society, 237–251.

Walter H. Fertl and George V. Chlllngar, 1988, Total Organic Carbon Content Determined From Well Logs: SPE Formation Evaluation, **3**, no. 02, 407-419.

Wang, F. P., and J. F. W. Gale, 2009, Screening criteria for shale-gas systems: GCAGS Transactions, v. 59, 779-793.

Zhang, B., T. Zhao, X. Jin, and K. J. Marfurt, 2015, Brittleness evaluation of resource plays by integrating petrophysical and seismic data analysis, Interpretation, **3**, T81-T92.

Zhao, T., S. Verma, and D. Devegowda, 2015, TOC estimation in the Barnett Shale from triple combo logs using support vector machine: 85th Annual International Meeting, SEG Expanded Abstracts.

Zhao, T., S. Verma, J. Qi, and K. J. Marfurt, 2015, Supervised and unsupervised learning: how machines can assist quantitative seismic interpretation: 85th Annual International Meeting, SEG Expanded Abstracts.

CHAPTER 7 **: CONCLUSIONS**

In this dissertation I examine the need and developed workflow for seismic data reprocessing and conditioning for quantitative interpretation of unconventional reservoirs.

In chapter 2, I demonstrated that seismic data conditioning and careful data QC are keys to avoiding pitfalls that hinder accurate results of quantitative interpretation. Detailed gather by gather seismic data QC is impractical for large mega merge surveys on the order of 50 GB. I developed a workflow based on angle-limited stacks that allows an interpreter to determine the usable limits of the data. Subsequent inversions should be offset- (and implicitly, angle-) limited to include only those offsets with physically reasonable amplitudes. RMS error maps of the modeled-to-measured data misfit should be used to validate the result and in subsequent risk analysis.

In Chapter 3, I present the use of seismic modeling to determine common pitfalls in seismic analysis. The attribute expression of the subsurface depends not only on the impedances and geometric configuration of the various facies, but also on the acquisition and subsequent processing and imaging of the seismic data.

In Chapter 4, and Chapter 5 I show the effect of highly aliased ground roll and presented a method to suppress such ground roll. Reprocessing can significantly enhance the data quality on legacy seismic data of North-central Texas. My proposed workflow of coherence based ground roll suppression helped to remove the highly aliased broad band ground roll. The explicit search for sample-by-sample phase velocities allows the filter to adapt to dispersive groundroll wave trains. The short, overlapping 3D window

implementation allows the filter to model piecewise continuous groundroll events that are broken by irregular topography and discontinuities in the weathering zone. Edge preserving structure oriented filter and 5D interpolation improved significantly the data quality.

In chapter 6, I investigate the value of integration of core, well and seismic data for estimating TOC and brittleness volumes, through quantitative interpretation on the Barnett Shale of the Fort Worth Basin. My analysis shows that TOC estimated on the well logs (on the cored well) with non-linear regression (using Passey's TOC, normalized stratigraphic height and other well logs) provides higher correlation on a blind well compared to Passey's method derived TOC. BI (computed by Wang and Gale's formula) on the cored well was correlated to the well logs and the established non-linear regression relationship showed a good correlation on the blind well test. Neural network volumetric prediction of TOC and BI, utilizing seismic attributes, seismic inversion products, TOC and BI well logs, showed a decent match on the blind wells.